Microfabricated Tools and Engineering Methods for Sensing Bioanalytes

Thesis by
Aditya Rajagopal

In Partial Fulfillment of the Requirements for the Degree
of
Doctor of Philosophy

CALIFORNIA INSTITUTE OF TECHNOLOGY
Pasadena, California
2014
(Defended July 22nd, 2013)

ACKNOWLEDGEMENTS

First, I would like to thank my advisor, Axel Scherer. You have patiently mentored me all my adult life, and you have given me the freedom and the resources to explore my interests. You have tolerated many of my zanier ideas, and you have allowed me to learn despite my mistakes. I will not forget that you used to give me rides to parents house many times as an undergraduate, so that I could see my folks. Thank you for everything!

I would also like to thank my co-advisor Professor Tom Tombrello for guiding me for several years from my days as an undergraduate in the Scherer group. You have been an excellent sounding board, and you have encouraged me through the hard times. You have been my mentor, and I would not be here without your help.

I would like to thank the wonderful Caltech faculty members for excellent interactions, conversations, and advice. My interactions with PPV have been very beneficial and I am grateful to have learned a great deal about DSP from him. I would like to thank professors Yu-Chong Tai, Azita Emami, Scott Fraser, David Rutledge, Greg Tsongalis and David Baltimore for their advice and help in finishing my work. I also want to thank Emil Kartalov for much encouragement, mentoring, and support over the years.

My close friends from home have always believed in me. Shivaram, Arjun, Si-Hyun, Mr. Kessler, Mr. Davis, Mrs. TV, I love you guys. Thank you for everything. Kim, you have been my best friend from high school and you have always seen me through difficulties. Steve, thank you for putting me on the path that got me here. Rest in peace, my friend.

I also thank my friends at Caltech, who have shepherded me through this journey. Vi Tran, Ryan Witt, Jesse and Jessica Escobedo, Michael Priolo, Timothy Kwa (BFF), Rahul Deb (Amigo 1), Carlos Saldana (Amigo 2), Craig Montouri, Carl Allendorph, Jennifer Yim, Manuel Monge, Eyal En Gad, John Statman, and Michael Woods (TTIS). You have always been there for me and I made it because of you.

Of course, none of this would have been possible without the awesome Scherer Group. Andrew Homyk, Sameer Walavalkar and Dave Henry, thank you for patiently mentoring me all these years. You got me through three degrees! My other labmates were awesome and instrumental in getting me to this point: JQ Huang, Erika Garcia, Jeff Chang, Mike Shearn, Uday Khankhoje,

Akram Sadek, Mujeeb Rahman, Imran Malik, Mark Goldberg, Kate Finigan, Dvin Adalian, Max Jones, William Fegadolli, Xiomara Madero, Saurabh Vywhare, Emil Kartalov, George Maltezos, Samson Chen, Teresa Emery, Joyce Wong, Chris Walker, and Mladen Barbic. Thank you guys!

Finally, I would like to thank the members of my wonderful, large, and often-times crazy family. We finally made it through Caltech! Prabha Aunty, Deepu, Veena, Neetu, Arvindh, Ishani, and Bharath, thank you for always being there for me, through thick and thin. Thebes, Raj Uncle, Disha, Goondo, thank you for being my second family and supporting me through all my significant milestones.

Erika and Karina, I am so glad to have had you guys in my life. Erika, the love and support from you has made Caltech worthwhile. Who else would patiently support, encourage, and prod me through the misery that is the thesis writing process? You persisted despite my every inclination to procrastinate. Who else would willingly to stay past midnight in lab looking at results on Fridays and Saturdays? You are my e^-: you complete my valence shell! Thank you for everything.

Amma, Dad, Abhe, I love you to death and you have been the foundation for my success. Abhe, you are the most important person in the world for me, and I love you to death. Thank you for supporting me on this journey. Amma, you have always held me through hard times, and you have never given up on me. Dad, you are my hero, and you are the person I want to be when I grow up. You have been my inspiration for all my life, and I would not be here without you. Pati and Akka, my thesis is dedicated to you both.

ABSTRACT

There is a convergence between the needs of the medical community and the capabilities of the engineering community. For example, the scale of biomedical devices and sensors allow for finer, more cost-effective quantification of biological and chemical targets. By using micro-fabrication techniques, we design and demonstrate a variety of microfluidic sensors and actuators that allow us to interact with a biochemical environment. We demonstrate the performance of microfluidic blood-filtrations chips, immune-diagnostic assays, and evaporative coolers. Furthermore, we show how micro-fabricated platinum filaments can be used for highly localized heating and temperature measurement. We demonstrate that these filaments can be used as miniature IR spectroscopic sources. Finally, we describe and demonstrate novel combinatorial coding methods for increasing the information extracted from biochemical reactions. We show proof-principle of these techniques in the context of Taqman PCR as well as persistence length PCR.

TABLE OF CONTENTS

LIST OF ILLUSTRATIONS

LIST OF TABLES

NOMENCLATURE

ASIC. Application-specific integrated circuit

B2M. Beta-2-microglobulin

CCD. Charge-coupled device

cDNA. Complementary deoxyribonucleic acid

CLIA. Clinical Laboratory Improvement Amendments

CNS. Central nervous system

Ct. Cycle threshold

Cy3. Cyanine 3 dye

Cy5. Cyanine 5 dye

dc. Direct current

DNA. Deoxyribonucleic acid

EDTA. Ethylenediaminetetraacetic acid

ELISA. Enzyme-linked immunosorbent assay

FAM. 6-carboxyfluorescein derivative of fluorescein

FIB. Focused ion beam

FWD. Forward primer

FRET. Fluorescence resonance energy transfer

GalC. Galactocerebroside

GapDh. Glyceraldehyde 3-phosphate dehydrogenase

GusB. Beta-glucuronidase

HIV. Human immunodeficiency virus

Hmpv. Human metapneumovirus

Hrv. Human rhinovirus

HSV. Herpes simplex virus

IAC. Immunoaffinity chromatography

Inf. Influenza

IR. Infrared

LED. Light emitting diode

MEMS. Microelectromechanical systems

MMP-9. Matrix metallo-proteinase-9

MOG. Myelin oligodendrocyte glycoprotein

M13. Filamentous bacteriophage composed of circular single stranded DNA

N2. Nitrogen gas

Pa. Pascal

PCB. Printed circuit board

PCR. Polymerase chain reaction

PDMS. Polydimethylsiloxane

PID. Proportional-integral-derivative

PIV. Parainfluenza virus

psi. Pound-force per square inch

Pt. Platinum

rf. Radio frequency

RNA. Ribonucleic acid

ROX. Reference dye designed to normalize the fluorescent reporter signal in real-time quantitative polymerase chain reaction

RR. Relapsing-remitting

Rsv. Respiratory Syncytial Virus

RTD. Resistance thermometer device

RT-PCR. Real-time polymerase chain reaction

RWD. Rewind primer

qPCR. Quantitative polymerase chain reaction

SARS. Severe acute respiratory syndrome

SEM. Scanning electron microscope

SNP. Single-nucleotide polymorphism

SNR. Signal to noise ratio

TCR. Temperature coefficient of resistance

C h a p t e r 1

INTRODUCTION

The quantification and characterization of bioanalytes in various serums can provide insight into the identification and quantification of pathogens. The capture and recognition of proteins, nucleic acids, and other biochemicals that are specific to certain illnesses, can be used to track the progression of these diseases. For example, measurements on protein markers for disease are routinely performed at medical facilities on a variety of patient samples such as blood serum, cerebro-spinal fluid, and urine. Protein markers are captured in vitro by utilizing the highly specific interactions between antibodies and their antigens; once captured, the presence of a particular antigen is determined by observing a reporting tag. In the case of antibody tests, these are usually fluorescent labels; one then correlates the intensity of the fluorescent signal with the quantity of antigen (e.g. protein) present.

However, for a bioanalyte assay to reliably track fluctuations in pathogen concentrations, it must be sufficiently specific (to minimize false positives) and sufficiently sensitive (to minimize false negatives). By shrinking chemical chambers from the millimeter size-scale, as used currently in laboratories, to the micrometer size-scale, more sensitive measurements of bioanalytes can be made in extremely small sample volumes, in a highly parallelized fashion [1-4]. Using microfabrication techniques, borrowed from the semiconductor industry, we have made microfluidic valves, gates and mixers in elastomers such as polydimethylsiloxane (PDMS). This fabrication strategy has been investigated in detail by many others, and has resulted in a codified, repeatable method of manufacturing microfluidic devices [5-6].

These devices have been used to create automated chemical laboratories [7-9]. At the micro-liter and nano-liter size scale, low Reynolds number flows allow for interesting fluidics. For example, viscous forces are much greater than inertial forces in microfluidic geometries; this allows for laminar, rather than turbulent flows [10]. Laminar flows are conducive to diffusion-limited mixing, which is a feature that is readily exploited in many microfluidic devices [11].

In this thesis, we exploit diffusion-limited mixing by designing microfluidic reaction chambers that maximize surface-area-to-volume ratios, and in turn, allow for more efficient interactivity

with a chemical environment. We demonstrate that such interaction facilitates immuno-capture of antigens with high sensitivity. We show the efficacy of a microfluidic chip that performs an enzyme-linked immunosorbent assay (ELISA) to capture protein targets specific to multiple-sclerosis symptom activity. As proof-of-principle that our portable, microfluidic platform is suited for qualitative protein detection, we capture and detected matrix metalloproteinase-9 (MMP-9) and galactocerebroside (GalC) in concentrations down to 65 nM. In addition, we demonstrate how similar passive elastomeric structures can be used for preparing a sample serum for bioanalyte detection. The feasibility of a microfluidic blood filtration device, as well as an immunoaffinity-based pathogen capture device, are also investigated. We show that these structures outperform their macroscopic laboratory counterparts.

We also show how active fluidic structures can be used to regulate the activity of enzymatic reactions. For instance, we fabricated microfluidic, evaporative coolers in PDMS for temperature regulation, and we show that rapid, highly localized thermal cooling rates (in excess of 40 Centigrade/second) can be achieved by endothermically mixing refrigerant and gas. We also demonstrate that highly localized heating can be achieved by fabricating micron-scaled and nano-scaled platinum heaters. We demonstrate that these platinum thin-film filaments can be used as heaters, temperature sensors, and IR spectroscopic sources. Furthermore, we briefly describe how these structures can be used for locally regulating enzymatic reactions such as the polymerase chain reaction (PCR)--a method for copying DNA [12].

PCR

PCR is a gold-standard biological technique for copying a specific nucleic acid target. In this technique, a chemical cocktail consisting of the nucleic acid target of interest, free base pairs (adenine, guanine, cytosine, thymine), short-strand complementary (to the intended target) DNA known as primers and DNA polymerase (an enzyme which synthesizes DNA), is rapidly heated and cooled between various temperature set points. If this cocktail is heated to a sufficiently high temperature, all the double stranded DNA polymers will unwind (as they will have sufficient thermal energy to break the hydrogen bonds with their complementary sequences. When this cocktail is cooled to a sufficiently low temperature the specific, low molecular weight primer sequences competitively bind to the DNA target of interest. In the presence of free nucleotides and DNA polymerase, the primer strands will be extended--effectively making a copy of the

DNA target of interest. As this procedure is repeated over successive cycles, the quantity of DNA is exponential increased (ideally, by a factor of 2 each cycle; though the actual factor is less due to concentration-based reaction-rate effects).

By choosing primers with sufficient specificity, both RNA and DNA targets can be copied, though a cDNA conversion step is required for an RNA target. This technique can be used to selectively amplify and then detect pathogenic or diagnostic nucleic acid targets in a serum. In fact, with a limit of detection as low as 6 copies/mL, quantitative PCR (qPCR) has been adopted as the most-sensitive, most-specific molecular diagnostic test for residual infectious disease measurements. In this thesis, we briefly mention how efficient thermal design on the microfluidic scale can be used to create low cost PCR instruments.

PCR Instruments

Current commercial systems for performing thermal cycling are typically large, bulky bench-top devices. Due to legacy geometries, these devices are designed to batch process samples in molded plastics (Figure 1.1) that contain a large number of individual reaction chambers (e.g. 48, 96, 384).

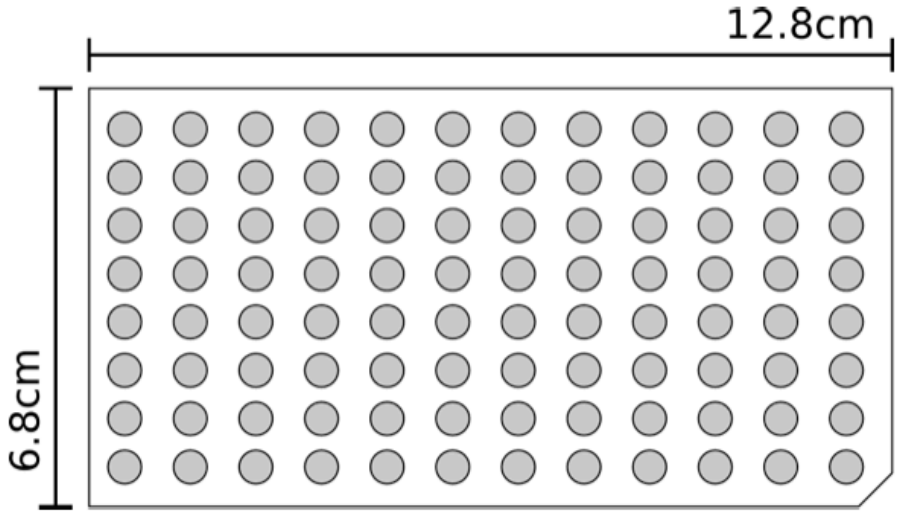

Figure 1.1 Typical dimension of a 96-well PCR plate.

These reaction vessels are heated and cooled using either forced air or Peltier junctions methods. While the former is cheaper, it is less effective at maintaining stable temperature profiles (temperature ramp rates are dependent on ambient temperature); the latter allows for quicker

temperature ramping, at the expense of significantly larger power requirements. Expensive electronics and bulky detection optics have precluded these devices from being used as platforms for low-cost, portable diagnostics. A portable PCR instrument, for example, would be particularly applicable to point-of-care diagnostics and developing world environments [13-15], as laboratory-grade instruments are not a financial or logistic possibility.

One approach to making a low cost instrument is to lower the complexity of the instrument by eliminating optics. This strategy does decrease the profile and cost of a PCR instrument, at the expense of requiring external detection methods to report on the result of the reaction. In these types of instruments, the identification of the DNA product is done through DNA hybridization [16], gel electrophoresis [17], or light absorption/fluorescence measurements. Amplification-only PCR instruments are appropriate when PCR is required only to increase the quantity of DNA (e.g. PCR preparation before sequencing), rather than to detect the presence or initial concentration of specific sequence. However, decoupling detection with amplification is not a suitable solution for PCR in point-of-care medical diagnostics or portable molecular diagnostics instruments.

Another strategy for increasing portability is to design an instrument that works on substantially smaller sample volumes. Others have tried to reduce the spatial complexity of the PCR instrument, by switching to novel geometry reactors built in a variety of materials such as silicon, silicon oxide, silicon nitride, and PDMS [18]. The limitations of these systems are that they require sophisticated assembly procedures to manufacture reaction chambers, resulting in systems that, while portable, are impractical to manufacture. For example, one device combines microfluidic reactions chambers defined in silicon dioxide with PDMS valves to create a single substrate qPCR reactor (Figures 1.2 and 1.3) [19]. The complicated microfabrication procedure and complex valving for this device preclude its adoption for low-cost, rapid PCR diagnostics.

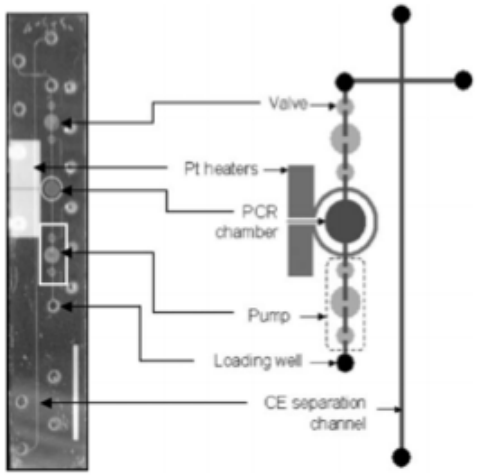

Figure 1.2 PDMS/glass hybrid reactor [19].

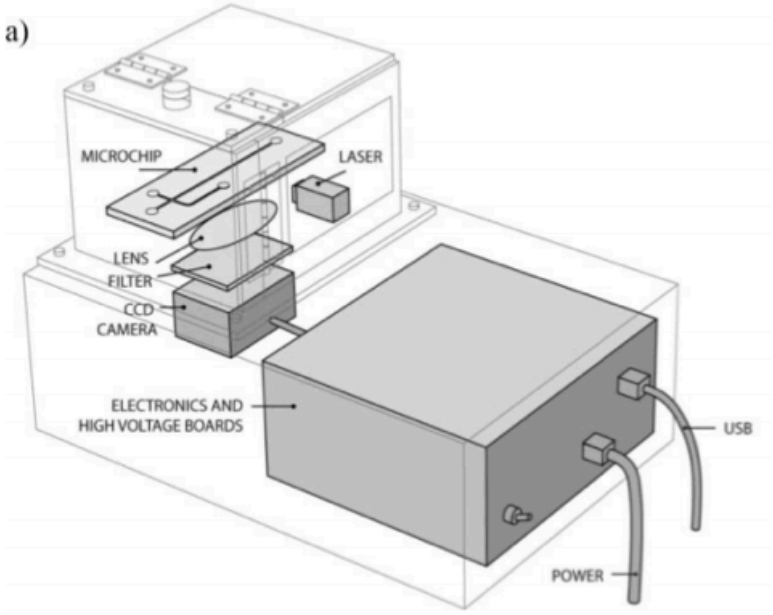

Figure 1.3 qPCR system with disposable microfluidic reactors [19].

In addition to reducing the cost of materials and supplies required to run a PCR reaction, small volume chambers allow for smaller thermal masses, and hence more rapid thermal cycling. For instance, Zou notes that thermal delays while moving between temperature set-points in microchip reactors can be significantly less than the thermal delays in macro-tube reactors (Table 1.1) [20]. While this is true, the dominant delay in most modern PCR reactors is not the latency in heating and cooling, but the time-scales required for the reaction itself.

Table 1.1 Thermal delays in macro-tube (30° cone tip) and in micro-chip.

	Volume (µl)						
	1	10	25	65	100	123	200
t_d in macro-tube (s)	2.5	11.5	21.2	39	39	39	39
t_d in micro-chip (s)	0.003	0.26	1.6	11	25	39	104

However, the cost of polymerase chain reactors can be reduced by simplifying and optimizing thermal control. For example, others have built PCR chambers wherein the reaction cocktail is pumped past isothermal zones [14] corresponding to the temperature required for the denature, anneal, and extend steps of thermal cycle, the PCR reaction. In this design, the PCR reaction is no longer delayed by heating and cooling of the sample mixture [20]. In one such device, the PCR cocktail is sequestered in a triangular-shaped, closed-circuit fluoropolymer tube (Figure 1.4).

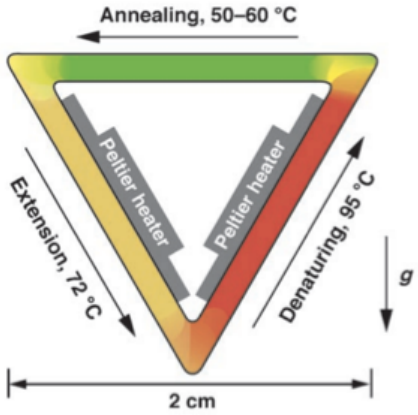

Figure 1.4 Geometry of an isothermal PCR device.

The temperature on the two sides of the tube are regulated 95°C and 72°C by Peltier junctions, while the third side is passively cooled to 58°C [14]. Convection motivates the fluid to travel between the temperature zones, resulting in a single PCR cycle every revolution. The pitfall of this particular system is that the chamber geometry determines both the temperature profile and the cycling time. In order to change PCR conditions, a new reactor must be designed. While this is acceptable as a demonstration of PCR, it is not a feasible solution for a general purpose PCR reactor. While not lowering the cost of a PCR instrument or the PCR reactor itself, the true benefit of isothermal PCR is that it allows for significantly lower power consumption due to passive heating.

System-level efforts to miniaturize the PCR reactor have resulted in practical machines that are as small as laptops [21]. For example, Belgrader describes a 4-color quantitative PCR device that uses commodity LEDs, photodiodes, thin-film heaters, and injection molded plastics (Figure 1.5) [21]. By using existing mass-market components mated with a custom-designed plastic chamber, the authors were able to realize a low-cost, portable PCR reactor. While the advantage of this system is that is portable and low-cost (~$1500), it is only capable of measuring one reaction at a time. The authors double the spatial multiplicity by combining two sets of heaters and detectors onto a single platform; however, this is not a scalable solution. Any benefit in space-saving and cost-saving is lost if a large number of samples are to be run simultaneously (e.g. 12, 24, 48).

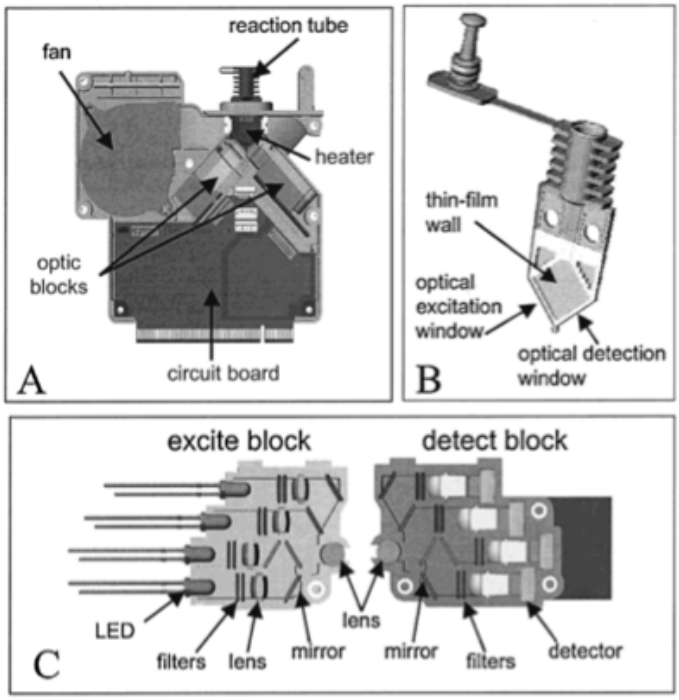

Figure 1.5 Principle components of a laptop-sized PCR reactor [21].

Others have suggested using printed circuit board (PCB) materials to make portions of chemical reactors, and specifically for PCR [22]. However, prior implementations have either involved integrating PCB electronics for temperature measuring or heating with existing PCR cartridges and instrumentation, or mating PCBs with cavities extruded in other materials [20, 23]. For example, other groups have defined 1-5μL chambers in silicon and silicon dioxide that are regulated by thin-film heaters [23]. Our strategy was to leverage the fabrication capabilities of the computer manufacturing industry to fabricate a microliter PCR chamber entirely out of printed

circuit boards. This fabrication process had the advantage of allowing us to integrate both temperature sensors and heaters onboard the cartridge, allowing for extremely accurate temperature control.

Initially, we opted to design PCB boards with embedded copper channels to define the reaction chamber. After receiving the boards, we defined the cavities by clearing the copper in these channels using either electrochemical and diffusion etches in ferric chloride and hydrogen chloride. We demonstrated that we were able to define cavities in the circuit boards without any change to their manufacturing process (Figure 1.6). However, to facilitate easy testing of the PCR reactor, we elected to transfer the fabrication procedure for these cavity devices, to a PCB manufacturing facilities (RigiFlex Inc., Anaheim, CA; Hughes Circuits Inc., San Marcos, CA) for large-scale production of a 100 cartridges.

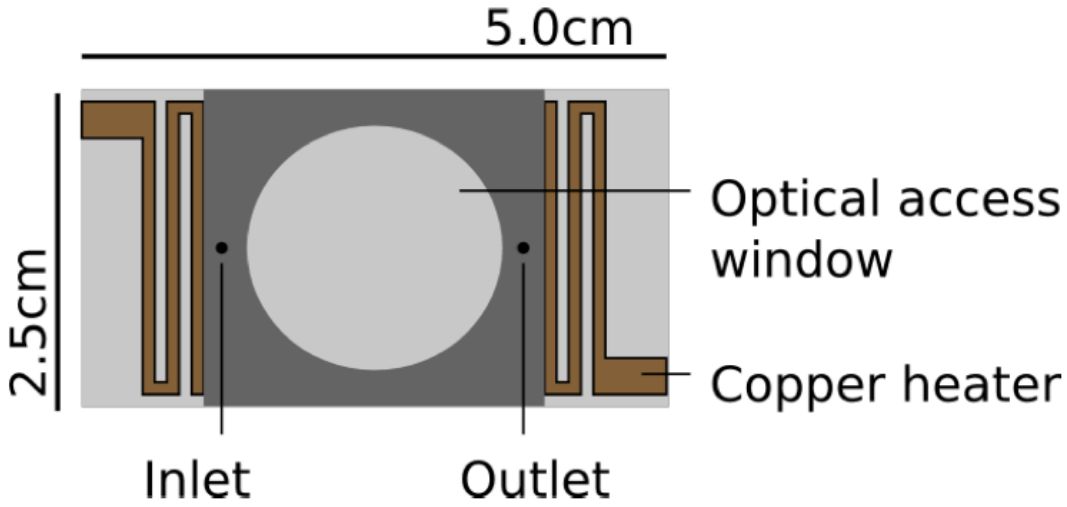

Figure 1.6 Topology of printed circuit board PCR chamber.

We demonstrated both thermal cycling and nucleic acid amplification in a hand-held, battery operated, $100 PCR instrument the size of cell phone (Figure 1.7). Temperature regulation in our reactor was achieved by varying the power delivered to either a copper resistive heater or a 25mm forced-air cooling fan (Figure 1.8). Furthermore, thermal stability was achieved by configuring both the heater, cooler, and temperature feedback thermistor in a PID control loop. We successfully amplified synthetic DNA sequences corresponding to regions of interest in HIV, HSV, malaria, and tuberculosis. The amplified product was verified using external fluorometry.

Figure 1.7 Pocket PCR system.

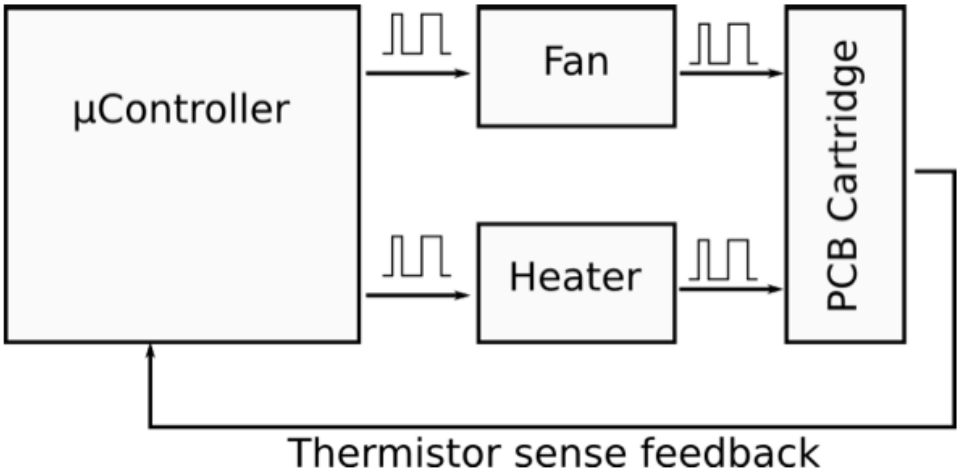

Figure 1.8 Pocket-sized polymerase chain reactor temperature control topology.

PCR Reporting

There are several strategies for reporting a PCR reaction. Currently, most PCR reactions are observed through the measurement of a fluorescent reporter specific to a particular nucleic acid sequence. For instance, fluorescence signals, from either intercalating dyes or fluorescent probes, can be used to identify and track the amplification of particular nucleic acid sequences over time. Both types of detection schemes offer their advantages and disadvantages.

Intercalating dyes are organo-metallic, aromatic complexes that are often hydrophobic and are incorporated into the naked interstices of double stranded DNA [29]. The dyes fill the interstitial binding sites in the varying ratios of one dye per 4-5 base pairs (e.g. ethidium bromide) to one dye per 2 base pairs (thiazole orange) [24]. These dyes exhibit maximal fluorescence when

stabilized in the double helix of the nucleic acid [24, 28]. For example, the thiazole orange exhibits a ~20000x increase in fluorescence when bound to double stranded DNA as opposed to being unbound [24].

Interestingly, for many intercalating dyes, the fluorescence quantum efficiency was independent of the saturation of the binding sides, meaning the fluorescence signature directly correlates with the number of fluorophores that have been incorporated into the double strands. As such, the intensity of a fluorescence signature can be linearly correlated with the total amount of double stranded nucleic acid. Though the fluorescent compounds are not discriminatory in their binding [24], it is still possible to distinguish multiple sequences so long as they are sufficiently varying in length. By carefully measuring the changes in fluorescence intensity while heating up a cocktail containing DNA strands of different lengths slowly, it is possible to associate a particular target with a particular change in fluorescence. This type of "melt-curve" analysis is routinely performed for DNA identification.

Another strategy for labeling DNA is to fix fluorescent compounds to nucleic acid sequences that are complementary to a nucleic acid target of interest. For example, one can fix two chromophores to the 5' and 3' ends of a short, single-stranded DNA sequence (Figure 1.9) in such a fashion that is complementary to itself. The chromophore at one end is designated as the fluorophore, while the chromophore at the other end is designated as the quencher. Even when excited, the fluorescence emission from the fluorophore will be damped when if it is in close proximity to the quencher. This interaction is governed by fluorescence energy transfer [25].

At lower temperatures, the probe forms a hairpin structure with itself that brings the fluorophore into close proximity with a matched quencher. In this configuration, the excited fluorescence emission is minimal, as the two chromophores are within a requisite quenching radius. As the temperature is increased, the probe has sufficient thermal energy to unwind. If the probe is designed to be complementary to a particular DNA target, it will bind to that target, if it is energetically favorable. When that occurs, the fluorophore and quencher are sufficiently separated such that there is appreciable fluorescence. In this way, these molecular probes can be used to associate particular fluorescence signatures with particular DNA targets.

Dual labeled nucleic acid probes can also be designed in another fashion. As the Taq polymerase elongates a strand, its exonuclease activity cleaves the nucleic acid probe containing both the

fluorophore and the quencher [26, 27]. Once the cleavage occurs, the quencher and fluorophore are no longer in close proximity at any temperature, and the fluorophore will exhibit a strong fluorescence signature. These probes are called TaqMan probes, and are a standard tool for reporting on PCR reactions. By carefully selecting both the fluorophore and the quencher that are conjugated to the nucleic acid strand, the emission signature can be controlled.

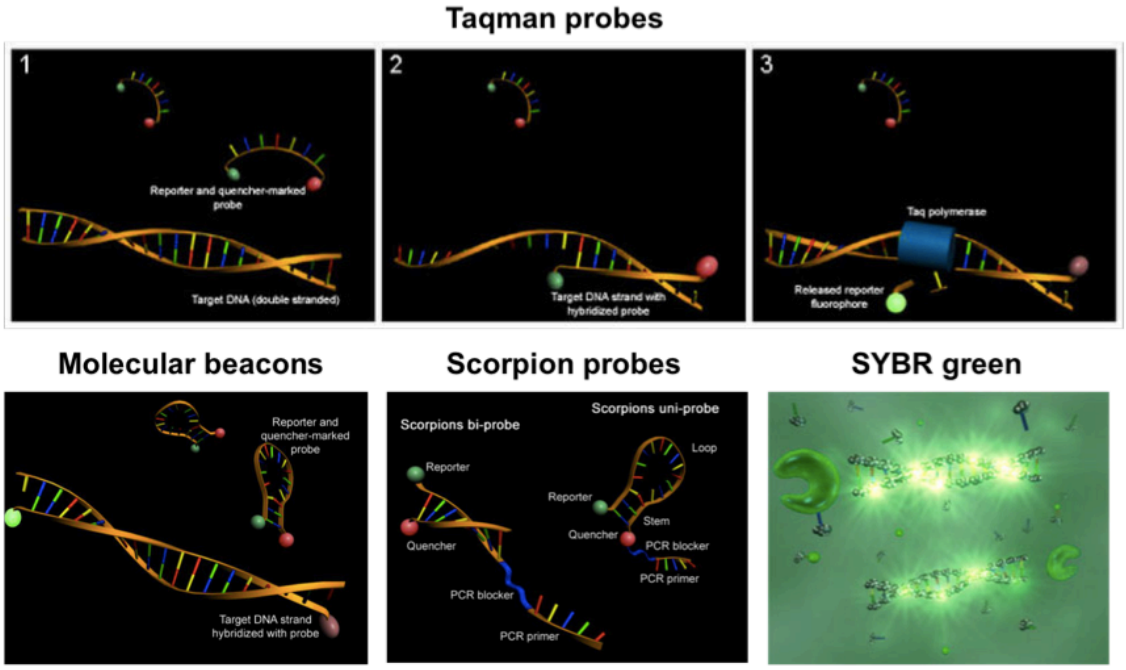

Figure 1.9 PCR reporting probes.

Multiplexed Reporting

Multiplexed reactions offer significant advantages and efficiencies, e.g. the use of the same chamber to run multiple reactions, the performance of parallel reactions on the same sample, and the ability to extract complex information from the sample in a fast and efficient way. However, to achieve these benefits and efficiencies, multiplexed assays require complex reporting mechanisms. These mechanisms involve coding of the "question" and decoding of the "answer" of the assay. Typical such mechanisms involve spectrally resolved fluorescence and chemiluminescence, or spatially resolved "single-color" assays, or temporally resolved, or by a combination thereof.

Standard DNA hybridization microarrays are an example of a spatially resolved multiplexed

assay where a single color is used for the detection (usually an intercalator dye). Single-chamber multiplexed PCR is an example of a spectrally encoded multiplexed assay, as the signal is collected from the same locus (e.g. the reaction chamber) but resolved spectrally as each PCR probe fluoresces in a different band of the spectrum. Sanger sequencing is an example of spectrally and spatially resolved multiplexed assay, as each terminated strand is coded with one of four fluorescence "colors" to report the terminating nucleic base, while the position of the base in the sequence is reported by the location of its fluorescence signal in the electrophoretic gel.

Fluorescence barcodes are also used, e.g. the Illumina system, where individual beads are coded with a combination of fluorescence probes, and then they are distributed across an array for individual decoupled readout. In the Helicos system for single molecule DNA sequencing, millions of strands are immobilized across a substrate and then sequencing-by-synthesis is performed by building the complementary strands using nucleotides tagged with one type of fluorescence dye per base type. The result is a spatially distributed array where spectral resolution determines the base, while temporal resolution produces the base location in the sequence by scan after every extension reaction.

Current PCR instruments and methods allow for the multiplexing reporting of PCR reactions by associating a particular wavelength fluorophore with a particular nucleic acid target. Regardless of the labeling strategy, the information from a single PCR reaction can be wavelength division multiplexed in this fashion.

In this thesis, we show that by selectively combining different fluorescent labels for a single nucleic acid target, we can identity a larger number of nucleic acid targets than the number of wavelength channels available. We demonstrate this technique by designing different two super-color codes for Taqman qPCR: error-correcting qPCR and binary-coded qPCR. The former has the benefit of using a biochemical checksum to ensure that a particular reaction has run to completion, while lowering the multiplexed capability of the super-color coded reaction. The latter code maximizes the number of targets that can be coded using this technique, by monitoring the intensity level in addition to the wavelength channel for particular target (Figure 1.10).

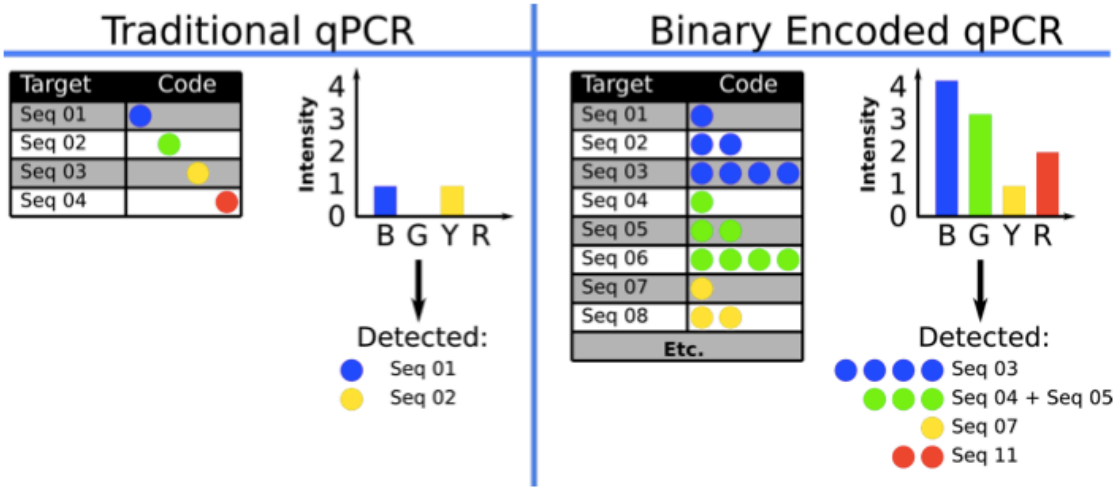

Figure 1.10 Binary-encoded PCR

Our coding/decoding technique offers an inexpensive way to multiplex through spectral resolution while avoiding the need for temporal and spatial resolution. More specifically, we offer a method to use fluorescence tags to overcome the multiplexing limitation to four colors with digestion probes in PCR, which is normally imposed by the wide emission spectra of standard fluorescence dyes. In this thesis, we explain the workings of the method, which would result in multiplexing to at least 6 independent readouts by fluorescence and an additional at least 3 readouts by fluorescence resonance energy transfer. We also explain how the two can be combined without crosstalk, resulting in an assay multiplexed to 9 independent readouts. Thus this method more than doubles the available bandwidth for multiplexing without requiring new instrumentation or expensive new reporting constructs. In fact, the implementation of the coding and decoding is rather straightforward and easily incorporated in modern assays.

Thesis Outline

In chapter two of this thesis we describe micro-scaled and nano-scaled platinum sensors for heating and thermometry. These sensors allows for highly localized temperature regulation, applicable for regulation of enzymatic processes like the polymerase chain reaction. We show that these heaters can also be used for on-chip IR spectra generation. In chapter three, we show how microfluidic fabrication techniques can be used to create a PDMS-based microfluidic blood filtration device. Such a device is applicable for the upstream sample preparation (e.g. sample filtration for DNA concentration) in a disease diagnostic platform. In chapter four, we describe

combinatorial codes for labeling and reporting on colorimetric assays such as ELISA and qPCR. In chapter five, we demonstrate fluorescence immunoassays in a miniaturized PDMS laboratory-on-chip. We show how the benefits in scaling geometries allows us to process 100 chemical reactions simultaneously. In chapter six, we report on a microfluidic immunoaffinity chromatography device that can be used to concentrate nucleic acid for downstream PCR analysis. In chapter seven, we describe the microfluidic evaporative coolers in PDMS. These coolers, for example, can be used to regulate the temperature of PCR reactions.

Chapter 2

MICROSCALED AND NANOSCALED PLATINUM SENSORS

Summary

We show small and robust platinum resistive heaters and thermometers that are defined by microlithography on silicon substrates. These devices can be used for a wide range of applications, including thermal sensor arrays, programmable thermal sources, and even incandescent light emitters. To explore the miniaturization of such devices, we have developed microscaled and nanoscaled platinum resistor arrays with wire widths as small as 75 nm, fabricated lithographically to provide highly localized heating and accurate resistance (and hence temperature) measurements. We present some of these potential applications of microfabricated platinum resistors in sensing and spectroscopy.

Introduction

Microlithography and nanolithography techniques can now be applied toward the miniaturization of a wide variety of sensors and actuators, leading to their integration into chip-based analysis systems. On-chip sensors enable the monitoring and regulation of many chemical and biological samples in parallel, and reduce the individual device cost, following the trend toward more complex and functional microelectronics through lithographic printing.

Platinum wires have been used for resistive heaters and incandescent light sources since the early 1820s. Platinum does not oxidize, making it a good candidate for vacuum-free, miniaturized visible and infrared sources, heaters, and thermometers. Applications of these microscale thermal control systems include chemical analysis, gas chromatography [30-33], microcalorimetry as well as thermal regulation of polymerase chain reactors [34] and even micropropulsion systems [35]. Miniaturization of these devices is particularly beneficial for systems that require independent thermal control over many reactions or wide band spectroscopic light sources; the low thermal mass of microfabricated heaters enables greater accuracy in measurement, faster heating and cooling rates, while requiring lower power than macroscopic systems.

Platinum resistance thermometer devices (RTDs) have a linear temperature response in the range

of −200°C to 500°C, and are well suited for the thermal measurement and control of wide array of chemical processes [34]. In particular, platinum RTDs exhibit a high accuracy and repeatability of temperature measurements when compared with thermocouples for temperatures below 600°C [36]. In this paper, we present on-chip thin-film, micron-sized platinum resistive thermometers as convenient on-chip thermal control systems and IR light sources.

Materials and Methods

We fabricated arrays of platinum microresistors and nanoresistors on alumina coated oxidized silicon wafer substrates. Fabrication starts with the growth of 160 nm of wet thermal oxide on a <100> silicon wafer. Subsequently, a 150 nm layer of alumina (Al_2O_3) and a 150 nm layer of platinum were sputter deposited on the surface using a direct current (dc) magnetron sputtering source [37]. The approximate film thicknesses were confirmed by scanning electron microscopy.

After the complete stack of materials was deposited, a milling mask pattern was then defined using standard photo-lithographic techniques. The resistor pattern was transferred by milling through the platinum and aluminum oxide, into the glass (to remove shunt thermal resistances), using a radio frequency (rf) plasma-based argon mill (Figure 2.1 top left inset).

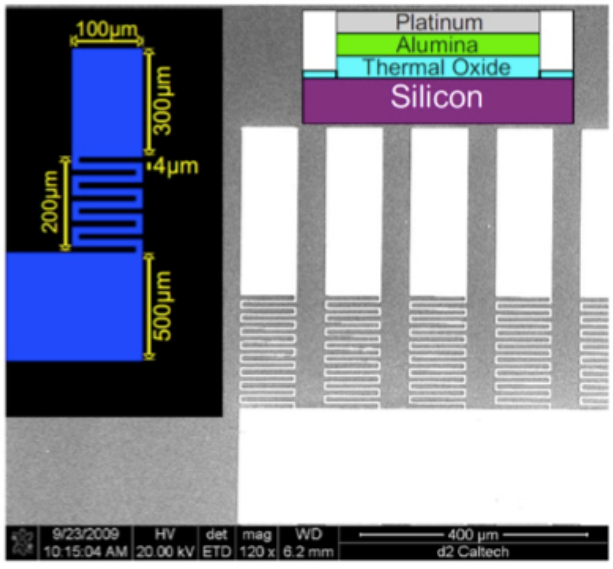

Figure 2.1 SEM image of Pt microresistors. Insets: cross-section (top right); dimensions (top left).

After the plasma- milling step, the cross-linked resist milling-mask was removed by exposing the

chips to a low- voltage rf oxygen plasma. These platinum resistors consist of a series of twenty serpentine platinum wires with 1-4 μm widths, and cover an area of 100 x 200 μm^2 on chip (Figure 2.1). Finally, selected microresistors were processed to create nanometer-wide "nanoresistors" (Figure 2.2) by using an FEI Nova 200 focused ion beam (FIB) system. The resistor linewidths were reduced from 1-4 μm to as small as 75 nm. This technique was utilized since it allows for mesoscaled structures to be fabricated using the same set of optical lithography masks.

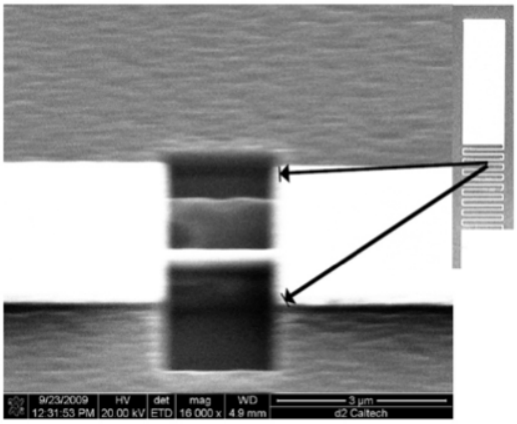

Figure 2.2 SEM image of Pt nanobulb (FIB-thinned microresistor).

Results and Discussion

Before temperature-benchmarking, the microresistors were annealed by resistive-heating with a constant power of ~1.5 W for 10 min to ensure thermal stability. These annealed resistors show considerably better relative tolerances on each chip than non-annealed resistors with a standard deviation of resistance σ=2.1% (sample size n=20) for annealed resistors and σ=48% (sample size of n=194) for non-annealed resistors. We believe that this annealing step allows the platinum thin-film to electromigrate in a controlled way and improves the reliability of the resulting heaters. This helps to minimize resistor failures during subsequent heating and measurement and has allowed the annealed resistors to be driven at higher power than non-annealed resistors.

To test the heating and temperature sensing capabilities of the resistors, a dc power supply was connected to the heater resistor and adjusted to deliver power in steps of 250 mW. The resistance of each adjacent resistor was manually probed and measured in order to characterize the thermal profile of a platinum resistor bank. By taking advantage of the linear temperature coefficient of

resistance (TCR) [0.003927 (Ω cm)/°C] [38] of platinum, we can relate resistance measurements of the platinum structure to the temperature of the substrate. The resulting temperature profile across the resistor array (Figure 2.3) shows that the temperature decreases with distance from the heating element and with decreasing heater power. Thermal isolation, provided by the SiO_2 film, ensures that the heating is confined to the surface Al_2O_3.

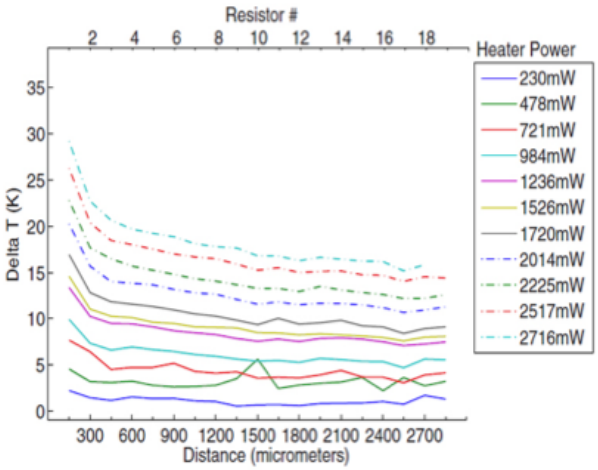

Figure 2.3 Temperature versus distance for resistor array for various driving powers. R0 is the heating element. R1-R9 are measurement elements.

Furthermore, the platinum resistor structures can be driven with enough power to exhibit luminescence in the visible range (Figure 2.4).

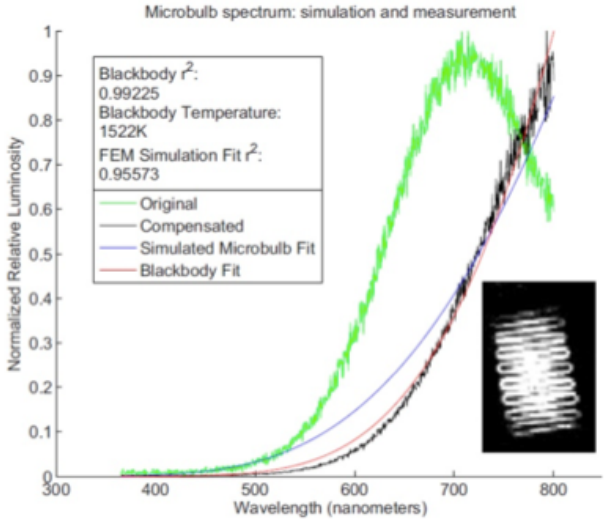

Figure 2.4 Normalized blackbody emission spectrum of Pt microbulb, and spectrum extracted by finite element methods.

This process can be enhanced by creating small, highly resistive regions within the platinum conductors. The intense localized heating of the platinum structures caused them to emit as blackbodies with components in the orange-red region of the visible spectrum. Spectra of light emission from these incandescent platinum filaments were extracted using an Acton cooled charge-coupled device camera. We compensated for the spectral sensitivity of the camera and optical system using a 3100 K near-blackbody light source. Furthermore, we were able to characterize the peak non-normalized (i.e., not corrected for detector optics) emission frequencies as a function of applied filament power across an individual resistor, and these have been summarized in Table 2.1.

Table 2.1 Peak emission wavelength vs power dissipation.

	Measured peak wavelength (nm)	***Input Power (W)***
Nanobulb	719.28	5.40
Nanobulb	718.02	5.92
Nanobulb	706.67	6.62
Nanobulb	701.62	7.22
Macrobulb	733.36	38.57

Using standard finite element analysis techniques, we were able to validate these spectral measurements. We modeled conduction, radiation, convection, and Joule heating using a nominal 1x1 cm chip with microresistors and a 5 W power source. Our model includes the chip mount used during the measurements, which was modeled as a heat sink with 9000 W/K m^2 (as measured). The simulated blackbody emission spectrum, produced using the surface temperatures created by the chip is shown in Figure 2.4. The simulated peak temperature was approximately 1900 K, slightly above the melting point of platinum. After optical compensation for our measured spectra, we found that the simulated peak and the predicted peak from Wein's law matched well with our measurements (Figure 2.4) [39, 40]. From these data, we conclude that the platinum filaments are heated slightly beyond their melting temperature, causing them to radiate in the near-visible and visible frequencies.

These high temperatures eventually led the bulb to failure, most likely caused by the melting and evaporation of the platinum from the substrate material. In the future, active cooling or physical confinement of the platinum through encapsulation might be employed to mitigate this failure.

Conclusion

The on-silicon fabrication of the resistive elements allows for integration of complex control circuitry for thermal control. For example, we envision that such a device can be used for applications such as microcalorimetry. These resistor arrays can be used to quantify the exothermic or endothermic nature of reactions. Ultimately, when electronics and fluidics are integrated with these platinum heaters, we envision these platinum resistance thermometers to be used within chip-based gas chromatography systems, accurate thermal controllers for microscopic polymerase chain reactors [41–43] and blackbody emitter light sources for visible and mid-IR spectroscopy [44–47].

Chapter 3

MICROFLUIDIC BLOOD FILTRATION DEVICE

Summary

Rapid decentralized biomedical diagnostics have become increasingly necessary in a medical environment of growing costs and mounting demands on healthcare personnel and infrastructure. Such diagnostics require low-cost novel devices that can operate at bedside or in doctor offices using small amounts of sample that can be extracted and processed on the spot. Thus, point-of-care sample preparation is an important component of the necessary diagnostic paradigm shift. We therefore introduce a microfluidic device which produces plasma from whole blood. The device is inexpensive, reliable, easy to fabricate, and requires only 3.5 kPa pressure to operate. The device is fully compatible with microfluidic diagnostic chips. The output 23- gauge microtube of the former can be directly plugged into the input ports of the latter allowing immediate applicability in practice as a sample-prep pre-stage to a variety of emergent microfluidic diagnostic devices. In addition, the shown approach of filter encapsulation in elastomer has principle importance, as it is compatible with and applicable to microfluidic sample-prep integration with analytical stages within the same elastomeric chip. This can eventually lead to finger-prick blood tests in point-of-care settings.

Introduction

Microfluidic technology allows for very precise manipulation of minute samples of fluid in controlled environments [48]. Furthermore, microfluidic chips can be mass-produced at low costs [48] and show potential as small, cheap, and low-powered devices for point-of-care medical testing [49]. Analytical microfluidic devices have already been demonstrated for antigen detection [50], viral detection [51], and quantification of various blood protein analytes in human serum [52] and human plasma [53].

However, such devices cannot be used directly with untreated patient samples because they are generally designed to operate with prepared serum or plasma, while the patient can only offer whole blood. As a result, traditional sample preparation techniques [54] have to be employed

first, e.g. coagulation and centrifugation for serum, and anti-coagulation and filtering for plasma. Thus, the complete diagnostic procedure cannot be fully miniaturized into a portable point-of- care format until sample preparation is miniaturized as well.

Such miniaturization is complicated due to the fact that serum preparation uses centrifugation to remove the coagulate, a technique that cannot be directly incorporated into a microfluidic chip. The alternative is to filter the coagulate, but this usually results in rapid clogging of the microfilter. Consequently, researchers have concentrated on the production of plasma on-chip, generally using poly(dimethylsiloxane) (PDMS) [55] as the material of choice, as PDMS is inexpensive, disposable, and chemically and biologically inert. The more recent results are encouraging [56-59].

However, the devices tend to produce only a relatively small amount of sample before becoming clogged [58], or they leak thrombocytes into the output [59], which might interfere with the proper function of the downstream diagnostic assay. In addition, such devices generally consist of filters sealed between layers of PDMS and/or glass, or the filter is defined in the PDMS itself before being assembled to the glass substrate [58, 59]. These configurations limit the filter surface (due to building the filter perpendicularly to the layer surface) and/or the applicable filtration pressure (due to the danger of sealing failure at the materials' interface in PDMS-glass devices).

Consequently, we have designed and fabricated a microfluidic blood filter tightly sealed within a single molded piece of PDMS. The device is integrated with an anticoagulant ethylene-diamine-tetra-acetic acid (EDTA) coated capillary tube. Whole blood from a single fingertip prick is passed through this tube and through specially-designed filter paper embedded in the PDMS device. The produced plasma exits through a 23-gauge steel microtube, allowing the device to easily interface with other standard microfluidic devices. In comparison to its microfluidic predecessors, the reported device has significantly increased the filtering area, making it less susceptible to clogging and enhancing its filtering capacity. Also, our device makes use of a more efficient filtering material, which further improves its overall filter characteristics. Finally, the complete encapsulation of the filter inside an elastomeric device makes it less susceptible to failure and leakage.

The reported device is also an important demonstration of a fully functional filter encapsulated in elastomeric devices. Such encapsulation allows for sample-prep and analytical devices to be

integrated within the same chip, eliminating the dead volume between sub-stages and eventually leading to point-of-care finger prick blood tests in fully integrated inexpensive analytical systems. The reported device is a technical step towards the future of biomedical diagnostics.

Materials and Methods

The PDMS blood filter is fabricated using polymer casting around a machined aluminum mold. Figure 3.1 depicts the mold alongside the finished device. The mold holds a membrane blood filter in place and defines a fluidic circuit between input and output ports compatible with commercially available anticoagulant finger prick blood draw capillary tubes and microfluidic 23-gauge tubes, respectively. The device is cast as a single piece.

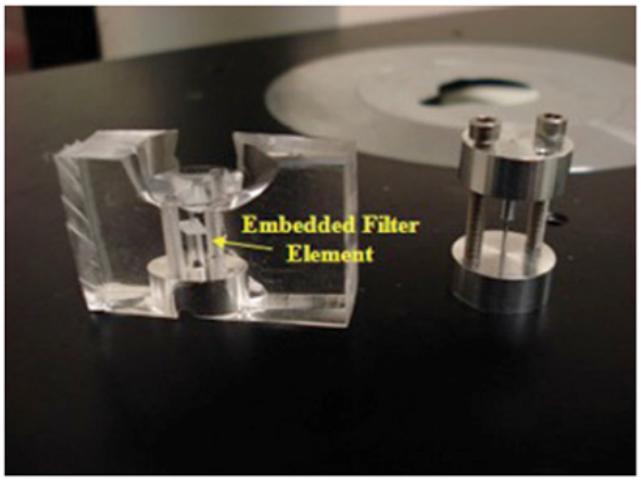

Figure 3.1 Aluminum mold and PDMS cast with filter material embedded.

A two-piece aluminum replica mold is connected with Allen bolts. The bottom piece contains a 24-gauge steel pin press-fit into the aluminum to mold a hole in the PDMS that seals tightly to the standard 23-gauge tubes typically used in microfluidic devices. The top piece consists of a cylinder designed to mold the PDMS in a fashion such that capillary tubes can be inserted and sealed. The top mold piece contains four holes, two of which are threaded and correspond to tapped holes on the bottom piece. These are used to compress the filter between the top and bottom cylinders, ensuring the creation of a leak-proof channel. The additional two holes are threaded and have no corresponding holes on the bottom piece. These are used to easily back the mold out of the PDMS when the casting process is finished.

The two rounds of the mold, which allow for the capillary tube integration and the 23-gauge pin interface, are connected and serve to compress the blood filter paper. The filter paper is then placed between the top and bottom pins, and Allen bolts are used to secure it in place. There are several inexpensive and readily available filter materials suitable for this device. The BTS-SP series from Pall Corporation (East Hills, NY) was used in fabrication and testing. The BTS-SP media (Figure 3.2, www.pall.com) features a highly asymmetric membrane engineered for plasma production from whole blood. The graduated pore structure of the filter consists of larger pores on the upstream side, with finer pores on the downstream side. This structure allows red and white blood cells to be captured in the larger pores while the plasma wicks into the smaller pores on the downstream side of the membrane. The large pore side of the media served as an absolute cell exclusion zone and performed very well in our device.

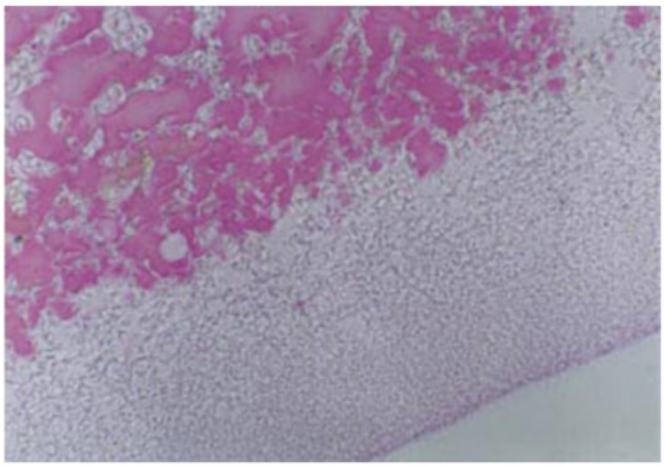

Figure 3.2 Micrograph of the BTS-SP filter based on asymmetry polysulfone membranes.

The PDMS device is cast in a procedure similar to conventional micro-soft lithography [60]. The mold is prepared and placed into a Petri dish. Uncured PDMS prepared in a 10:1 ratio is poured into the dish, covering the mold [60]. The dish is left to degas in a vacuum chamber to remove air bubbles from the PDMS mixture. The device is allowed to cure in an 80°C oven for one hour. The cured PDMS is removed from the dish and the device is cut from the underlying PDMS substrate. The Allen bolts holding together the cast are removed, bolts are inserted into the tapped separation holes, and the mold is slowly backed out of the PDMS. This allows the blood filter paper to remain intact within the microfluidic device. The choice of capillary tube is specific to the test carried out, as different anticoagulants are needed for different analyses. The capillary tube we used (StatSampler Capillary Blood Collectors from StatSpin, Iris Sample Processing,

Westwood, MA) had EDTA as an anticoagulant. These capillary tubes are used in medical facilities as a standard finger prick blood draw and are available with several different anticoagulant formulations.

Results and Discussion

Mouse blood was used to test the effectiveness of the device. Aliquots of the blood sample were stored at 4°C during testing; EDTA was used to prevent the blood from clotting when stored. When testing, 1 mL aliquots of mouse blood were drawn into a blood draw glass capillary tube inserted into the filter (Figure 3.3). The blood was forced through the filter under 3.5 kPa of dry nitrogen supplied by a hose attached to the capillary tube. This pressure was chosen to demonstrate that very little pressure is necessary to flow blood through the filter, and the blood filtered through very quickly under these conditions. The filter was able to collect 80-100% of the available plasma, typically half the total volume of the blood. As microfluidic applications generally require tens to hundreds of nano-liters of plasma for analysis [52, 53], our tests demonstrated this filter was capable of handling a volume of blood large enough for many uses.

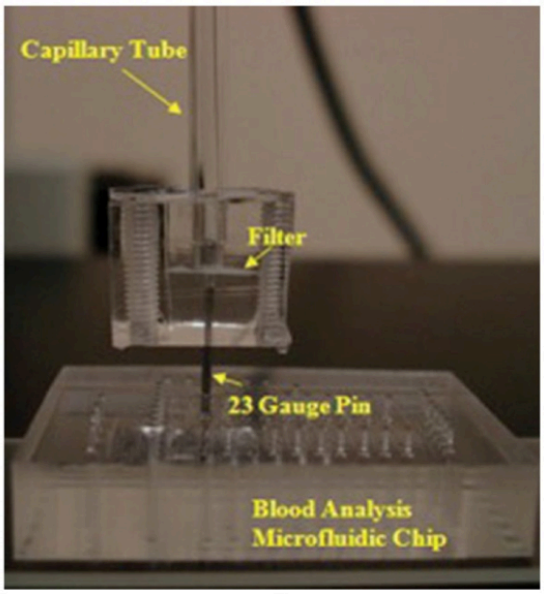

Figure 3.3 PDMS blood filter integrated with a blood-draw glass capillary tube and connected to a microfluidic analysis chip through a 23 gauge steel tube.

The filter was attached to a PDMS device containing a microfluidic channel 100 μm in width and 10 μm in height, through the 23-gauge interconnecting steel tube (Figure 3.3). At its upper end,

the tube is held tightly by the material of the filter device, while its lower end is held tightly by the material of the analytical device (Figure 3.3). Since these are very light structures, additional mechanical support was not necessary. Flow in the channel was imaged with blood both passed through the filter and without the filter. Figure 3.4 shows the blood sample with and without filtration, demonstrating successful cell elimination. The device filtered more than 2 mL without clogging. Based on our experience, we believe the limit of the current configuration is about 5 mL filtered before clogging.

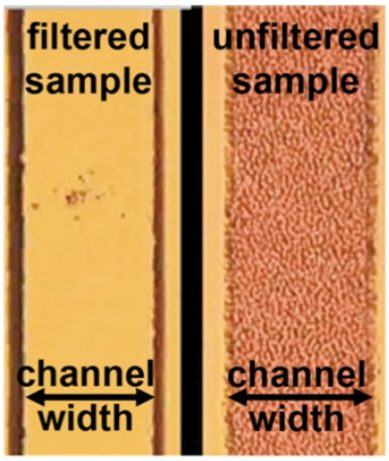

Figure 3.4 Comparison between filter output (left) and unfiltered whole blood (right) attests to the quality of the filtering. Each channel is 100 μm wide and 10 μm tall.

This design has important advantages over traditional planar microfluidic filters that rely on sealing blood filters between layers of PDMS, or PDMS and a solid substrate. Such devices can effectively use only the thinnest of filters, and require epoxy, thermal or plasma bonding to create tight seals, complicating fabrication and creating concerns of leakage. By contrast, the presented device can use a variety of filtering materials, making the filtering area less limited and increasing the overall reliability and robustness of the device. Finally, the casting method used allows for high reproducibility and low cost of production due to the low cost of PDMS and the reusability of the mold.

In principle, similar filtering systems can be assembled by combining commercial filters with macrofluidic components, e.g. luer-stub adaptors and connectors. However, each has a dead volume, which leads to losses of sample as a flat initial investment. In contrast, our method can be used to encapsulate the special filter membrane directly inside elastomeric microfluidic

devices by design and during the latter's fabrication. The long-term utility of such an approach will be the elimination of dead-volume losses and overall system integration and miniaturization. The result would be diagnostic systems where the sample-prep and the measurement stage are built inside the same disposable device by simple and economic means, while the elimination of many microliters of dead volume would mean the ability to use such devices for finger prick blood tests in point-of-care settings. Thus, the reported device and approach have important implications for the future of bioanalytical diagnostics.

The system integration described above would also make device fabrication more streamlined, as the process of encapsulation of the filter will be incorporated as part of the industrial fabrication of the overall device. For example, the filter could be sandwiched between consecutive layers in a multi-layer microfluidic chip. Alternatively, the filter can first be encapsulated into an elastomer slab as done here, and then be used as one of the layers in the overall multilayer chip. Both techniques are fully compatible with modern industrial approaches of microfluidic fabrication, e.g. such as successfully practiced by Fluidigm Corp.

Conclusion

We have demonstrated a simple, reliable, and disposable PDMS blood filter device that produces plasma from whole blood while using nominal positive pressure. Casting the device as a single piece ensures leak-free functionality without chemical sealants or complicated bonding procedures. Additional advantages include a larger filtering area, more efficient filtering material, and compatibility with conventional PDMS chips. It contributes as an important sample-prep function to microfluidic diagnostic systems, which promise to shape the future of biomedical diagnostics and healthcare.

Chapter 4

SUPERCOLOR CODING METHOD FOR LARGE-SCALE MULTIPLEXING OF BIOCHEMICAL ASSAYS

Summary

We present a method for the encoding and decoding of multiplexed biochemical assays. The method is the first to solve the degeneracy problem in "supercolor" coding. It allows for a theoretically unlimited number of independent targets to be detected and uniquely identified in any combination. Herein, we describe three coding schemes under the same method, and show experimental proofs-of-principle using Taqman PCR. Nonetheless, the method is not limited to PCR or fluorescence, but would benefit any assay whose reporting mechanism has "color" and "intensity", or their equivalents. The method enables the implementation of large panels of tests in point-of-care, near-patient, and low-resource biomedical diagnostics. Also, the method offers a remarkable increase in the productivity and information richness of existing PCR assays and systems, with correspondingly broad impact to clinical diagnostics and digital PCR.

Introduction

Multiplexed reactions offer significant advantages: the performance of parallel reactions on the same sample, the use of the same chamber to run multiple reactions, and the ability to extract rich information from the sample in a fast and efficient way. However, to achieve these benefits, multiplexed assays require complex reporting mechanisms: spectrally resolved fluorescence or chemi-luminescence (PCR, ELISA) [62], spatially resolved assays (microarrays, gel electrophoresis) [63], temporally resolved signals (capillary electrophoresis), or combinations thereof (Sanger sequencing) [64].

Among these, fluorescence has been the undisputed leader for the past 15 years due to its long list of desirable features: compatibility with biochemical assays, small size of the labels, easy conjugation to molecules of interest, affordability, low toxicity, stability, robustness, detectability with inexpensive optics, and ability to be combined with spatial arrays. However, fluorescence-based multiplexing has been limited by the large width of the emission spectra of standard fluorophores, and by the requirement to minimize spectral overlap among the probes, so that

measured signal can be correctly decoded into a unique outcome [65].

As a result, the typical coding scheme has been to assign one color per target, i.e. M=N, where M is the multiplexing factor and N is the number of independent "colors". With standard fluorophores, this has meant that only 4 to 6 questions are typically asked of the same sample at the same time [66, 67]. Wherever higher factors of multiplexing are required, the solution has been to combine fluorescence with aliquoting, spatial arraying, or sequential processing [68]. However, those lead to labor-intensive workflow and/or significantly more expensive and bulkier systems. Thus, it would be highly beneficial if the multiplexing factor were increased through spectral coding only.

Early attempts at "supercolor" multiplexing (M>N) have been only partially successful. "Chromosome painting" [69] allowed for FISH-based identification of 24 chromosomes, while two PCR Taqman-based schemes could identify eight foodborne pathogens [70] or fifteen types of HPV [71]. However, the first scheme made use of the application-specific condition that each chromosome was also spatially resolved from the others, while the other two schemes assumed that no more than one of the targets is present at a time. If these restrictions are relaxed, all three schemes produce "degeneracy", i.e. the same test result decodes into more-than-one possible outcomes. A general multiplexing scheme (e.g. coding for panels of infectious diseases, drug-resistant bacterial strains, foodborne pathogens, or genetic markers) cannot allow ambiguity of outcome and cannot assume that only one target is present at a time.

Herein we report on a novel coding method that is the first to solve the degeneracy problem and thus the first to ensure the unambiguous identification of any combination of present targets. Also, its multiplexing factor M is mathematically unlimited and is practically much larger than the number of available colors (M>>N). Thus our method is a major breakthrough in the field.

As the method uses standard fluorophores and oligos, it is easily implemented with the existing oligo-synthesis techniques and measurement infrastructure. Once applied in practice, the method would produce a major increase of the productivity of the existing fleet of machines (e.g. for PCR, qPCR, digital PCR) as no changes in the hardware would be needed to accommodate the new multiplexing capabilities.

In clinical diagnostics, splitting a profuse sample into aliquots and testing each aliquot for a

different target is a valid if expensive and labor-intensive multiplexing strategy [72-80]. However, the amount of sample is rather limited in point-of-care diagnostics [81], while the viral load in a positive patient can be very low. As a result, any splitting is undesirable, because the resulting amount of analyte in each aliquot may fall below the detection limit of the assay. In contrast, our method would pose multiplexed questions to the whole sample, thus avoiding aliquots and the loss in sensitivity. Hence, our method is particularly significant to point-of-care PCR assays, where it would also allow for cheap disposables to test for large panels of infectious diseases and multiple strains of drug-resistant bacteria. The low cost of its implementation makes it even more important to diagnostics in low-resource settings.

Materials and Methods

Five nucleic acid pathogens of clinical relevance were chosen for this study: Human Immunodeficiency Virus 1 (HIV-1), Plasmodium falciparum (Malaria), Herpes Simplex Virus-2 (HSV-2), Mycobacterium tuberculosis (TB), and Dengue Virus Type 3 (Dengue Fever). Two targets of diagnostic relevance on the HIV-1 genome [82-85] *(26–29)*, p17 and poly protease, were selected from the Los Alamos National Laboratory HIV-1 reference sequence [86] *(30)*. A diagnostic sequence from the Malaria falciparum ChR7 gene [87, 88] *(31, 32)* was obtained from the UCSC Plasmodium falciparum Genome Browser [89] *(33)*. A sequence for Herpes Simplex Virus-2 [90] *(34)* was synthesized from the sequence obtained from the European Molecular Biology Library [91] *(35)*. Similarly a diagnostic sequence for rpoB gene in Mycobacterium tuberculosis [92-94] *(36–38)* was synthesized from a sequence obtained from the European Molecular Biology Library [95] *(39)*. A PCR diagnostic sequence for Dengue Virus Type 3 [96] *(40)* was obtained from the National Institute of Health genetic sequence database [97] *(41)*.

All oligonucleotides were synthesized by Integrated DNA Technologies (Coralville, Iowa). Diagnostic sequences were input into IDT's OligoAnalyzer 3.1 tool. Probes and primer pairs for each target were chosen, from the OligoAnalyzer's set of generated sequences, to minimize homology with un-intended targets, probes and primers. TaqMan sense probes for all targets were synthesized with a fluorophore at the 5' end and a quencher at the 3' end. Sequence information is tabulated in Appendix A Tables S-3 to S-8. Nucleic acid products were synthesized and lyophilized by IDT. These products were reconstituted with TE buffer and aliquoted for experimental use.

Results and Discussion

The crux of our method is the combined use of "colors", the multiplicity of signal intensity, and mathematical strategies to circumvent degeneracy and ensure an infinite number of unique codes that can be unambiguously decoded in any combination of occurrence. While the method is not limited to fluorescence, PCR, and Taqman probes [98], they are the natural choice as a system for proof of principle for the method.

Taqman probes are short pieces of DNA that have a fluorophore on one end and a quencher on the other end. If the target sequence is present, the probe and primer hybridize to it. As the polymerase extends the primer, its 5' exonuclease activity breaks up the probe sequence. The released fluorophore and quencher separate by diffusion, and so the fluorophore emits fluorescence signal. Conversely, if the target sequence is not present, the probe remains intact, so the quencher prevents fluorescence emission. The end result is a strong fluorescence signal when the target is present and a weak or no signal when the target is not present.

Standard fluorophores have wide emission spectra, so to avoid overlap and false positives, only a few colors (typically four) are used simultaneously in multiplexed assays. Each color is assigned to a different Taqman probe. Then, the presence or absence of a sequence is judged by the fluorescence signal in the respective color. For example, if the color set is named {blue, green, yellow, red} by excitation, a traditional experimental result of 1100 means the sequences coded by blue- and green-excited fluorophores are present, while the other two are absent.

Unlike the traditional approach, our method generally uses more than one color per sequence. Table 4.1 shows one such coding scheme in four colors.

Table 4.1 Combinatorial coding of Targets

Sequence	B	G	Y	R
Control Z	1	0	0	0
Sequence A	1	0	0	1
Sequence B	1	0	1	0
Sequence C	1	1	0	0
Sequence D	1	0	1	1
Sequence E	1	1	0	1
Sequence F	1	1	1	0
Sequence G	1	1	1	1

Code 1000 is assigned to a control sequence Z that will always be present and should always amplify [99]. All sequences have a probe in the control color. This design ensures that the multiplicity of the signal intensity in the "control" color reports the number of unique sequences that have successfully extended and are thus present in the sample.

Mathematical symmetry dictates that any color can be the control color. However, as the highest multiplicity would likely be observed in the control color, it makes sense to choose it to be the color that is best detected in the particular system. The Roche Lightcycler 480 used for the experimental proof has only a blue excitation, while the other colors count on wide excitation tails. Hence, blue was the logical choice here.

The possible measurement results and their decoded meaning in terms of sequences present are shown in Table 4.2. Three conditions have been stipulated: First, the positive control always produces a positive outcome, i.e. it works appropriately. Second, in each color, the signal is additive and scales in the same way with probe concentration, regardless of which probe it comes from. Third, in each color, each probe produces the same unit of signal. Essentially, this means the signals are additive and digital. Ensuring the first condition is just a matter of proper preparation of the assay. The second condition is attainable under fluorescence. In practice, the third condition need only be approximately right, as we show further below.

A measurement outcome is denoted as a sequence of signal multiplicities in the respective "colors". Each multiplicity is calculated within its own color. For example, outcome 4321 means the sample's measured intensities are 4x in blue, 3x in green, 2x in yellow, and 1x in red. This outcome is valid, because it can be achieved by adding sequence codes from Table 4.1, so it is found in the decoding Table 4.2. It produces the answer ZCFG, which means only sequences Z, C, F, G are present. Conversely, the outcome 4000 is invalid, because it cannot be achieved by adding sequence codes from Table 4.1 in a digital fashion, and thus is not listed in Table 4.2. An invalid outcome means that the assay malfunctioned in the particular experiment. This logic filter provides a powerful tool for judging the validity of experimental results.

Table 4.2 Exhaustive combinations of codes

B	G	Y	R	Read
1	0	0	0	Z
2	0	0	1	ZA
2	0	1	0	ZB
2	1	0	0	ZC
2	0	1	1	ZD
2	1	0	1	ZE
2	1	1	0	ZF
2	1	1	1	ZG
3	0	1	1	ZAB
3	1	0	1	ZAC
3	0	1	2	ZAD
3	1	0	2	ZAE
3	1	1	1	ZAF, ZCD, ZBE
3	1	1	2	ZAG, ZDE
3	1	1	0	ZBC
3	0	2	1	ZBD
3	1	2	0	ZBF
3	1	2	1	ZBG, ZDF
3	2	0	1	ZCE
3	2	1	0	ZCF
3	2	1	1	ZCG, ZEF
3	1	2	2	ZDG
3	2	1	2	ZEG
3	2	2	1	ZFG
4	1	1	1	ZABC
4	0	2	2	ZABD
4	2	2	0	ZBCF
4	2	0	2	ZACE
4	1	1	2	ZABE, ZACD
4	1	2	1	ZABF, ZBCD
4	2	1	1	ZACF, ZBCE
4	1	2	2	ZADF, ZABG, ZBDE
4	2	1	2	ZACG, ZCDE, ZAEF
4	2	2	1	ZBCG, ZBEF, ZCDF
4	2	2	2	ZCDG, ZAFG, ZBEG, ZDEF
4	1	1	3	ZADE
4	1	3	1	ZBDF
4	3	1	1	ZCEF
4	1	2	3	ZADG
4	3	2	1	ZCFG
4	2	1	3	ZAEG
4	2	3	1	ZBFG
4	1	3	2	ZBDG
4	3	1	2	ZCEG
4	2	2	3	ZDEG
4	2	3	2	ZDFG
4	3	2	2	ZEFG

B	G	Y	R	Read
5	1	2	2	ZABCD
5	2	1	2	ZABCE
5	2	2	1	ZABCF
5	2	2	2	ZABCG, ZABEF, ZBCDE, ZACDF
5	1	2	3	ZABDE
5	2	1	3	ZACDE
5	1	3	2	ZABDF
5	2	3	1	ZBCDF
5	3	1	2	ZACEF
5	3	2	1	ZBCEF
5	2	2	3	ZABEG, ZACDG, ZADEF
5	2	3	2	ZABFG, ZBCDG, ZBDEF
5	3	2	2	ZACFG, ZBCEG, ZCDEF
5	1	3	3	ZABDG
5	3	1	3	ZACEG
5	3	3	1	ZBCFG
5	2	3	3	ZADFG, ZBDEG
5	3	3	2	ZBEFG, ZDEFG
5	3	2	3	ZCDEG, ZAEFG
5	2	2	4	ZADEG
5	2	4	2	ZBDFG
5	4	2	2	ZCEFG
5	3	3	3	ZDEFG
6	2	2	3	ZABCDE
6	2	3	2	ZABCDF
6	3	2	2	ZABCEF
6	2	3	3	ZABCDG, ZABDEF
6	3	2	3	ZABCEG, ZACDEF
6	3	3	2	ZABCFG, ZBCDEF
6	4	3	2	ZBCEFG
6	4	2	3	ZACEFG
6	3	3	3	ZABEFG, ZACDFG, ZBCDEG
6	3	4	2	ZBCDFG
6	2	4	3	ZABDFG
6	3	2	4	ZACDEG
6	2	3	4	ZABDEG
6	4	3	3	ZCDEFG
6	3	4	3	ZBDEFG
6	3	3	4	ZADEFG
7	4	4	3	ZBCDEFG
7	4	3	4	ZACDEFG
7	3	4	4	ZABDEFG
7	4	3	3	ZABCEFG
7	3	4	3	ZABCDFG
7	3	3	4	ZABCDEG
7	3	3	3	ZABCDEF
8	4	4	4	ZABCDEFG

Table 4.2 shows all the valid answers, and thus it is the exhaustive set for the encoding Table 4.1. To see this, let's go through the decoding Table 4.2 rank-by-rank. "Rank" is defined as the number of present sequences, which under the encoding Table 4.1, is equal to the multiplicity of the blue bin. The lowest rank is 1, with a single valid outcome of 1000 and a test result of Z. This means only the control sequence was present. At rank 2, the control sequence and one other are present, so there are 7 such cases. At rank 3, the control sequence and two other sequences are present, so the number of distinct results is a combination of 7 choose 2, or 7!/(5! * 2!)=21. At rank 4,5,6,7, and 8, the number of distinct results is 35, 35, 21, 7, and 1, respectively. Table 4.2 shows the same numbers of results in each rank, so the table is exhaustive.

In "supercolor" multiplexing, degeneracy is the phenomenon wherein the same valid outcome corresponds to multiple distinct combinations of present sequences [70, 71]. For example, outcome 5233 in Table 4.2 is degenerate, because it can be decoded as either ZADFG or ZBDEG. As a counterexample, outcome 3110 is not degenerate because it is decoded to a single result (ZBC).

It turns out degeneracy can be eliminated. For example, outcome 4112 is valid and can be decoded as either ZABE or ZACD. So, if we drop sequence D from the set, the test result ZACD is no longer possible, so the only remaining test result associated with outcome 4112 is ZABE. Using this idea, we have found out that dropping any two of {D, E, F} completely eliminates degeneracy, while the coding remains "supercolor" (M>N) as 6 sequences are unambiguously identifiable in any combination while using just 4 colors.

To demonstrate the scheme experimentally, we chose representative sequences from important diseases and designed respective primers and probes labeled with FAM, Cy3, ROX, and Cy5. The chosen coding was 1000 (HIV PolyProt), 1100 (HIV P17), 1010 (malaria), 1001 (herpes), 1101 (tuberculosis), and 1111 (dengue). We ran separate positive controls for each sequence, as well as the full panel for several combinations of sequences present. The experimental details are in the supplemental materials.

The signals of the positive controls were added to produce the expected cumulative signal for every possible combination of present sequences, in each color. Each expected cumulative signal was plotted as its own level in a "chromatogram". Expected cumulative signals corresponding to combinations of the same rank in the same color were organized into their own "band". Doing

this for all colors produced a level and band structure, against which the experimental results of each combination could be judged. Figure 4.1 shows the chromatograms of experimental combinations 4112, 3121, and 3102. The experimental results for each combination in each color are shown by black dots.

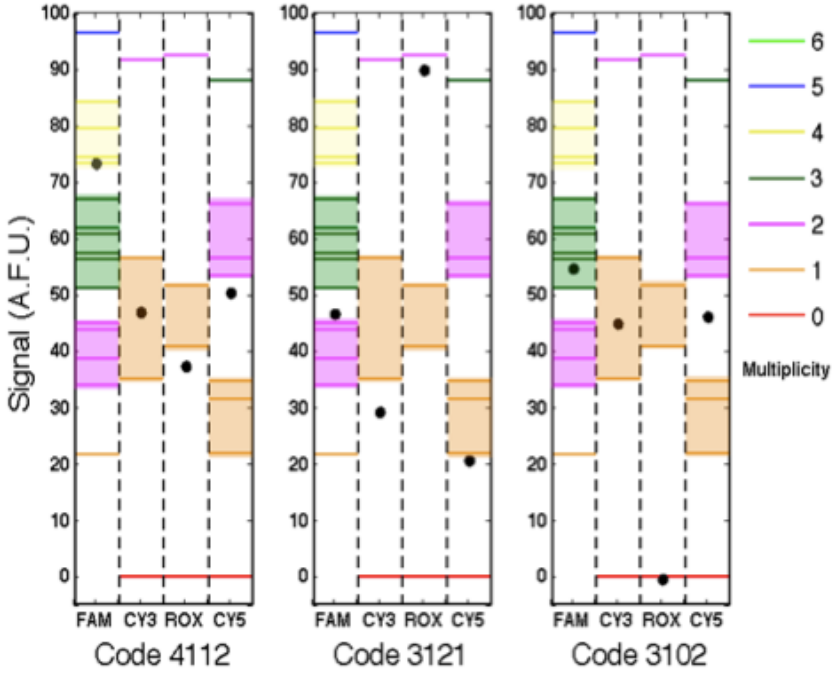

Figure 4.1 Chromatogram of multiplexed experiments.

"Calling" the results to determine multiplicity in each color relies on three criteria: First, the analog result of fluorescence signal must be converted into a digital result of the multiplicity. So, if the dot falls inside a band, then the multiplicity of that band is the answer. If a dot is in between two bands, the result can be either multiplicity but not both. Second, illegal results can be excluded or considered a failed experiment. Third, if the dot is between two legal results, the "called" result is the one whose band is closer to the dot.

Using these criteria, the first experiment is "called" 4112, which is the correct answer. The second experiment should be "called" 2121 or 3121, but 2121 is illegal, so the result must be 3121, which is the correct answer. The third experiment is 3102 or 3101, both of which are legal, but the dot is clearly closer to 3102, so that should be the call, and that is the correct answer. These results provide an experimental demonstration and proof-of-principle for our coding method.

The results show a trend of slightly lower combined signal than what would be expected from a simple summation of positive-control signals. This leads us to believe that the combination is not perfectly linear, so there are additional effects, for which the chromatogram construction does not account at present. We conjecture that this particular effect has to do with the absolute concentration of quenchers. The higher the absolute concentration of quenchers, the larger the percentage of reaction volume they "black out", so the same percentage of released fluorophores fails to contribute to the cumulative signal. One solution is to use low concentrations of probes, so that the percentile loss is negligible, regardless of how much of the quencher is released. This issue is a subject of ongoing research.

Figure 4.1 shows that each rank containing multiple combinations has a relatively wide band. The width of the band is ultimately the difference between the highest and lowest cumulative signals. If all positive controls in the particular color produced exactly the same fluorescence signal, then the width of each band would be zero. Since instead those signals are somewhat different, the resulting bands are relatively wide. Fortunately, there is a simple means to tighten the bands. Instead of loading all probes at the same concentration as we did here, each probe concentration can be adjusted so that the end-point fluorescence intensity of each positive-control, in every color, is the same. This approach would significantly tighten the bands, making calling easier.

The coding method can be further improved by switching to a single hybridization probe per target sequence. To maintain the coding in Table 4.1, each such probe would be present with corresponding color labels at the concentrations prescribed by the band-tightening optimization above. Making one sequence, aliquoting it, and labeling each aliquot with a corresponding color, is far less expensive than making multiple sequences each with its own color. As a result, the overall coding scheme is far cheaper to deploy in this second modality. Furthermore, it is far easier to fit just one hybridization probe to a target sequence, than two, three, or four.

Under the coding scheme of Table 4.1, the maximal-multiplicity combination is 6323, which means all coded sequences are present. On the other hand, Table 4.1 has the tacit restriction that each sequence can have only 1x signal in any color. If we relax that restriction, we can add a sequence 1X00, which preserves the sequence counting property in the blue color. What is the minimal X, such that the new addition preserves the general structure of Table 4.2, keeps degeneracy broken, and offers a new tier of multiplexing? The answer is $X_{min}=4$. Basically, X

has to be the maximal previous cumulative multiplicity plus 1. Then any answer of 0-3 in the green digit is interpreted as before and means sequence 1400 is not present, while any answer of 4-7 in green means 1400 is present and the full answer must have 1400 subtracted from it to obtain the rest of the present sequences using Table 4.2.

Obviously, this system can be analogously expanded with additional sequences 1030 and 1004, for yellow and red, respectively. An analogy with Table 4.1 coding then suggests additional sequences 1404 and 1434. Iterating the same idea to the third tier will lead to further added sequences of 1800, 1060, 1008, 1808, and 1868. Thus, if just 3 tiers are used, the total number of sequences that are unambiguously identifiable in any combination, is 5x3=15, while the maximal-multiplicity result would be 16-39-14-39, when all sequences are present.

This expansion of the Table 4.1 coding offers theoretically infinite number of additional sequences that can be unambiguously identified in any combination. However, there are practical limitations on the assay, e.g. the ability to tell the difference between bands B and B+1 in the multiplicity call. Thus practically, there is a limited multiplicity bandwidth to be utilized by any coding scheme. Hence, the most efficient scheme is the one that uses that bandwidth most sparingly, so that M is maximized for a fixed B_{max}.

These ideas lead to the following third coding scheme. Each sequence has one probe with only one color. The sequences of each color are coded by the multiplicities of their probes. The first few sequences in blue are 1000, 2000, 4000, 8000. Similarly, the first few sequences in green are 0100, 0200, 0400, 0800. This scheme is theoretically infinite as before, but it allows for more sequences per unit multiplicity bandwidth. For example, if we take the first 4 tiers, the number of unambiguously identifiable sequences in any combination are 4x4=16, while the “all-present” outcome is 15-15-15-15. This third scheme is better than the second scheme in terms of bandwidth density and practicability, but it does not possess the self-correcting qualities of the first and second schemes. We call this third scheme “binary” as the coded intensities correspond to single digits of different orders in binary counting.

To test the binary scheme experimentally, we chose to use three sequences, Dengue Virus, HIV TPP, and HIV P17, in just one color (blue). The fluorescence signals from their probes in positive-control end-point PCR reactions were measured and used to calculate the respective probe concentrations that would produce a 1x, 2x, and 4x signal intensity, respectively. Then all 7

non-null combinations of target occurrence were processed in a batch experiment using the same Masterplex mixture of primers and probes. The fluorescence signal of each case was plotted in a chromatogram (Figure 4.2). The multiplicity levels were assembled as the expected integer multiples of the 1x signal intensity, while their widths were calculated as the propagated uncertainty of the 1x measurement. That uncertainty was equated to the standard deviation of the fluorescence signals of the last five PCR cycles in saturation.

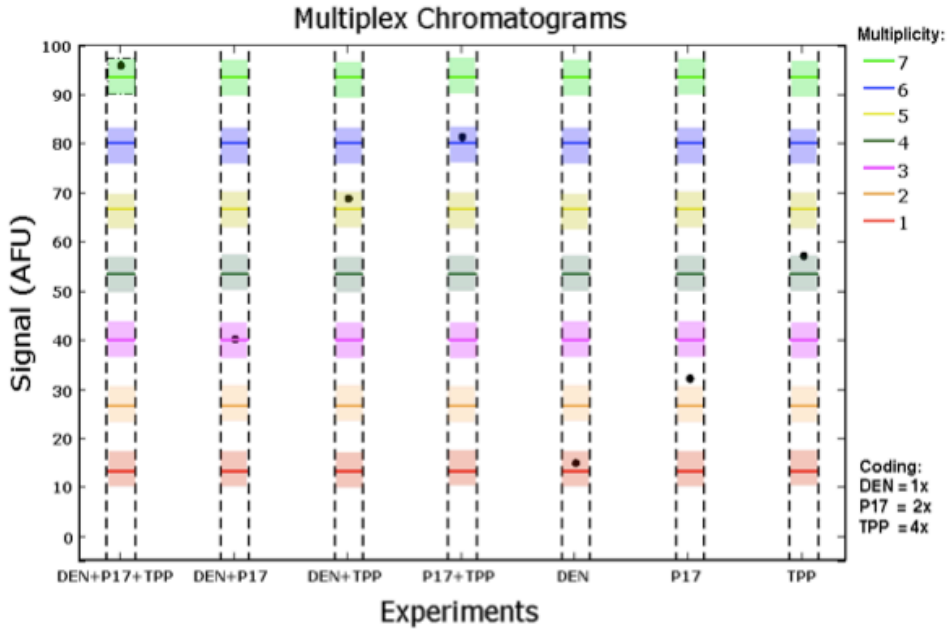

Figure 4.2 Chromatogram of binary coded multiplex experiments in FAM

The results in Figure 4.2 show a virtually perfect agreement between expectations and experiment. In every case, the result correctly decodes to the exact list of present sequences. Furthermore, the experimental set is exhaustive, as all theoretical combinations are accounted for and measured for the case of 1 color and 3 sequences. These results show proof of principle for the binary coding scheme.

Conclusion

The so-far described schemes all utilize standard fluorescence. However, fluorescence resonance energy transfer (FRET) can be used in conjunction with standard fluorescence to enlarge the set further. FRET-based Taqman probes [100] function in essentially the same way as standard

Taqman probes but have an orthogonal spectral output, because they emit one step further into the larger wavelengths. Thus if fluorescence interrogation of the sample is performed one color at a time, the signal from the standard probe will be shifted by one step but the signal from the FRET probe will be shifted by two steps. Then, detecting in each spectral band separately will produce independent signals. The same coding as described above can then be independently and simultaneously applied to the FRET probes. This should double the number of sequences that are unambiguously identifiable in any combination. So, for the third scheme used to the fourth tier, this means 4x4x2=32 sequences in the set. The tradeoff is that the analyzer systems would have to be FRET-capable. That limits usability with systems already embedded in practice, but the large gain in multiplexing would more than justify the feature in emerging systems.

Our method of coding is a universal solution for systems limited by the requirement to fit multiple reporters within a certain bandwidth while avoiding overlap, crosstalk, and false positives. Thus the particular coding shown in Table 4.1 for four basis "colors" is just one of the possibilities under the general method. If the basis "color" set is expanded, e.g. by future fluorophores with tighter emission spectra, the described coding method is still fully applicable and will offer larger multiplexing factors. Thus the fundamental utility of the coding method will grow further with advances in probes.

Also, while we discuss standard fluorophores as the reporter molecules, the same coding idea can be used with other systems, e.g. chemi-luminescence, or in fact any quantitative reporting where the output signal scales with the constituent signals of the same color, frequency, physical size, absorption band, etc. The cumulative signal does not have to be digital or scale linearly with number and intensity of constituent signals. For example, if the physical principle of measurement is absorption, the cumulative attenuation is a product of constituent attenuations while the concentrations are additive, due to the exponential nature of Beer-Lambert's law. The logarithm of the cumulative attenuation will then scale linearly with constituent concentrations in each absorption band (the equivalent of color), so the same multiplexing method is still applicable.

While our description focused on multiplexed end-point PCR for qualitative panels, the same method can be applied to certain types of qPCR. Digital PCR systems (e.g. BioRad's digital droplets and Fluidigm's dynamic arrays) produce highly sensitive quantification of copy

numbers, and so are qPCR systems by output, but their actual mode of operation is end-point PCR [101, 102]. This means that our presented method can be immediately integrated into those systems and would drastically expand their productivity.

Furthermore, we can confidently prophesy that the presented multiplexing method would work within traditional real-time PCR. First, the real-time data would be fully recorded as the PCR runs to completion. The end-point values would be decoded into the list of present sequences. Second, individual Ct's can be gleaned in each color by detecting the maxima of the second derivative of the real-time curve in that color. Third, as a particular sequence gets amplified, fluorophores are released from its Taqman probes in the same ratios as the color multiplicities in the coding of that sequence. That is so because the amplification breaks up the same probe and thus has no bias among the colors for that sequence. Hence, e.g. under the second coding scheme, 1100 will have the same Ct in blue and green, while 1400 will have its green Ct precede its blue Ct by 2 cycles. This set of clues should be rich enough to decipher the identity and starting quantity of each present sequence.

Finally, the applicability of the method is not limited to PCR or even biochemical assays. Any qualitative test producing a fixed amount of signal that is independent of the starting amount of the test's target, is subject to the same mechanic and thus can benefit from this multiplexing method. If there is a "spectral" dimension to the physical basis of the test, the concept of "color" would apply, and thus the presented mathematical apparatus can be engaged to full force. If there is no "spectral" dimension, single-color multiplexing is still applicable, e.g. using the binary scheme presented here.

Chapter 5

FLUORESCENCE IMMUNOASSAYS IN MICROFLUIDIC ELASTOMERIC CHIPS FOR PORTABLE DIAGNOSTICS OF MULTIPLE SCLEROSIS

Summary

Herein we experimentally explore the possibility of rapid diagnostics and frequent monitoring of multiple sclerosis by using microfluidics to detect MMP-9. We demonstrate detection with SNR>10 using high-throughput microfluidic elastomeric chips with inbuilt fluorescence sandwich immunoassays. Our research shows the limit of detection is at least as low as 65 nM. Our results establish feasibility and form a solid basis for future R&D in this biomedical application.

Introduction

Multiple sclerosis is a debilitating auto-immune disease that affects the function of the central nervous system (CNS). The patient's own immune system targets oligodendrocytes cells that are responsible for the myelination of neural axons. The immune response critically damages oligodendrocytes, halting production of myelin and leading to the rapid demyelination and eventual disintegration of the axons. Ultimately, the affected neurons lose the ability to conduct electrical impulses [103].

Diagnosis of multiple sclerosis is done through characterization of the symptomatic response, which varies with each patient. More common symptoms, associated with the loss of neural function, include fatigue, numbness, spasticity, vision loss, and depression. Most patients fall into one of the four identified symptom motifs for multiple sclerosis: relapsing-remitting (RR), primary-progressive, secondary-progressive, and progressive relapsing (Figure 5.1).

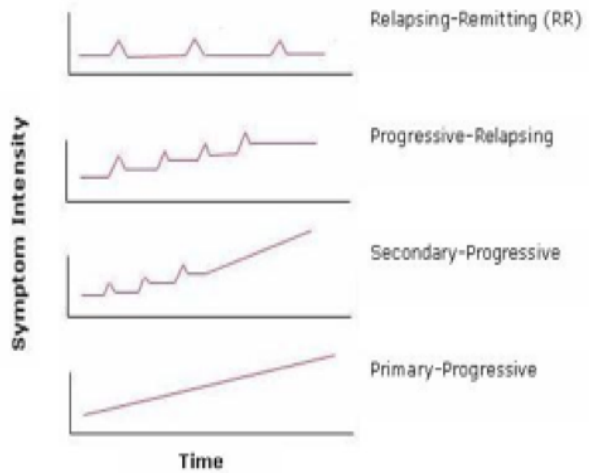

Figure 5.1 Multiple sclerosis symptom motifs

Approximately 85% of multiple sclerosis patients are initially diagnosed as relapsing-remitting; characteristics of these patients include episodes of acute symptoms followed by remissions of partial to complete recovery. Within ten years of the initial diagnosis about 50% of RR patients go on to exhibit secondary-progressive multiple sclerosis, which is characterized by a steady increase in symptom intensity with brief periods of acute symptoms and recovery [104]. A smaller percentage of patients, diagnosed as primary-progressive, exhibit a steady increase in symptom intensity from the onset of the disease. However, a very small percentage of patients with multiple sclerosis demonstrate a progressive relapsing syndrome, wherein symptom intensity steadily increases along with intermittent periods of partial recovery.

Currently, there is no definitive serological test for multiple sclerosis. However, recent research has demonstrated the existence of specific biological markers for multiple sclerosis, which include matrix metalloproteinase 9 (MMP-9), a gelatinase enzyme that has the ability to cleave myelin [105], and Galactocerebroside (GalC), a transmembrane glycoprotein in oligodendrocyte cells that is a known target for demyelinating antibody responses [106, 107]. Furthermore, these markers have a demonstrated presence in the blood stream, making them promising candidates for immunological testing.

Herein we experimentally explore the possibility of rapid diagnostics and frequent monitoring of multiple sclerosis by using microfluidics to detect MMP-9. We demonstrate successful detection with signal to noise ration (SNR) greater than 10 using high-throughput microfluidic elastomeric chips with inbuilt fluorescence sandwich immunoassays. Our research suggests the limit of

detection is at least as low as 65 nM. Our results establish feasibility and form a solid basis for future R&D in this biomedical application.

Materials and Methods

A high-throughput immunoassay chip (Figure 5.2) [108] was used to perform the microfluidic immunoassays. Soft lithography was used to fabricate the chips in polydimethylsiloxane (PDMS), an organic elastomer. The PDMS chips were then mounted and bonded on SuperEpoxy SME glass slides from TeleChem International.

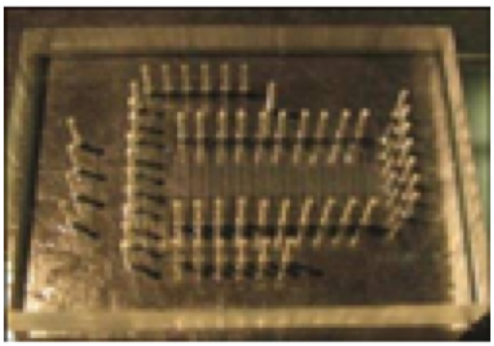

Figure 5.2 Elastomeric microfluidic immunoassay chip.

The immunoassays were carried out using human MMP-3, MMP-9 antigens, anti-MMP-9 polyclonal antibodies, and monoclonal human anti-MMP-9 and anti-MMP-3 antibodies manufactured by R&D Systems. Subsequent immunoassays were performed with human GalC and anti-GalC antibodies provided by a collaborator.

The MMP proteins were reconstituted with TCNB buffer solution containing 50 mM Tris buffer, 10 mM $CaCl_2$, 150 mM NaCl, and Brij 35 (a stabilizing detergent manufactured by VWR Scientific.) The reconstituted proteins were aliquot into single-use centrifuged tubes, and refrigerated at -27°C until needed. Furthermore, monoclonal human anti-MMP-9 and anti-MMP-3 were tagged with a Dylight 547 protein fluorescence labeling kit from the Pierce Corporation. The antibodies were stabilized with pure PBS buffer from Irvine Scientific.

The chip was controlled with a Fluidigm BOB3 pressure-flow controller and was interfaced to the user with the Fluidigm uChip software. Antigen and antibody solutions were gently vortexed before input. Tris buffer was used to passivate epoxide groups in reagent channels. Excitation of

the fluorophores was performed with a green light of 552 nm. Pictorial data was obtained using a Sony DFW-V500 Fire-i digital microscope camera.

Results and Discussion

We built a simple two-layer immunoassay, using a high-throughput microfluidic immunoassay chip designed by Kartalov et al [108], to illustrate a proof-of-concept of multiple sclerosis disease detection. A serum of MMP-9 was flowed through the coliseums of the fluidic chip and allowed to bond to the epoxide moieties on the glass bottom surface of the micro-channels in the flow layer (Figure 5.3).

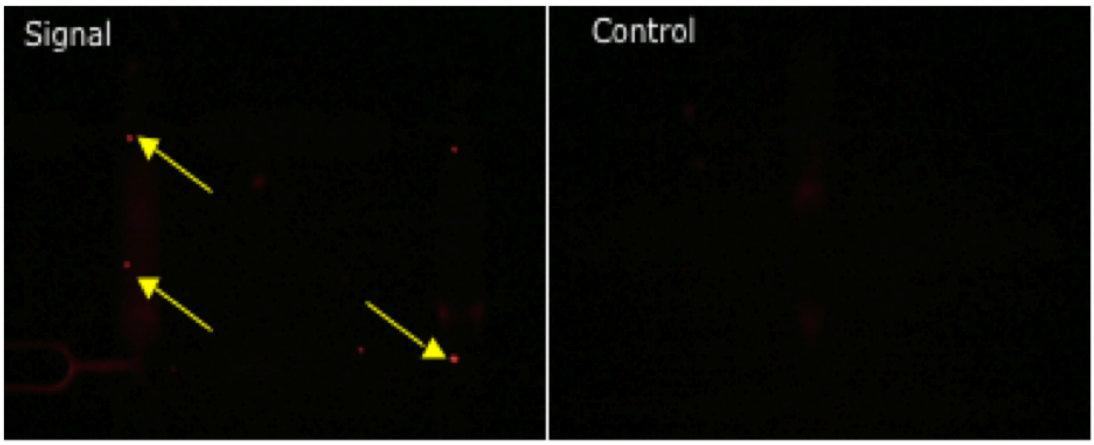

Figure 5.3 False-color fluorescence image of MMP-0 two-layer immunoassay

After passivating the remaining epoxide sites with TRIS buffer, fluorescently- tagged monoclonal anti-MMP-9 antibodies were pumped throughout the coliseums. Subsequently, the coliseums were flushed with TRIS buffer to liberate and remove any free- floating antibodies. Finally, the microfluidic chip was illuminated with light of wavelength 547 nm, and the fluorescence emission was captured by a CCD (Figure 5.3). We inferred the presence of MMP-9 from the observed fluorescence signal.

Controlled detection of MMP-9 was done using a sandwich immunoassay (Figure 5.4) for MMP-9. First, polyclonal goat anti-human MMP-9 molecules were flowed through the coliseums and allowed to bond to the epoxide layer of the immunoassay chip. After passivating the remaining epoxide moieties with TRIS buffer, simulated patient serum (consisting of a 470 nM solution of

MMP-9) was flowed through the coliseums. The MMP-9 was captured by the polyclonal anti-MMP-9 antibodies. Finally, fluorescently tagged monoclonal anti-MMP-9 antibodies were flowed through to bind to the MMP-9. Fluorescence imaging confirmed the presence of MMP-9 (Figure 5.5). Furthermore, fluorescence was observed only in coliseums that had exposure to MMP-9, attesting to the specificity of the sandwich immunoassay.

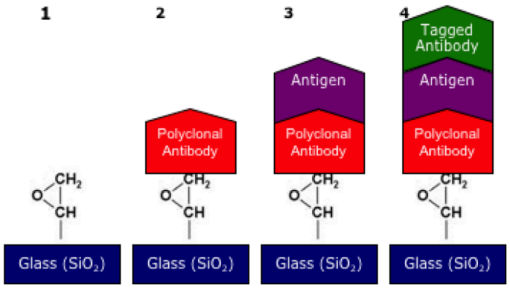

Figure 5.4 Sandwich immunoassay built onto epoxide substrate.

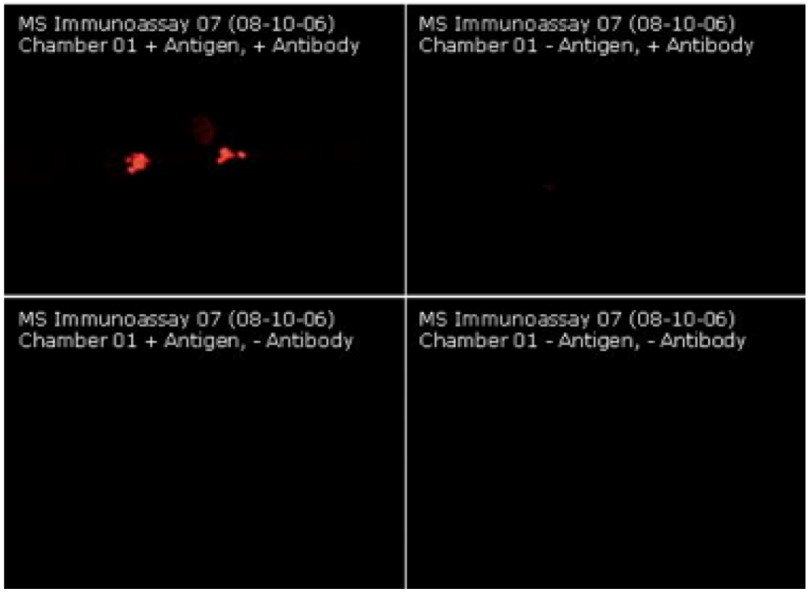

Figure 5.5 False-color fluorescence images of MMP-9 sandwich immunoassays

Since only fully formed sandwich immunoassays have fluorescently tagged antibodies, the intensity of the fluorescence emission corresponds to the strength of the signal. In one assay, we measured the red mean of the signal to be 227 with a standard deviation of 39.2. In comparison,

the red mean of the noise was 9.224 with a standard deviation of 9.23. This resulted in a SNR of 24 to 1. In another assay, we observed a red mean of the signal to be 72.6 with a noise floor of 7.01, resulting in a SNR of 10 to 1. Successful immunoassays consistently had signal to noise ratios of 10 to 1 or greater.

In future tests, we will attempt to do a more thorough characterization of the detection of antigens at ultra-low concentration. Additionally, we will attempt a three-stage characterization of multiple sclerosis through the detection of MMP9, myelin oligodendrocyte glycoprotein (MOG), GalC in the patient blood serum. Finally, we plan on integrating the microfluidic immunoassay chip with an elastomeric blood filter and CCD image capture device to illustrate the feasibility of a hand-held multiple sclerosis monitor.

Conclusions

We have demonstrated a proof-of-concept of multiple sclerosis disease detection through successful detection of the biomarker MMP-9. Furthermore, fluorescence detection of MMP-9 yielded SNR in excess of 24 to 1, with a minimum SNR of 10 to 1. Subsequent testing has suggested that MMP-9 antigen detection is possible with concentrations as low as 65 nM.

Chapter 6

IMMUNOAFFINITY CHROMATOGRAPHY IN ELASTOMERIC MICROFLUIDIC DEVICES

Summary

Immunoaffinity chromatography (IAC) is an important stage in sample-prep workflow in modern biotechnology. Herein we report on a microfluidic device that performs IAC. The demonstrated performance of the device is a proof-of-principle for microfluidic miniaturization of IAC, and thus is an important step towards integrated disposable devices performing DNA- and RNA-based diagnostics.

Introduction

Recent advances in microfluidic and microelectromechanical systems (MEMS) technology has allowed for the fabrication of miniaturized disease detectors. One mode of pathogen detection is through the use of miniaturized polymerase chain reactors (PCR) [109]. PCR is a quick and inexpensive process that allows for amplification of a given nucleotide sequence (Figure 6.1). DNA polymerase is utilized to copy a DNA template in successive cycles of amplification. The singular advantage of PCR is that is can be carried out exclusively in vitro.

A similar technique called real-time polymerase chain reaction (RT-PCR) allows for DNA quantification [111]. In RT-PCR, the fluorescence of an intercalating dye is measured after each thermal cycle. Dyes such as SYBR green bind to all double-stranded DNA in the PCR reaction.

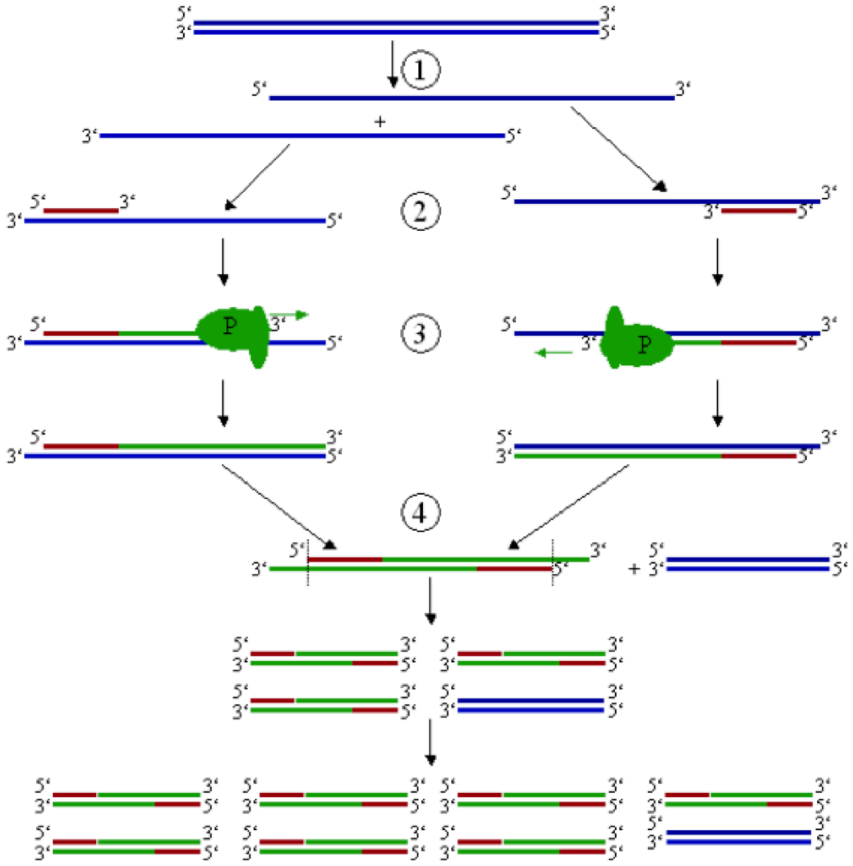

Figure 6.1 Generic scheme of polymerase chain reaction [110].

The relative number of DNA copies in a sample can then be interpolated by comparison to standard DNA dilution curves (Figure 6.2).

The speed and accuracy of RT-PCR makes it attractive for point-of-care diagnostics. However, to increase PCR amplification yield, it is necessary to start with a concentrated DNA serum. This can be accomplished by taking advantage of the lock-and-key interactions of antibodies and antigens [112-115]. In a process called IAC, biological mixtures are separated and concentrated. Using IAC methods, it is possible to sift through an environment sample to find a molecule of interest. This is applicable to the purification and concentration of various virus strains in a given sample serum.

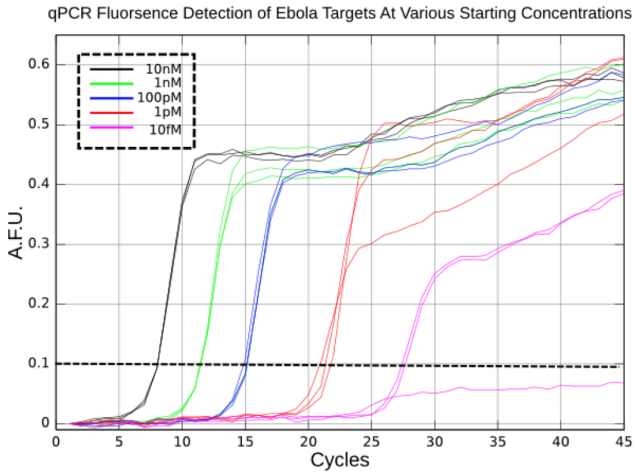

Figure 6.2 RT-PCR amplification curves for various concentrations of sample DNA (example).

Microfluidics provides a suitable platform for IAC since it allows for manipulation of minute quantities of fluids. By replicating column affinity chromatography (Figure 6.3) in a microfluidic chip, the quantities of reagents and samples used can be minimized. This results in a significant cost and time reduction for the immunoassay. Here, we present a proof-of-concept microfluidic immunoaffinity chromatography device that can be eventually used in conjunction with Parylene-based RT-PCR reactor. Eventually, this conglomerate system will form the basis of a hand-held detector for SARS.

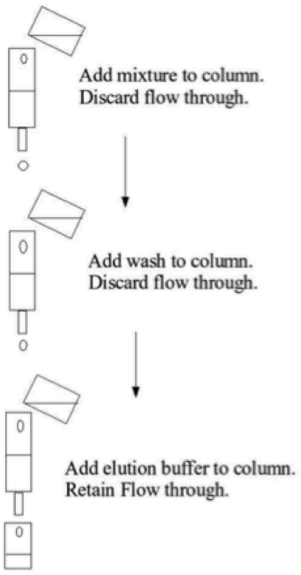

Figure 6.3 Column-based immunoaffinity chromatography [6].

Materials and Methods

The fluidic chip was first designed on a computer using SolidWorks, a three-dimensional modeling tool. This model was then used to produce an aluminum replica mold for the chip. Sylgard Dow-Corning 184 Elastomer—generic name, polydimethylsiloxane (PDMS)—was used to fabricate the fluidic chip. A Keyence Hybrid Mixer HM501 was used to prepare the elastomer in a 10:1 ratio of base to curing agent. A layer of PDMS was poured over the aluminum replica mold, degassed in a vacuum chamber, and thermally cured at 70°C for 60 minutes. Afterwards, the chip was cropped and cleaned with dilute 2-propanol.

Two through-holes were made for the input and output ports using a modified drill press. A 23 gauge aluminum cut tube, Type 304 manufactured by New England Small Tube, of external diameter about 647 micron was inserted into the inlet and into the exhaust. The affinity chromatography chip was then mounted on a sterile glass slide, and clamped with binder clips (Figure 6.4). The clamps and cut tubes were bonded to the surface of the PDMS using epoxy. The inlet and exhaust tubes were fitted with Tygon Microbore tubing manufactured by Cole-Parmer. The input port of the chip was then mated to a 1cc syringe using a 23-gauge lure stub adapter. Reagent flow was driven using a programmed Pico Plus 11 syringe pump manufactured by Harvard Apparatus.

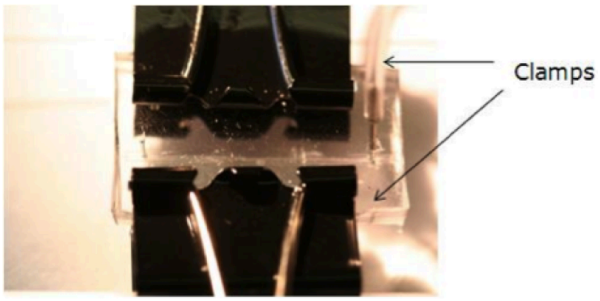

Figure 6.4 IAC chip clamped with binder clips.

The immunoaffinity chromatography was modeled on the procedure of the Seize Primary Immunoprecipitation Kit (Catalog Number 45335) manufactured by the PIERCE Corporation. Off-chip validation of the RT-PCR was also performed using this commercially available affinity chromatography kit. The agarose-sepharose beads provided in the kit were functionalized and bonded with antibodies specific to the M13 virus. During the on-chip chromatography, the beads were packed into the inlet channel. Reagents including the M13 virus serum,

immunoprecipitation buffer, and elution buffers were flowed through the channel at rates not exceeding 11 μL/min, and virus capture and elution took place throughout the inlet channel. After the chromatography was performed, the samples were analyzed using a Stratagene MX3500P RT-PCR machine. Further analysis was performed using a Fuji laser-based gel electrophoresis imager.

Results and Discussion

The primary device investigated was a simple fluidic filter fabricated in PDMS. This fluidic device consists of a 50-micron wide filter section sandwiched between two 650 micron wide inlet and exhaust channels (Figure 6.5). The dimension of the filter section was chosen in order to obfuscate the flow-though of immunoaffinity beads on which the chromatography occurs. A simple statistical analysis of bead sizes showed that mean and median bead size was approximately 80 micron. The device has a 2:1 height to width ratio, which was necessary to prevent the walls of channel from collapsing. The PDMS chip was bonded and clamped to a glass slide. The input port was mated to a syringe pump to drive reagent flow, while the exhaust port was attached to a centrifuge tube to collect the flow through.

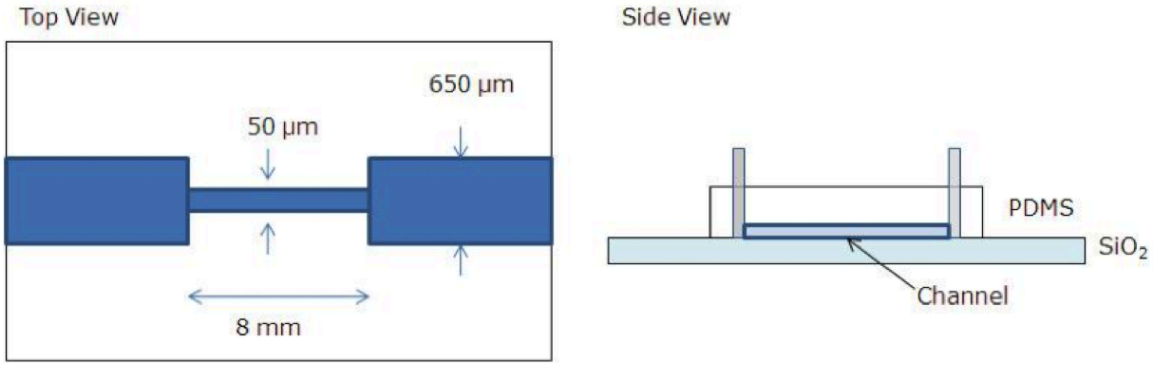

Figure 6.5 Top and side views of IAC fluidic chip layout

A M13 bacteriophage virus was used to test the biology and chemistry of the chromatography device. First, M13 antibodies were bonded to agarose-sepharose beads. These beads were then flowed and sequestered in the inlet channel of the device. A simulated sample serum of M13 was flowed through the channel. The M13 antibodies captured the virus of interest though highly selective antibody-antigen interactions. After purging the system of any residual virus by flowing

through immunoprecipitation buffer, the captured virus was liberated from the bead matrix by flowing elution buffers.

All the flow-throughs were saved and analyzed using a commercial off-chip RT-PCR device. A gel-electrophoresis was run to confirm that the fluorescence was indeed from the product of interest, and not from spurious DNA (like primer-dimers). By comparing the fluorescence of the samples with the fluorescence of several standard M13 concentrations, the relative quantity of eluted M13 virus was determined (Figure 6.6). The elution (Elution 1, Figure 6.6) on-chip IAC procedure was able to provide a -100x concentration of the sample M13 serum (M13 F.T., Figure 6.6). Though the on-chip IAC ended up diluting the virus serum, it did perform an order of magnitude better than an off-chip IAC procedure using a commercially available kit.

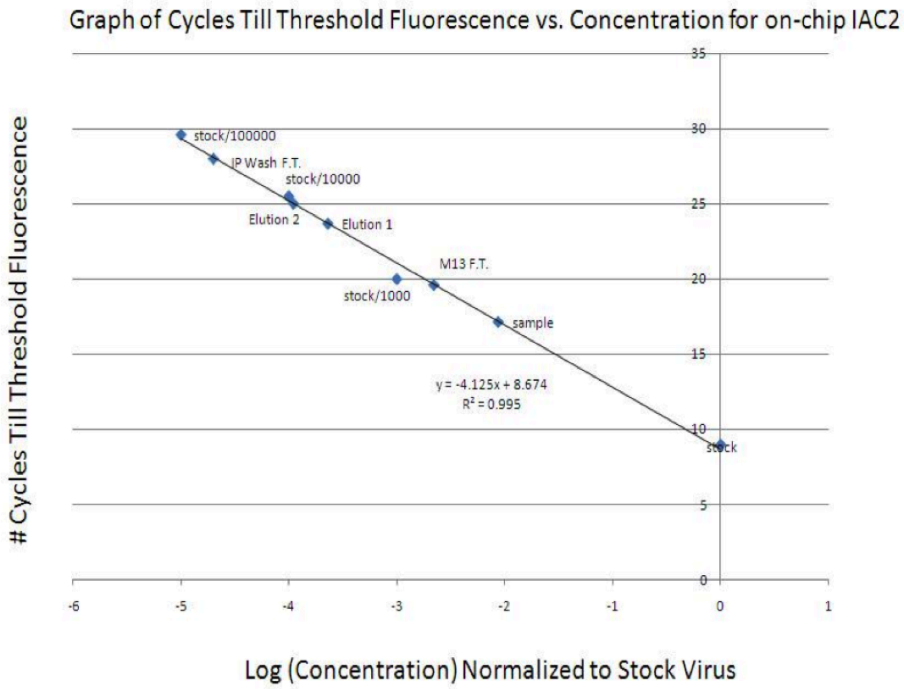

Figure 6.6 Graphs of cycles till threshold fluorescence vs. concentration for on-chip IAC02.

Using the fluorescence data from the standard curve, it was determined that approximately 2000 viruses were eluted. This corresponded almost exactly to the estimated number of antibody bonding sites in the channel of the IAC chip. The insufficient number of bonding sites may explain why the IAC device was only able to achieve negative concentrations. (In the future, it may be necessary to redesign the inlet channel in order to accommodate more agarose beads—thereby providing a larger number of binding sites.) Furthermore, a gel electrophoresis of the

flow-throughs confirmed that the correct M13 genome was amplified. Finally, two control chromatography experiments were performed: an IAC with beads with no antibodies attached, and an IAC with no beads at all. There was an absence of virus in the elutions of both these controls. This confirmed that immunoaffinity chromatography had indeed taken place in our original experiment.

In the future, we plan to investigate a higher-throughput fluidic chip that will allow for faster affinity chromatography. This device will employ multiple filter sections in a completely embedded channel in PDMS (Figure 6.7). Reducing the fluidic resistance of the filter and providing a larger surface area for virus capture will allow the device to concentrate the sample quicker. Furthermore, we also plan on devising methods to pack beads more tightly in the inlet channels of the first generation of chromatography chips—by increasing bead input flow rates, or by widening the inlet through-holes—in order to provide more binding sites for the M13 virus.

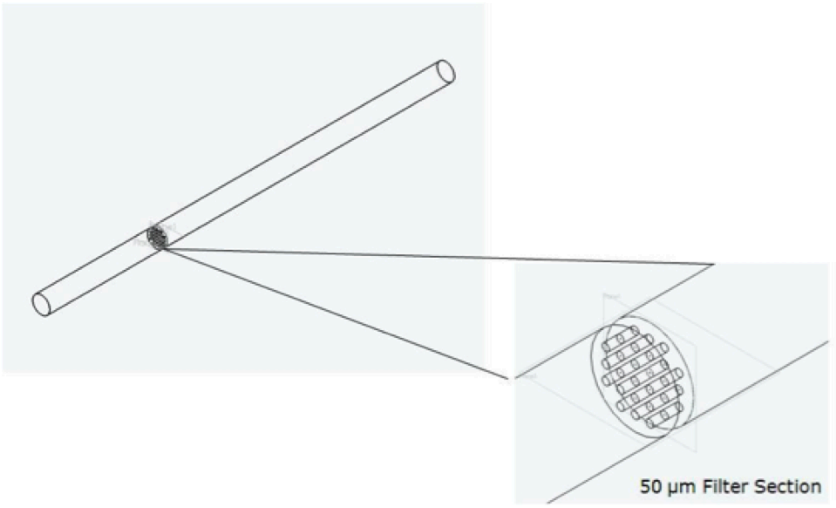

Figure 6.7 High-throughput fluidic channel.

Finally, we plan on optimizing the RT-PCR process in order to get data to better quantify the performance of our chromatography technology.

Conclusion

Immunoaffinity devices will become increasingly important in coming years, as they provide the possibility of portable pathogen detection. Specifically, microfluidic quantitative real-time polymerase chain reactors (RT-PCR) show promise as hand-held detectors for a spectrum of

diseases including SARS coronavirus, the virus responsible for the severe acute respiratory syndrome (SARS). Our device provides a proof-of-concept for integrated on-chip IAC that can be used in conjunction with such a detector.

Chapter 7

MICROFLUIDIC EVAPORATIVE COOLING

Summary

Localized evaporative cooling in fluidic channels provides an elegant and low-cost solution to the problem of cooling electronics, optics and chemical reactions. By optimizing the geometry of a Y-junction and the gas/evaporant ratios, we found that the optimal refrigeration took place in a 10 degree Y-junction when using ethyl ether as the evaporant. Maximum temperature drops were measured when gas inlet pressures were between 21 psi and 36 psi. The evaporation of ethyl ether also enabled temperatures as low as -20°C to be sustained for several minutes. These findings prove principle for evaporative cooling in microfluidic systems.

Introduction

Miniaturization of components has been the defining trend in the world of electronics and optics for the past 50 years. Moore's law predicts a doubling of transistors density in approximately every 18 months [115], and transistor resolution is now well below 100nm [116]. With this rapid increase in transistor density, the fundamental problem of heat dissipation places ultimate limitations on processing power and device speed. Attention to energy consumption and heat dissipation is of paramount importance [117] when designing new electronic and optical architectures. So far, heat dissipation has been addressed in a variety of ways, from "sleep" transistors [118] to on-chip micro-refrigeration [119].

Besides electronics, there are many fields in need for miniaturized refridgeration: optical and microwave detector cooling, polymerase chain reactor cycling, and thermal stabilization of high power telecommunications lasers. Temperature control has also become very important in ensuring the precise control of thermally sensitive reactions within the framework of microfabricated chemical "laboratories" in which sub-nanoliter volumes of reagents are reacted on microfluidic chips.

Herein we present a unique solution to the problem of heat dissipation: localized cooling through evaporation of volatile materials within microfluidic channels. It is well known that refrigeration

can be achieved through the endothermic mixing of compressed gas with an evaporating liquid [120]. Herein we demonstrate that evaporative cooling works in microfluidic devices as well.

Materials and Methods

The fluidic channels were first designed on a computer using SolidWorks, a three-dimensional modeling tool. These models were then converted to a usable file format using SolidScape's ModelWorks software. Wax molds of the fluidic channels were created using a SolidScape T66 wax printer. The wax molds were then chemically cured (to remove unwanted build wax) with Petroferm Bioact VS-0 Precision Cleaner, and thermally cured by overnight heating at 37°C.

Sylgard Dow-Corning 184 Polydimethalsiloxane (PDMS) elastomer and curing agent were mixed in a 10:1 ratio using a Keyence Hybrid Mixer HM501 to fabricate the fluidic channels. The PDMS was then cured in a three-step process. First, a 0.3 mm thick initial layer of elastomer was degassed in a vacuum chamber for 10 minutes and thermally cured at 80°C for 8 minutes. Next, a second, thin layer of uncured PDMS was poured on top of the first layer. The wax junction-mold was then placed on the second layer of PDMS. Finally, a 3 mm thick layer of PDMS was poured on top of the wax mold. The setup was finally pumped down in a vacuum chamber for 25 minutes to degas the elastomer and then heated at 54°C for 4 hours to thermally cure the PDMS.

The PDMS blocks were then cropped and de-waxed (by heating to 90°C for 15 min). Acetone was rinsed through the fluidic channels to remove residual build wax. The fluidic chips were then attached to a refrigerant and N_2 gas inlets. An Omega Precision fine wire, K-type thermocouple was inserted into the outlet of the fluidic channel. The thermocouple had a diameter of 0.125 mm—small enough not to interfere with the outlet of refrigerant and gas. The thermocouple was attached to an Omega iSeries i/32 temperature controller that logged the temperature in the junction at a rate of approximately 3 Hz. Temperature measurements were made using this controller interfaced to a computer via serial port and Microsoft HyperTerminal. The inlet pressures of the refrigerant and the gas were monitored using TIF Instruments digital pressure meters.

Results and Discussion

A simple Y-junction was fabricated with two input channels (Figure 7.1)—one for the refrigerant

and the other for the gas. Evaporation occurs throughout the outlet channel. In our experiments, each channel has a length of 6.5 mm and a diameter of 0.650 mm. The angle of the Y-junction was varied between 10 degrees and 180 degrees, and the cooling effect was characterized as a function of angle, inlet gas pressure (N_2) and type of refrigerant. We successfully characterized such evaporative cooling using ethyl ether, acetone, ethyl alcohol and isopropyl alcohol.

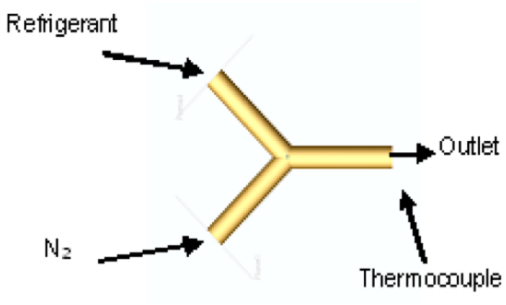

Figure 7.1 Y-Junction cooler geometry.

Preliminary characterization of the channels indicated that the lowest refrigeration temperatures were achieved by evaporating ethyl ether. We believed that this was due to the very low specific heat and boiling point of ethyl ether—enabling rapid vaporization. Ethyl ether pressure was 1.2 psi, while the N_2 inlet pressures were in excess of 20 psi. Refrigeration rates recorded for the vaporization of ethyl ether were approximately 40°C/s. The evaporation of ethyl ether also enabled temperatures as low as -20°C to be sustained for several minutes (Figure 7.2). Prolonged cooling effects in excess of 15 minutes were also recorded.

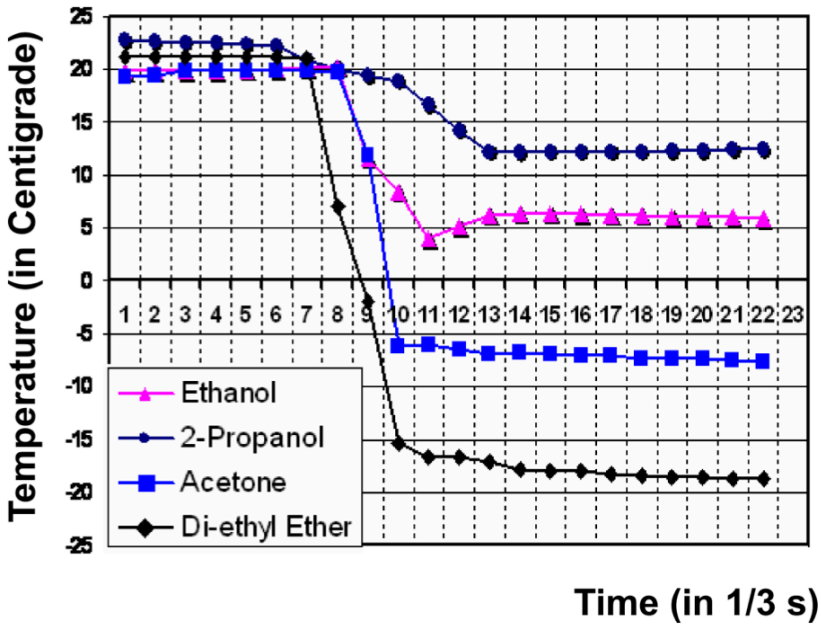

Figure 7.2 Temperature drop versus time for four refrigerants. The gas inlet pressure for the isopropyl alcohol, ethyl alcohol, and acetone graphs was 20psi. The gas inlet pressure for the ethyl ether experiment was 21psi.

The rates of temperature decrease in the mixing channel were also characterized with respect to the gas inlet pressures. We incremented gas inlet pressures from 0 psi to 36 psi in steps of 3 psi, and found that there was a positive relationship between the gas inlet pressure and the refrigeration rate. However, we noted that inlet pressures in excess of 21 psi did not significantly increase the cooling effect further (Figure 7.3). We suspected that such increases in the gas inlet pressure created back-pressure within the inlet channels, and a corresponding disruption in the flow of the refrigerant.

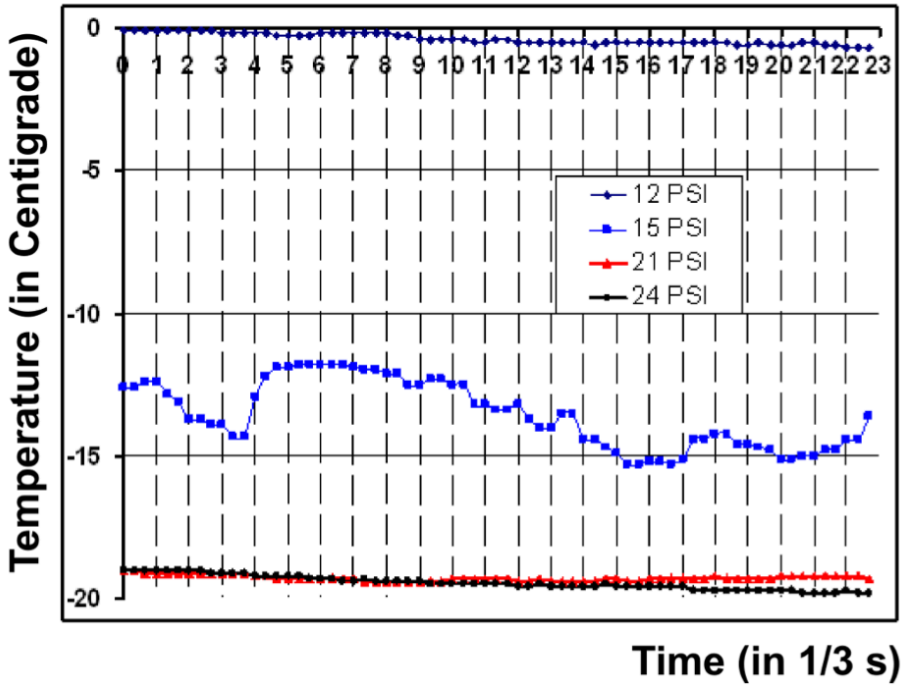

Figure 7.3 Graph of minimal attainable temperature versus time for two channels impinging at 10 degrees. Legend indicates inlet gas pressures in psi.

We also characterized Y-junction geometries with respect to angle between the channels. We found that the slowest refrigeration occurs when the angle between the channels forming the Y-branch is large (180 degrees), and the refrigerant supply and nitrogen evaporation gas sources point at each other. Conversely, the most efficient cooling was measured when the angle between these two supply channels was 10 degree Y-junction. We think this was due to the fact that in smaller angles, flow congestion at the junction can be minimized. Smaller angles allow the vaporized refrigerant and heat to leave the system faster. Furthermore, larger angles exhibit significant back-pressure problems at pressures in excess of 15 psi (Figure 7.4). Back-pressure prevents proper refrigerant flow, thereby dampening the cooling effect. This was most clearly demonstrated in a test for the 180 degree junction with gas inlet at 25 psi and ethyl ether inlet at 1.2 psi, where little or no cooling was observed.

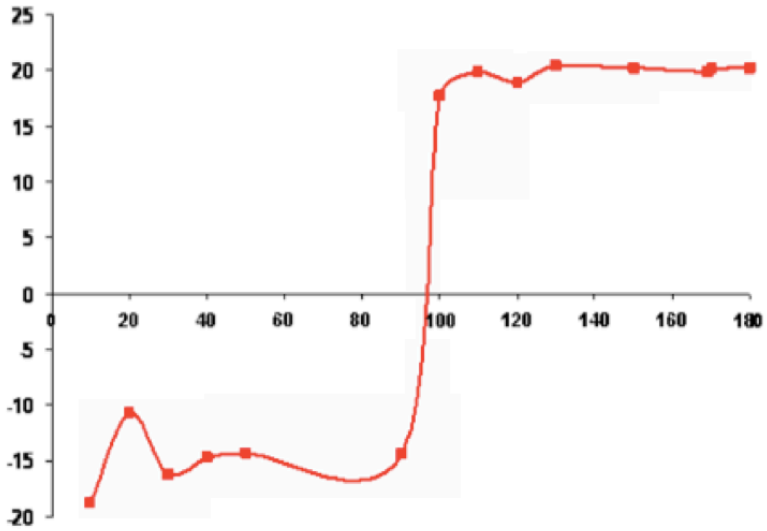

Figure 7.4 Minimum attainable temperature (Centigrade, vertical axis) drop versus time with respect to junction angle of channel (degrees, horizontal axis). The gas inlet pressure for the 10 degree channel was 21psi. For all other channels, the gas inlet pressure was 20psi.

We also investigated the increase of the size of the outlet channel in hopes of promoting the expansion associated with evaporation of the refrigerant. However, we found that widening the outlet channel to a diameter of 2 mm did not result in faster refrigeration.

A copper heat sink was also embedded into a fluidic chip. In this chip, it was observed that the cooling effect in the Y-junction channel resulted in a cooling effect in a second channel. The copper heat sink acted as a thermal bridge between the two channels. With this model, it was possible to demonstrate the cooling of an external heat source. This experiment confirmed that it is possible to apply the evaporative coolers for electronic and optical cooling purposes. Ultimately, we hope to develop self-sustaining, closed systems in which the refrigerant is conserved. One possibility for refrigerant conservation would employ a selective, organic membrane at the output channel. Furthermore, in order to provide an applicable solution for the cooling of electronics, we plan on integrating microfluidic cooling systems into silicon.

Conclusions

Localized evaporative cooling in fluidic channels provides an elegant and low-cost solution to the problem of cooling electronics, optics and chemical reactions. By optimizing the geometry of a

Y-junction and the gas/evaporant ratios [120], we found that the optimal refrigeration took place in a 10 degree Y-junction when using ethyl ether as the evaporant. Maximum temperature drops were measured when gas inlet pressures were between 21 psi and 36 psi. The evaporation of ethyl ether also enabled temperatures as low as -20°C to be sustained for several minutes. These findings prove principle for evaporative cooling in microfluidic systems.

Chapter 8

CONCLUSIONS AND NEW DIRECTIONS

The content of this thesis is divided into two broad categories: microfluidic devices for biological measurement and biological techniques. The microfluidic tools described in this thesis each perform a specific task (e.g. concentrating nucleic acids or performing a polymerase chain reaction). However, these devices can be combined and cascaded in various combinations to perform a variety of tasks in a miniaturized laboratory footprint. As such, these individual devices are akin to tools in a microfluidic tool kit. We will briefly describe some of the ways these simple tools can be combined to make more complex instrumentation.

We will also describe some of the applications and extensions of the supercolor coding methods described in the thesis. These coding methods can be used in real-world scenarios, and we will show the performance of such assays in a clinical laboratory setting. Furthermore, we will describe new directions for nucleic acid probe designs that might bridge the information density gap between PCR and sequencing.

Modular Fluidics

Modular microfluidic components have been speculated before [121-123], though these components are often integrated on a single microfluidic substrate [124]. This diminishes the utility of microfluidic breadboarding, however, forcing integration to take place pre-fabrication rather than post-fabrication. Yet, post-fabrication breadboarding can be realized if the PDMS-PDMS interconnects are properly gasketed to pressure gradients and to limit fluidic losses [125-127].

The various sensors and devices described in this thesis can be connected and daisy-chained to form more complex, integrated microfluidic systems. For example, the immunoaffinity chromatography chip can be mated upstream of the PCB-based PCR device to create the foundation for a sample-to-answer PCR instrument. Since all the microfluidic devices described in the body of thesis have been designed to be coupled, a variety of more complex micro-laboratories can be easily engineered by mixing and matching components.

For instance, the platinum heating elements can be coupled with the evaporative coolers to form a miniature temperature management system to control chemical reaction rates. This system might be used as substrate for nucleic acid amplification, or a substrate for the careful generation of particular chemical products. Future work will incorporate the heaters, coolers, and DNA extraction devices to form the basis for might ultimately be a low-cost, portable disease diagnostic.

Applications of Multiplexing PCR in Real-World Scenarios

In this thesis, we described super-color coding methods for the polymerase chain reaction using synthetic nucleic acid targets. One practical application of this technique is the detection of infectious diseases in clinical samples. In order to demonstrate the efficacy of the super-color coding technique in clinical samples, we designed a single color, seven-target PCR assay for respiratory illnesses. This panel was designed to look at targets for strains of Influenza (InfA and InfB), Respiratory Syncytial Virus (RsvA and RsvB), Human metapneumo virus (Hmpv), Human rhino virus (Hrv), parainfluenza (PIV-3); these sequences are listed in Appendix B Tables 1-7.

This assay was multiplexed using the binary coding technique described in chapter four. Thus, the reporters for InfA, InfB, RsvA, etc. were coded with a 1x, 2x, 4x, etc. intensity. Clinical aspirate samples from patients in the Dartmouth Hitchcock Medical Center were spiked with synthetic targets corresponding to 100 nM concentrations of Influenza A, Influenza B, and Respiratory Syncytial Virus. The blinded, spiked clinical aspirate samples from hospital patients were processed using standard hospital sample preparatory protocols to extract nucleic acids. The resulting sample serum, containing a possible combination of InfA, InfB, and RsvA, was processed in a PCR detection protocol using the seven-target assay. We found that the multiplex coding technique was able to successfully distinguish arbitrary combinations of the infectious diseases in superposition (results are tabulated in Figure 8.1).

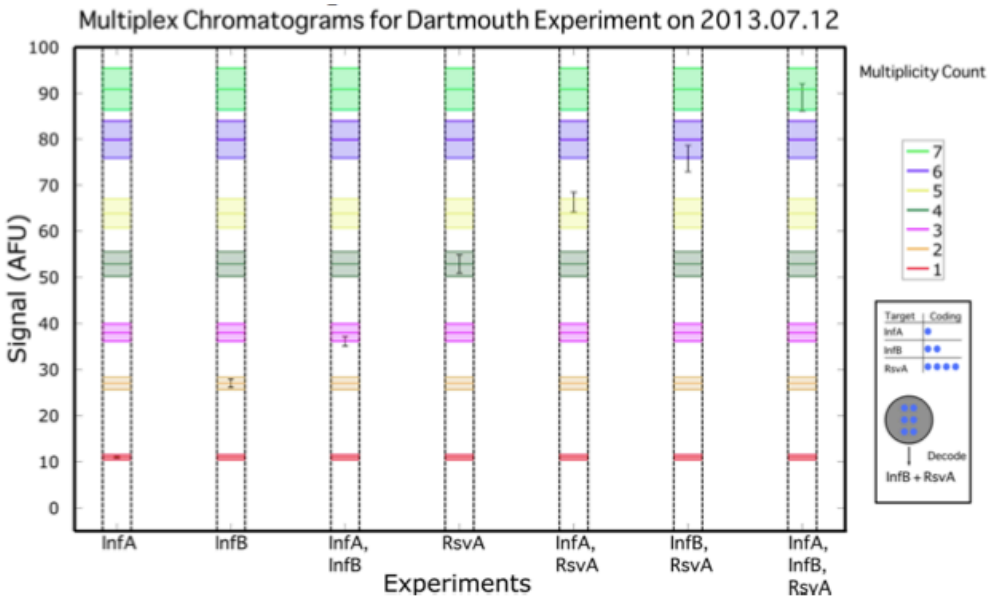

Figure 8.1 Chromatogram for intensity-coded multiplexed PCR in clinical samples spiked with respiratory viruses. The bands represent the multiplexed counts, and the bar and stem data points represent the data points with measurement uncertainty.

We also applied the binary coding technique to a set of single-plex PCR assays for regulatory genes GusB, B2M, and GapDh. The primer and probe sets were titrated in a 1x, 2x, and 4x fashion, respectively, to generate a single-color, triplex panel. This panel was tested on human genomic samples containing combinations of the three genes at a CLIA laboratory facility in Irvine, CA (ResearchDx). We again demonstrated that the supercolor coding technique was able to correctly identify the various combinations of the targets (see Figure 8.2).

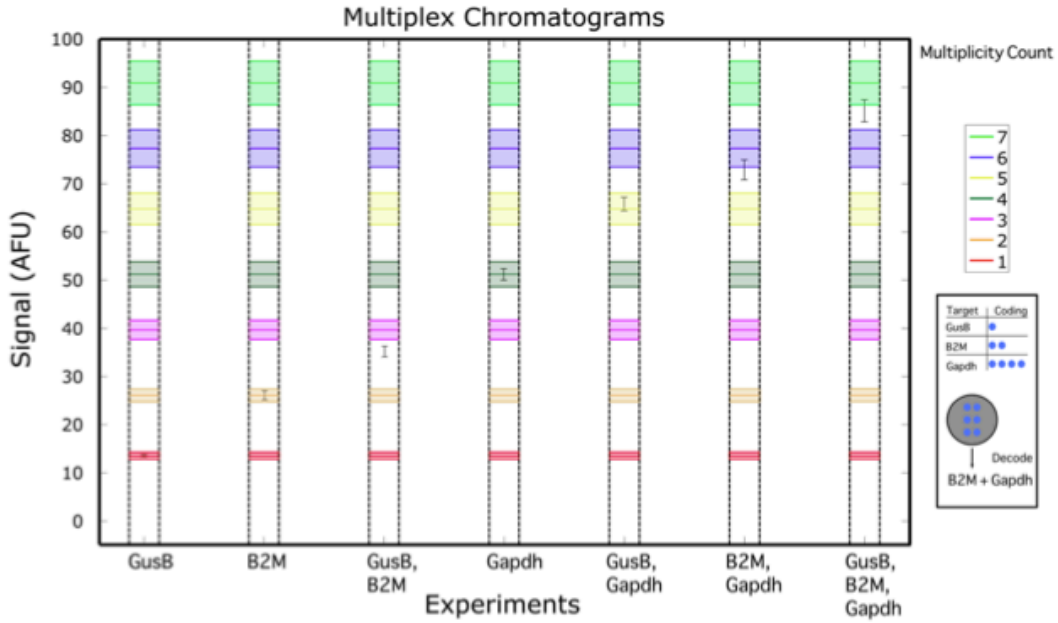

Figure 8.2 Chromatogram for intensity-coded multiplexed PCR in human genomic samples. The bands represent the multiplex counts, and the bar and stem data points represent the data points with measurement uncertainty.

These results suggest that the supercolor coding techniques can be used in real-world scenarios to identify and eventually quantify, nucleic acid targets in various combinations. We aim to collect data and explore the use of this technique in a variety of clinical samples in the near future. This will likely pave the way for the use of midplex PCR (6 - 40 targets per reaction) for clinical diagnosis of disease as well as the identification of particular genomic markers. While this does not approach the information-rich data sets generated by whole genome sequencing, it does significantly improve the data density of the more widely-used PCR.

Codes in DNA

Another application of supercolor PCR multiplexing is for the encryption and decryption of digital codes into nucleic acids. Cryptographic techniques are used for the encoding and decoding of information that needs to be hidden from all possible recipients except for the intended target. However, efficient codes must strike a balance between complexity of coding and density of information. Furthermore, the interpretation of these codes should be done in a way that a reader (intended recipient) can decode the information in an unambiguous fashion. Elegant codes can achieve this with one-to-one mapping of information to cryptogram. For instance, a one-to-one mapping a message in English would require 26 different coded characters. Effectively, this

requires a base-26 code for the mapping.

However, there is a less complex, but less spatially compact way of replicating this type of code. Binary values of a predetermined length can be used to code for letters and symbols. For instance, the English language ASIC lookup table maps a hexadecimal (effectively binary) code to every character of the language. This allows for the coding of letters in a fashion that can be understood by machines.

For instance, consider the set of n-unique organisms (such as bacteriophages, bacteria, or other viruses), where each organism represents a "bit" of the message. If we consider a set of n=20, and if organisms 1, 3, 6, and 19 are present, the code would be read as: 01000 00000 00001 00101 (Table 8.1).

Table 8.1 Examples of organism-based coding for a 20-bit protocol.

Organisms Present	Interpretation
1,2,3	00000 00000 00000 00111
1,2,5	00000 00000 00000 10011
2,6,12	00000 00010 00001 00010
1,3,6,19	01000 00000 00001 00101

In order to decode the message, the recipient would only need to run a multiplexed PCR reaction containing the message contents, which allows for a fast decoding of the message contents. Since the state-of-the-art in PCR allows for the simultaneous measurement of 4 - 6 targets, supercolor-coded PCR is an ideal candidate to implement this coding technique. We are currently exploring the feasibility of these encryption techniques in the coming months.

Transportation of the Message

Furthermore, several techniques could be used for the transportation of the message contents. Nucleic acid cryptograms can be easily transported in a variety of organic desiccants that preserve the bond structures while preventing contamination from external environment. One such embodiment is the inclusion of nucleic acid cryptograms in saccharide-based desiccant. For instance, the cryptograms can be preserved inside of sucrose packages for transportation. In addition to preserving the codes, the delivery method allows for easy destruction of the message

if the need should arise. The message contents can be easily and safely digested by human and animal consumption. Furthermore, the message contents can be obfuscated, destroyed, and disposed of by dissolving the saccharide package in a solution including but not limited to saliva, water, urine, soda, ethanol, and alcoholic beverages. This package form factor is particularly advantageous, since it is very similar to hard candy. This allows for the package to be physically transported from the creator to the intended recipient without arousing suspicion.

When the message contents need to be read, the saccharide package would be dissolved in a known solution that is conduce to nucleic acid stability. An electric field can be applied to extract and concentrate the nucleic acid cryptogram. Simple sequencing can be used to determine the content of the message.

Providing a natural environment for each "bit" of the message would likely preserve the contents for an appreciable amount of time. For instance, in an n-bit code each organism can be stored in a host such as a small rodent or mammal. In order to decode the message, the recipient would only need to draw the blood of the animal and run a PCR reaction. The message host provides the ideal conditions to preserve the message, while having the added benefit of degrading the contents of the message for prolonged time scales (i.e. the host will die due to infection). In fact, the SNP sequences from the host can be used to authenticate the information that is encrypted.

Alternatively, hosts can be intentionally tagged with benign organisms for identification purposes. For instance, a predetermined set of non-lethal bacteria or viruses can be used to infect a human host. When the human host is required to provide authentication of their identity, a drop of blood can be extracted from them. The PCR analysis run on the blood would confirm their identity. Because of the specificity of the PCR reaction, only the intended authenticator would know how to interpret the nucleic acid contents of the blood sample. Furthermore, this has the additional benefit of obfuscating the contents of the message (i.e. blood sample), since the blood will contain native host DNA as well as the DNA of any parasitic and symbiotic organisms.

In another variation, organisms can be used to transfect the host with particular nucleic acid targets. These targets would code for unique proteins that would be expressed in the blood. In order to read the message contents, the blood contents would only need to be processed in an immunoassay such as an ELISA. The specificity of the antibody-protein bond would allow the message to be uniquely interpreted.

Extension to Sequencing

Eventually, these coding techniques can also be realized using DNA sequencing, instead of PCR. For example, consider a scheme wherein the A-T 2mers code for the digit 0 and A-A and T-T 2mers code for the digit 1. In this case, a reading of either A-T or T-A is interpreted as a 0, while the reading of either A-A or T-T is interpreted as a 1. Since DNA is readily stabilized by its complementary strand, this allows for a natural redundancy in the message contents. In this coding scheme, the reading frame is determined by the binary spacing of the intervening G's and C's. For instance, consider the sequence following sequence:

5'**AT**GGGGGGGG**AT**GGGG**AT**GG**AT**G3' 3'**TA**CCCCCCCC**TA**CCCC**TA**CC**TA**C5'

Here, the message is read starting at the 5' end of the bottom strand. This is due to the fact that the G-C spacing increases as the frame shifts downstream (to the 3' end). The coding base pairs (A's and T's) can be tagged with variety of reporters including but not limited to heavy metal ionic tags, fluorescent markers, quantum dots, quenchers, hydronium (ph-based) markers, and radioactive tags. The message contents are read by sequencing the entire DNA strand. The spacing between the reporters allows the reader to determine the location of the message he is reading, while the tags themselves denote how the content is to be interpreted.

Novel Nucleic Acid Probes

Our investigations into multiplexed PCR sequed into a survey of the different part of nucleic acid reporters. Nucleic acid targets are discriminated using one of several techniques including fluorescence intensity measurement (using TaqMan probes, FRET probes, or intercalating dyes), length discrimination (using gel electrophoresis, melt curve analysis, etc), or chromatography (haptin-based nucleic acid capture, etc.). Whereas, we described PCR combinatorial coding with using traditional probe chemistries, these codes are extensible to novel probes as well.

For example, individual PCR primers can be ligated with chromaphores. Consider a scheme wherein the chromaphore on one primer is a fluorophore and the chromaphore on its complementary primer is a matched quencher. As a PCR reaction, specific to these two primers, proceeds to completion, the observed fluorescence will decrease. This is because a correctly amplified PCR product will bring the two chromaphores into close proximity (since they are fixed

onto a the DNA polymer), reducing the fluorescence signal. For instance, consider the sequence:

5’ATGGGGGGGGGGGGGGGGATGGGGGGGGAAGGGGGGATGGGGGGGGATGGGGATGGATG3’
3’TACCCCCCCCCCCCCCCCTACCCCCCCCTTCCCCCCTACCCCCCCCTACCCCTACCTAC5’

We can design the forward (FWD) and rewind (RWD) primers such that a quencher and fluorophore are ligated to the 5’ of each primer respectively:

FWD Primer /Quencher/5’ATGGGGGGGGGGGGGGGGAT3’
RWD Primer 3’CCCCCCCTACCCCTACCTAC5’/Fluorphore/

If the primers are selected in appropriate concentrations to limit unbound quenching, before the first cycle of PCR reaction is run, there will be a total intensity of *X*. During the first cycle of the PCR, this intensity level will be unchanged, as there will be no DNA target present that incorporated both a fluorophore and a quencher. As the cycles progress, on average, the total fluorescent signal will decrease by a factor of 2 per cycle. Therefore, the fluorescent intensity at the end of cycle two will be *X/2*. This is due to the fact that the persistence length of DNA target is such that the fluorophore on the anti-sense strand is efficiently quenched by the quencher on the sense strand. This attenuation of the fluorescent signal will continue till the supply of primers for that target have been exhausted. In this way, a “dark-field” measurement for the DNA target can be obtained by looking at the intensity of fluorescence after each cycle. Schematically, the PCR reaction will proceed as follows (Figure 8.3):

5’ATGGGGGGGGGGGGGGGGATGGGGGGGGAAGGGGGGATGGGGGGGGATGGGGATGGATG3’ Extension <- 3’CCCCCCCTACCCCTACCTAC5’/**F**/

3’TACCCCCCCCCCCCCCCCTACCCCCCCCTTCCCCCCTACCCCCCCCTACCCCTACCTAC5’
/**Q**/5’ATGGGGGGGGGGGGGGGGAT3’ -> Extension **Cycle One Annealing**

/**Q**/5’ATGGGGGGGGGGGGGGGGATGGGGGGGGAAGGGGGGATGGGGGGGGATGGGGATGGATG3’
Extension <- 3’CCCCCCCTACCCCTACCTAC5’/**F**/

3’TACCCCCCCCCCCCCCCCTACCCCCCCCTTCCCCCCTACCCCCCCCTACCCCTACCTAC5’/**F**/
/**Q**/5’ATGGGGGGGGGGGGGGGGAT3’ -> Extension **Cycle Two Annealing**

/**Q**/5’ATGGGGGGGGGGGGGGGGATGGGGGGGGAAGGGGGGATGGGGGGGGATGGGGATGGATG3’
3’TACCCCCCCCCCCCCCCCTACCCCCCCCTTCCCCCCTACCCCCCCCTACCCCTACCTAC5’/**F**/

/**Q**/5’ATGGGGGGGGGGGGGGGGATGGGGGGGGAAGGGGGGATGGGGGGGGATGGGGATGGATG3’
3’TACCCCCCCCCCCCCCCCTACCCCCCCCTTCCCCCCTACCCCCCCCTACCCCTACCTAC5’/**F**/

End of Cycle Two Extension

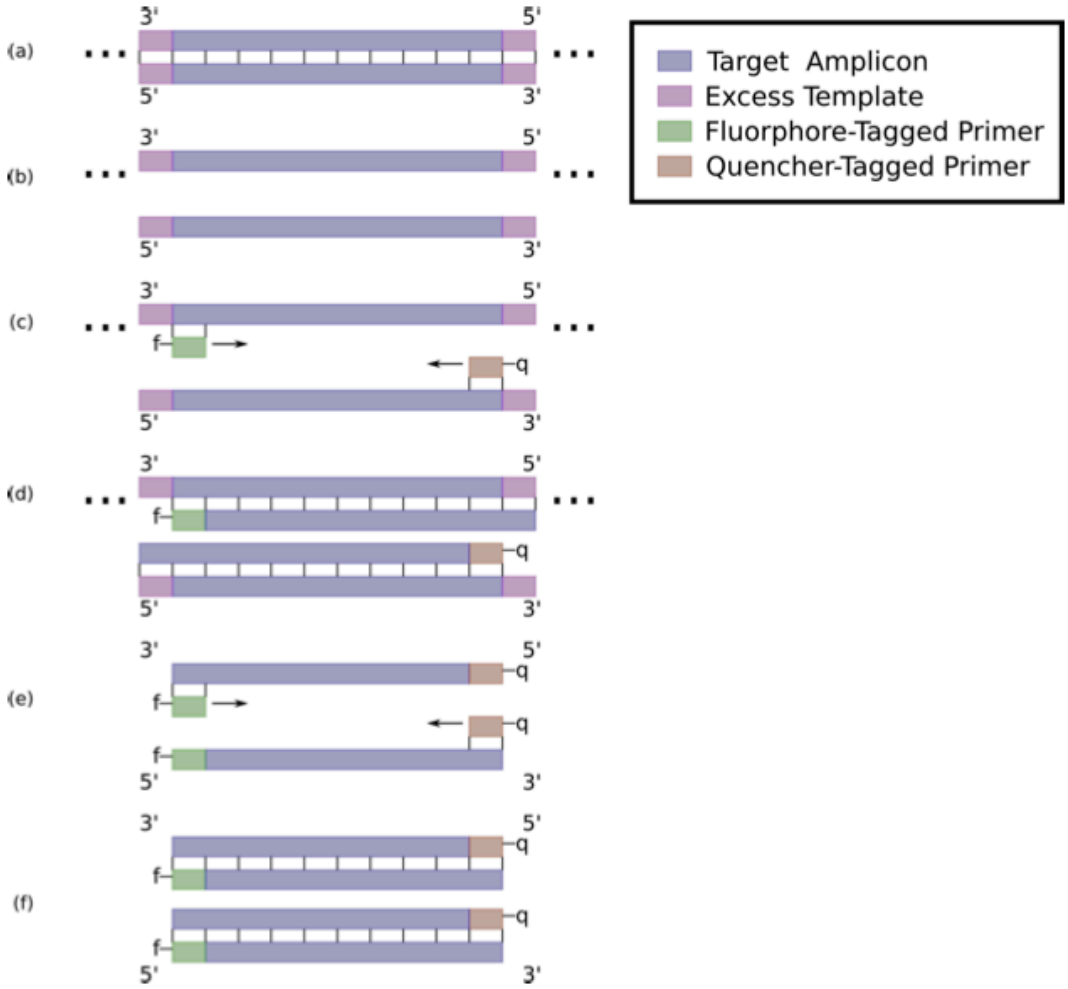

Figure 8.3 Chromaphore-tagged primers for DNA synthesis over subsequent cycles. As the polymerase chain reaction proceeds over consecutive cycles (c)-(g), the two chromaphores are brought into close proximity (f), reducing the overall fluorescent signature.

Furthermore, by carefully observing this PCR reaction at both the denaturation and the annealing stages (Figure 8.4), we can get a cycle-by-cycle normalization. This chopper stabilization is possible because the original (cycle zero) fluorescence signature is fully recovered when the strands are totally unbinded at denaturation temperatures. At these temperatures, the coupling between the quencher the fluorophore is lost, allowing for a self-normalization of the PCR fluorescence signature. In contrast, the measurements made during annealing track the actual progression of the PCR.

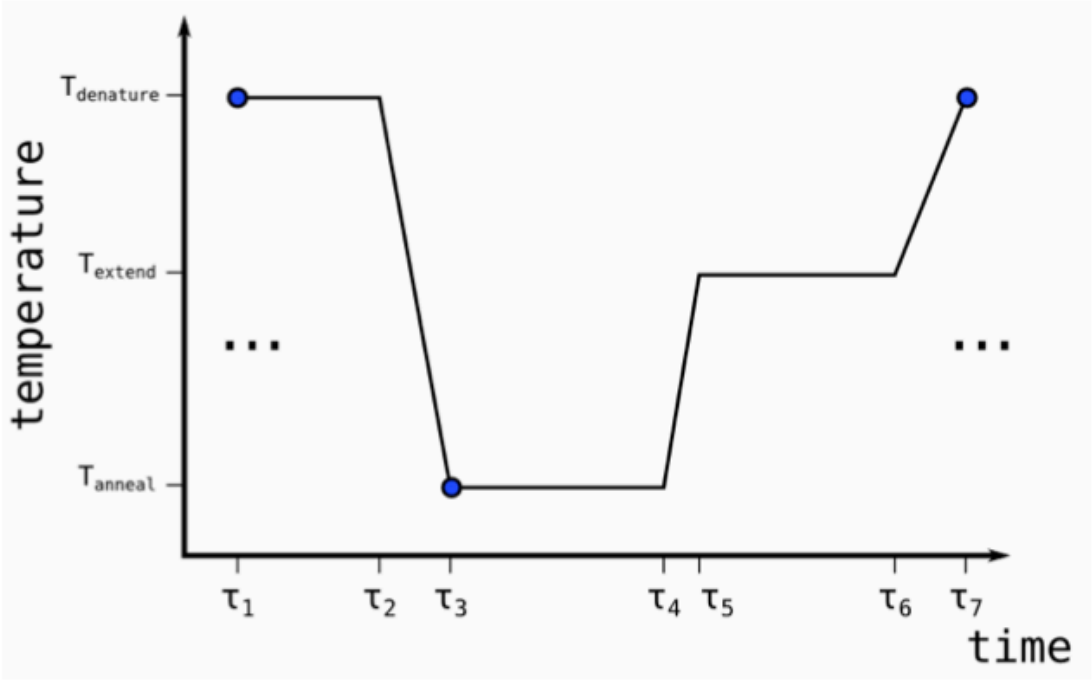

Figure 8.4 Temperature and light-intensity measurement schedule for tagged-primer PCR. Fluorometry is performed at both the denature and annealing temperatures.

Initial proof-of-principle of the primer-tagged technique was performed using synthetic nucleic acid targets chosen from the Human Immunodeficiency Virus 1 (HIV-1) TPP gene. We observed that this novel probe technique was successfully able to report on the progress of PCR (Figure 8.5), over a large dynamic range of initial TPP target concentrations. Wee found that the primer-tagged assay was equally sensitive and specific as the traditional HIV-1 TPP assay (described in chapter four).

Furthermore, we noticed that nucleic acid targets of varying lengths, for a giving tagged-primer set, exhibited characteristic fluorescence signatures. By testing this technique on HIV TPP targets ranging from 40bp to 190bp, we found that the extent of the endpoint quenched signature varied inversely with the length. Interestingly, the initial data did not fit the FRET fluorescence model, and was instead consistent with electronic conduction models suggested by other researchers [136-143].

Furthermore, initial observations indicate that a single base pair change affects the probability that a particular electron diffuses from the donor to the acceptor. For example, a single base-pair mismatch in a 80bp target causes a 35% change in collected fluorescence signal. Initial data

indicates that this effect is base-pair dependent (i.e. an A-T match, a T-T mismatch, a G-T mismatch, and a C-T mismatch all generate unique signatures). We suspect that any point mutations affect the electron forward conduction probability, and hence the quenched signal. This implies that this novel probe technique has the capability of being even more sensitive than traditional nucleic acid assays for detecting single point mutations. This will be the subject of subsequent research in both research and clinical environments.

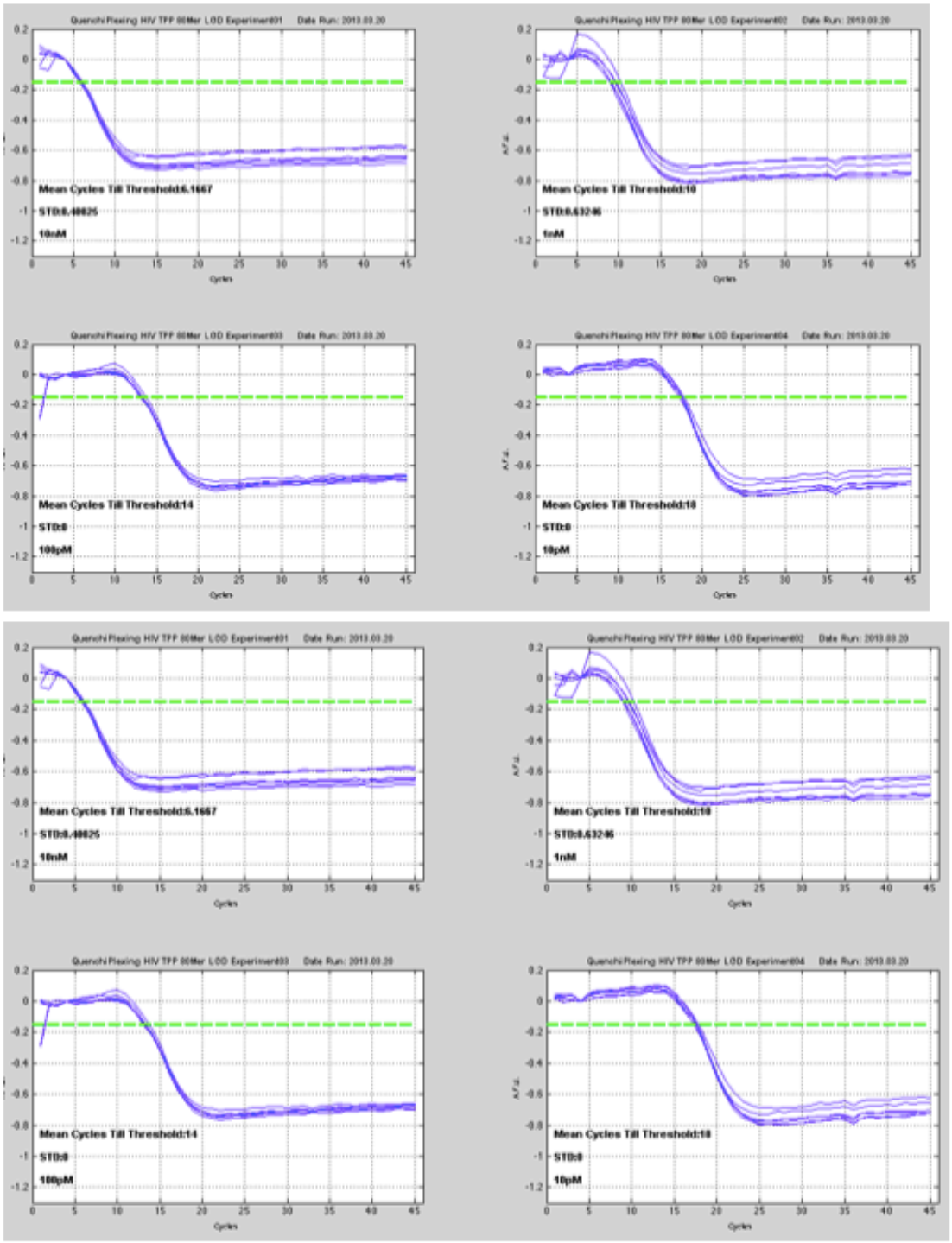

Figure 8.5 Successful primer-tagged PCR detection of HIV TPP targets. Initial experiments show the qPCR detection of 80bp HIV TPP targets at varying concentrations from 10 nM to 100 fM. All successful detection curves exhibit the inverse-sigmoidal characteristic.

Higher Density Coding

Part of the novelty of tagged-primer PCR is that chromaphores are permanently ligated onto the amplified strands. This allows for more sophisticated coding schemes. For example, consider a scheme where the ordering of identifying color distinguishes a particular sequence. Each nucleic acid target can have tagged-primer pairs of varying length that are selectively incorporated into the template strands as a function of the annealing temperature (Figure 8.6). By carefully controlling this temperature zone, the kinetics of the PCR reaction can be tailored to allow for the binding of a particular primer/probe with greater probability at a given cycle. For instance, longer primers can be exhausted first by initially having an annealing temperature that is higher than the melt temperature of the competitive smaller primers. As such, the kinetics of a PCR reaction, as well as the dynamics for reporting on that reaction, can be controlled by temperature alone.

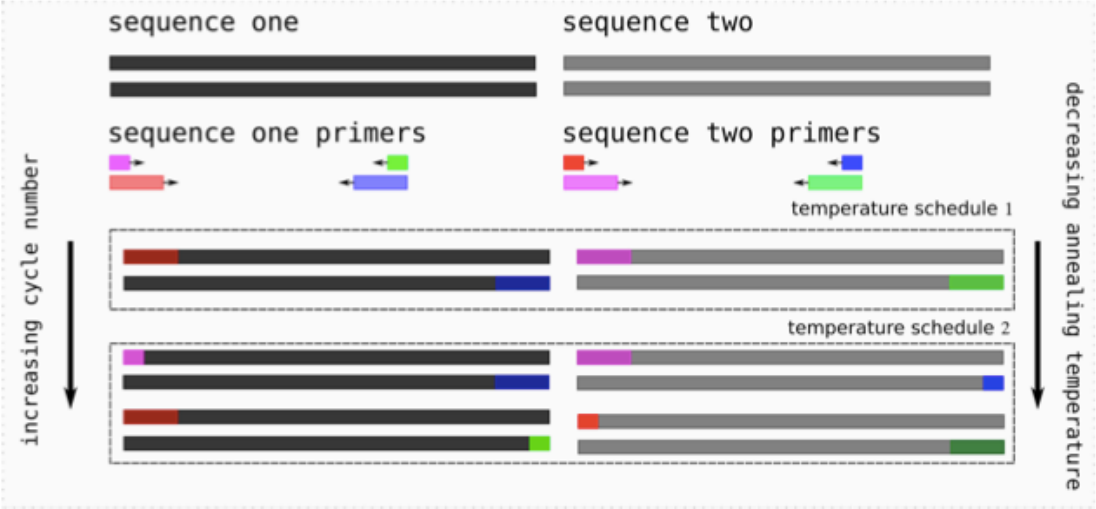

Figure 8.6 Higher density combinatorial coding of nucleic acid targets using tagged-primers.

This allows for the coding of PCR reactions using novel 2-dimensional labels of wavelength-temperature pairs. In its simplest iteration, the maximum occupancy for a specific temperature zone is four (one target, per color, per temperature step). In the case of a four color instrument, we can code for up to 16 targets in a single well (Table 8.2). As the PCR reaction proceeds, we look for changes in fluorescence in each color channel. If the change in a particular color crosses a threshold, we record this as the presence of a target.

Table 8.2 Mapping of wavelength-temperature pairs to code for particular sequences.

Color\Temperature	T1	T2	T3	T4
B	Seq01	Seq05	Seq09	Seq13
G	Seq02	Seq06	Seq10	Seq14
Y	Seq03	Seq07	Seq11	Seq15
R	Seq04	Seq08	Seq12	Seq16

Final Thoughts

The material reported in this thesis represents an initial foray into the use of engineering tools and techniques for biological measurement. While this has yielded encouraging initial results, there is still much to be explored. For example, more sophisticated microfluidic tools will allow for novel measurements on a variety of biochemical phenomena. Furthermore, analysis strategies borrowed from information theory and combinatorics will allow for more detailed analysis of these information-rich measurements. This will afford us more weapons with which we can analyze the biological world.

BIBLIOGRAPHY

1. Eteshola, E., and D. Leckband. "Development and characterization of an ELISA assay in PDMS microfluidic channels." *Sensors and Actuators B: Chemical* 72.2 (2001): 129-133.
2. Herrmann, M., T. Veres, and M. Tabrizian. "Enzymatically-generated fluorescent detection in micro-channels with internal magnetic mixing for the development of parallel microfluidic ELISA." *Lab on a Chip* 6.4 (2006): 555-560.
3. Hoegger, Daniela, et al. "Disposable microfluidic ELISA for the rapid determination of folic acid content in food products." *Analytical and bioanalytical chemistry* 387.1 (2007): 267-275.
4. Eteshola, Edward, and Michal Balberg. "Microfluidic ELISA: on-chip fluorescence imaging." *Biomedical microdevices* 6.1 (2004): 7-9.
5. Thorsen, Todd, Sebastian J. Maerkl, and Stephen R. Quake. "Microfluidic large-scale integration." *Science* 298.5593 (2002): 580-584.
6. Whitesides, George M. "The origins and the future of microfluidics." *Nature* 442.7101 (2006): 368-373.
7. Herrmann, Marc, et al. "Microfluidic ELISA on non-passivated PDMS chip using magnetic bead transfer inside dual networks of channels." *Lab on a Chip* 7.11 (2007): 1546-1552.
8. Lai, Siyi, et al. "Design of a compact disk-like microfluidic platform for enzyme-linked immunosorbent assay." *Analytical chemistry* 76.7 (2004): 1832-1837.
9. Yu, Ling, et al. "Flow-through functionalized PDMS microfluidic channels with dextran derivative for ELISAs." *Lab on a Chip* 9.9 (2009): 1243-1247.
10. Squires, Todd M., and Stephen R. Quake. "Microfluidics: Fluid physics at the nanoliter scale." *Reviews of modern physics* 77.3 (2005): 977.
11. Stone, Howard A., Abraham D. Stroock, and Armand Ajdari. "Engineering flows in small devices: microfluidics toward a lab-on-a-chip." *Annu. Rev. Fluid Mech.*36 (2004): 381-411.
12. Mullis, Kary B., and Fred A. Faloona. "Specific synthesis of DNA in vitro via a polymerase-catalyzed chain reaction." *Methods in enzymology* 155 (1987): 335.
13. M. Urdea et al. Nature S1, 73-79 (23 November 2006).
14. Agrawal, Nitin, Yassin A. Hassan, and Victor M. Ugaz. "A Pocket-Sized Convective PCR Thermocycler." *Angewandte Chemie International Edition* 46.23 (2007): 4316-4319.
15. Liu, P., Li, X., Greenspoon, S. A., Scherer, J. R. & Mathies, R. A. Integrated DNA purification, PCR, sample cleanup, and capillary electrophoresis microchip for forensic human identification. *Lab on a chip* **11,** 1041–8 (2011).
16. Schmitt, Markus, et al. "Bead-based multiplex genotyping of human papillomaviruses." *Journal of clinical microbiology* 44.2 (2006): 504-512.
17. de Lumley-Woodyear, Thierry, et al. "Rapid amperometric verification of PCR amplification of DNA." *Analytical chemistry* 71.3 (1999): 535-538.
18. M.U. Kopp, A.J. De Mello, A. Manz, Chemical amplification: continuous-flow PCR on a chip, Science 280 (1998) 1046–1048.
19. Kaigala, Govind V. "An inexpensive and portable microchip-based platform for integrated RT–PCR and capillary electrophoresis." *Analyst* 133.3 (2008): 331-338.

20. Zou, Quanbo, et al. "Micro-assembled multi-chamber thermal cycler for low-cost reaction chip thermal multiplexing." *Sensors and Actuators A: Physical*102.1 (2002): 114-121.
21. Belgrader, Phillip, et al. "A battery-powered notebook thermal cycler for rapid multiplex real-time PCR analysis." *Analytical chemistry* 73.2 (2001): 286-289.
22. Shen, Keyue, et al. "A microchip-based PCR device using flexible printed circuit technology." *Sensors and Actuators B: Chemical* 105.2 (2005): 251-258.
23. Zhao, Zhan, et al. "Monolithically integrated PCR biochip for DNA amplification." *Sensors and Actuators A: Physical* 108.1 (2003): 162-167.
24. Glazer, Alexander N., and Hays S. Rye. "Stable dye-DNA intercalation complexes as reagents for high-sensitivity fluorescence detection." *Nature*359.6398 (1992): 859-861.
25. Clegg, Robert M. "Fluorescence resonance energy transfer." *Current opinion in biotechnology* 6.1 (1995): 103-110.
26. Livak, Kenneth J., et al. "Oligonucleotides with fluorescent dyes at opposite ends provide a quenched probe system useful for detecting PCR product and nucleic acid hybridization." *Genome Research* 4.6 (1995): 357-362.
27. Holland, Pamela M., et al. "Detection of specific polymerase chain reaction product by utilizing the 5'----3'exonuclease activity of Thermus aquaticus DNA polymerase." *Proceedings of the National Academy of Sciences* 88.16 (1991): 7276-7280.
28. Figeys, Daniel, et al. "Use of the fluorescent intercalating dyes POPO-3, YOYO-3 and YOYO-1 for ultrasensitive detection of double-stranded DNA separated by capillary electrophoresis with hydroxypropylmethyl cellulose and non-cross-linked polyacrylamide." *Journal of Chromatography A* 669.1 (1994): 205-216.
29. Glazer, Alexander N., and Hays S. Rye. "Stable dye-DNA intercalation complexes as reagents for high-sensitivity fluorescence detection." *Nature* 359.6398 (1992): 859-861.
30. S. Semancik and R. Cavicchi, Acc. Chem. Res. **31**, 279 _1998_.
31. Simon, N. Barson, M. Bauer, and U. Weimar, Sens. Actuators B **73**, 1 (2001).
32. P. M. Sarro, A. W. van Herwaarden, and W. van der Vlist, Sens. Actuators A, **42**, 666 (1994).
33. J. Yeom, C. R. Field, B. Bae, R. I. Masel, and M. A. Shannon, J. Micromech. Microeng. **18**, 125001 (2008).
34. C. Zhang and D. Xing, Nucleic Acids Res. **35**, 4223 (2007).
35. C. Rossi, D. Briand, M. Dumonteuil, T. Camps, P. Q. Pham, and N. F. de Rooij, Sens. Actuators A **126**, 241 (2006).
36. J. Courbat, D. Briand, and N. F. de Rooij, Sens. Actuators, A **142**, 284 (2008).
37. M. D. Henry, S. Walavalkar, A. Homyk, and A. Scherer, Nanotechnology **20**, 255305 (2009).
38. *CRC Handbook of Chemistry and Physics*, edited by R. Weast (CRC, Boca Raton, 1983), p. F-125.
39. *CRC Handbook of Chemistry and Physics*, edited by R. Weast (CRC, Boca Raton, 2001),p. F-110.
40. C. H. Mastrangelo and R. S. Muller, Proceedings of the International Electron Devices Meeting, 1989.
41. P. Furjes, C. Dusco, M. Adam, J. Zeettner, and I. Barsony, Superlattices Microstruct. **35**, 455 (2004).
42. J. El-Ali, I. R. Perch-Nielsen, C. R. Poulsen, D. D. Bang, P. Telleman, and A. Wolff, Sens. Actuators, A **110**, 3 (2004).

43. D. Briand, S. Heimgartner, M. A. Gretillat, B. van der Schoot, and N. F. de Rooij, J. Micromech. Microeng. **12**, 971 (2002).
44. S. H. Kong, D. D. L. Wijngaards, and R. F. Wolffenbuttel, Sens. Actuators A **92**, 88 (2001).
45. A. Nitkowski and M. Lipson, Proceedings of the Conference on Lasers and Electro-Optics, 2008.
46. B. Fischer, A. Behrends, D. Freund, D. F. Lupton, and J. Merker, Platinum Met. Rev. **43**, 18 (1999).
47. W. E. Forsythe and E. Q. Adams, J. Opt. Soc. Am. **35**, 108 (1945).
48. E.P. Kartalov, W.F. Anderson, A. Scherer, J. Nanosci. Nanotechnol. 6 (8), 2265 (2006)
49. E.P. Kartalov, J. In-Vitro Diagnostic Technology, Sept (2006)
50. T.G. Henares, F. Mizutani, H. Hisamoto, Anal. Chim. Acta 611, 17 (2008)
51. X. Cheng, G. Chen, W.R. Rodriguez, Anal. Bioanal. Chem. 393, 487 (2009)
52. E.P. Kartalov, D.H. Lin, D.T. Lee, W.F. Anderson, C.R. Taylor, A. Scherer, Electrophoresis 29, 5010 (2008)
53. D.H. Lin, C.R. Taylor, W.F. Anderson, A. Scherer, E.P. Kartalov, J. Chromatogr. B, 878 (2009)
54. L.W. Henderson, Hemofiltration, Springer Verlag, (1986)
55. J.N. Lee, C. Park, G.M. Whitesides, Anal. Chem. 75, 6544 (2003)
56. J. Moorthy, D.J. Beebe, Lab Chip 3, 62 (2003)
57. S. Thorslund, O. Klett, F. Nikolajeff, K. Markides, J. Berquist, Biomed. Microdevices 8, 73 (2006)
58. V. VanDelinder, A. Groisman, Anal. Chem. 78, 3765 (2006)
59. R. Fan, O. Vermesh, A. Srivastava, B.K.H. Yen, L. Qin, H. Ahmad, G. A. Kwong, C.C. Liu, J. Gould, L. Hood, J.R. Heath, Nat. Biotechnol. 26(12), 1373 (2008)
60. J.C. McDonald, D.C. Duffy, J.R. Anderson, D.T. Chiu, H. Wu, O.J. Schueller, G.M.
61. Whitesides, Electrophoresis 21, 27 (2000)
62. Liew, M., Groll, M. C., et al. (2007). "Validating a custom multiplex ELISA against individual commercial immunoassays using clinical samples." *BioTechniques*, *42*(3), 327-333.
63. Wiese, R., Belosludtsev, Y., Powdrill, T., Thompson, P., & Hogan, M. (2001). "Simultaneous multianalyte ELISA performed on a microarray platform." *Clinical Chemistry*, *47*(8), 1451-7.
64. Sanger, F., Nicklen, S., & Coulson, A. R. (1977). DNA sequencing with chain-terminating. *Proceedings of the National Academy of Sciences of the United States of America*, *74*(12), 5463-5467.
65. Tyagi, S., Marras, S. a, & Kramer, F. R. (2000). Wavelength-shifting molecular beacons. *Nature biotechnology*, *18*(11), 1191-6.
66. Lee, L. G., Livak, K. J., Mullah, B., Graham, R. J., Vinayak, R. S., & Woudenberg, T. M. Seven-Color, Homogeneous Detection of Six PCR Products. *Biotec*, *27*(2), 342-349.
67. Vet, J. A. M., Majithia, A. R., Marras, S. A. E., Tyagi, S., Dube, S., Poiesz, B. J., & Kramer, F. R. (1999). Multiplex detection of four pathogenic retroviruses using. *Proceedings of the National Academy of Sciences of the United States of America*, *96*(May), 6394-6399.
68. S. P. A. Fodor, R. P. Rava, X. C. Huang, A. C. Pease, C. P. Holmes, C. L. Adams. "Multiplexed biochemical assays with biological chips." *Nature*, Vol. 364, p. 555 – 556.

69. Speicher, M. R., Ballard, S. G., & Ward, D. C. (1996). Karyotyping human chromosomes by combinatorial multi-fluor FISH. *Nature Genetics*, *12*, 368-376.
70. Huang, Q., Hu, Q., & Li, Q. (2007). Identification of 8 foodborne pathogens by multicolor combinational probe coding technology in a single real-time PCR. *Clinical chemistry*, *53*(10), 1741-8.
71. Huang, Q., Zheng, L., Zhu, Y., Zhang, J., Wen, H., Huang, J., Niu, J., et al. (2011). Multicolor combinatorial probe coding for real-time PCR. *PloS one*, *6*(1), e16033.
72. Henegariu, O., Heerema, N. A., Dlouhy, S. R., Vance, G. H., & Vogt, P. H. (1997). Multiplex PCR!: Critical Parameters and Step-by-step Protocol. *BioTechniques*, *511*(September), 504-511.
73. Chamberlain, J. S., Gibbs, R. A., Ranierl, J. E., Nguyen, P. N., & Thomas, C. (1988). Deletion screening of the Duchenne muscular dystrophy locus via multiplex DNA amplification. *Nucleic Acids Research*, *16*(23), 11141-11156.
74. Waters, L. C., Jacobson, S. C., Kroutchinina, N., Khandurina, J., Foote, R. S., & Ramsey, J. M. (1998). Microchip device for cell lysis, multiplex PCR amplification, and electrophoretic sizing. *Analytical chemistry*, *70*(1), 158-62.
75. Oliveira, D. C., & Lencastre, H. D. (2002). Multiplex PCR Strategy for Rapid Identification of Structural Types and Variants of the mec Element in Methicillin-Resistant Staphylococcus aureus. *Antimicrobial Agents and Chemotherapy*, *46*(7), 2155-2161.
76. Lao, K., Xu, N. L., Yeung, V., Chen, C., Livak, K. J., & Straus, N. a. (2006). Multiplexing RT-PCR for the detection of multiple miRNA species in small samples. *Biochemical and biophysical research communications*, *343*(1), 85-9.
77. Zhang, K., Mcclure, J.-ann, Elsayed, S., Conly, J. M., & Louie, T. (2005). Novel Multiplex PCR Assay for Characterization and Concomitant Subtyping of Staphylococcal Cassette Chromosome mec Types I to V in Methicillin-Resistant Staphylococcus aureus. *Journal of Clinical Microbiology*, *43*(10), 5026-5033.
78. El-hajj, H. H., Marras, S. A. E., Tyagi, S., Kramer, R., & Alland, D. (2001). Detection of Rifampin Resistance in Mycobacterium tuberculosis in a Single Tube with Molecular Beacons. *Journal of Clinical Microbiology*, *39*(11), 4131-4137.
79. Chong, S. S., Boehm, C. D., Higgs, D. R., & Cutting, G. R. (2000). Single-tube multiplex- PCR screen for common deletional determinants of alpha-thalassemia. *Blood*, *95*(1), 360-2.
80. Paton, A. W., & Paton, J. C. (1998). Detection and Characterization of Shiga Toxigenic Escherichia coli by Using Multiplex Enterohemorrhagic E . coli hlyA , rfb O111. *Journal of Clinical Microbiology*, *36*(2), 598-602.
81. Urdea, M., Penny, L. A., Olmsted, S. S., Giovanni, M. Y., Kaspar, P., Shepherd, A., Wilson, P., et al. (2006). Requirements for high impact diagnostics in the developing world. *Nature*, 73-79.
82. Patterson, B. K., Till, M., Otto, P., Furtado, M. R., Mcbride, L. J., & Wolinsky, S. M. (1993). Detection of HIV-1 DNA and Messenger RNA in Individual in Situ Hybridization Cells by PCR-Driven and Flow Cytometry. *Science*, *260*(5110), 976-979.
83. Roth, W. K., Weber, M., & Seifried, E. (1999). Feasibility and efficacy of routine PCR screening of blood donations for hepatitis C virus, hepatitis B virus, and HIV-1 in a blood- bank setting. *Lancet*, *353*(9150), 359-63.
84. Ptak, R. G., Gallay, P. A., Jochmans, D., Halestrap, A. P., Ruegg, U. T., Pallansch, L. A., Bobardt, M. D., et al. (2008). Inhibition of human immunodeficiency virus type 1 replication in human cells by Debio-025, a novel cyclophilin binding agent.

Antimicrobial Agents and Chemotherapy, *52*(4), 1302-17.
85. Ou, C.-Y., Kwok, S., Mitchell, S. W., Mack, D. H., Sninsky, J. J., Krebs, J. W., Feorino, P., et al. (1988). DNA Amplification for Direct Detection of HIV-1 in DNA of Peripheral Blood Mononuclear Cells. *Science*, *239*(4837), 295-29.
86. Website: http://www.hiv.lanl.gov/content/index [Accessed February 2012]
87. Heidari, M., Assmar, M., & Daloii, M. R. N. (2005). Detection of Plasmodium falciparum Directly from Blood Samples Using the Polymerase Chain Reaction. *Journal of Sciences, Islamic Republic of Iran*, *16*(1), 21-24.
88. Tirasophon, W., Ponglikitmongkol, M., Wilairat, P., Boonsaeng, V., & Panyim, S. (1991). A Novel Detection of a Single Plasmodium Falciparum in Infected Blood. *Biochemical and Biophysical Research Communications*, *175*(1), 179-184.
89. Website:http://microbes.ucsc.edu/cgibin/hgGateway?hgsid=612764&clade=eukaryota-protista&org=0&db=0 [Accessed February 2012]
90. Weidmann, M., Meyer-König, U., & Hufert, F. T. (2003). Rapid Detection of Herpes Simplex Virus and Varicella-Zoster Virus Infections by Real-Time PCR. *Journal of Clinical Microbiology*, *41*(4), 1565-1568.
91. Website:http://www.ebi.ac.uk/Tools/dbfetch/emblfetch?db=embl&id=AJ303204&format=default&sty le=default&Retrieve=Retrieve [Accessed February 2012]
92. Noordhoek, G. T., Kolk, A. H. J., Bjune, G., Catiy, D., Dale, J. W., Fine, P. E. M., Godfrey- Faussett, P., et al. (1994). Sensitivity and specificity of PCR for detection comparison study among seven laboratories . Sensitivity and Specificity of PCR for Detection of Mycobacterium tuberculosis!: a Blind Comparison Study among Seven Laboratories. *Journal of Clinical Microbiology*, *32*(2), 277-284.
93. Rosenstraus, M., Wang, Z., Chang, S.-yung, DeBonville, D., & Spadoro, J. P. (1998). An Internal Control for Routine Diagnostic PCR!: Design , Properties , and Effect on Clinical Performance. *Journal of Clinical Microbiology*, *36*(1), 191-197.
94. Beige, J., Lokies, J., Schaberg, T., Finckh, U., Fischer, M., Mauch, H., Lode, H., et al. (1995). Clinical evaluation of a Mycobacterium tuberculosis PCR assay. *Journal of Clinical Microbiology*, *33*(1), 90-95.
95. Website:http://www.ebi.ac.uk/Tools/dbfetch/emblfetch?db=embl&id=GQ395623&format=default&st yle=default&Retrieve=Retrieve [Accessed February 2012]
96. dos Santos, H. W. G., Poloni, T. R. R. S., Souza, K. P., Muller, V. D. M., Tremeschin, F., Nali, L. C., Fantinatti, L. R., et al. (2008). A Simple One-Step Real-Time RT-PCR for Diagnosis of Dengue Virus Infection. *Jounral of Medical Virology*, *80*, 1426-1433.
97. Website: http://www.ncbi.nlm.nih.gov/nuccore/M93130 [Accessed February 2012]
98. Livak, K. J., Flood, S. J. A., Marmaro, J., Giusti, W., & Deetz, K. (1995). Oligonucleotides with fluorescent dyes at opposite ends provide a quenched probe system useful for detecting PCR product and nucleic acid hybridization. *Genome Research*, *4*, 357-362.
99. Hartman, L. J., Coyne, S. R., & Norwood, D. a. (2005). Development of a novel internal positive control for Taqman based assays. *Molecular and cellular probes*, *19*(1), 51-9.
100. Jothikumar, P., Hill, V., & Narayanan, J. (2009). Design of FRET-TaqMan probes for multiplex real-time PCR using an internal positive control. *BioTechniques*, *46*(7), 519-24.
101. Chun, J.-Y., Kim, K.-J., Hwang, I.-T., Kim, Y.-J., Lee, D.-H., Lee, I.-K., & Kim, J.-K. (2007). Dual priming oligonucleotide system for the multiplex detection of respiratory viruses and SNP genotyping of CYP2C19 gene. *Nucleic acids research*,

35(6), e40.
102. Lee, H. R., Kim, S. Y., Chang, H. E., Song, S. H., Lee, H. S., Park, K. U., Song, J., et al. (2010). Novel multiplex PCR using dual-priming oligonucleotides for detection and discrimination of the Mycobacterium tuberculosis complex and M. bovis BCG. *Journal of clinical microbiology*, *48*(12), 4612-4.
103. Website: <http://www.nationalmssociety.org>
104. N. Tanuma, H. Sakuma, A. Sasaki. "Chemokine Expression by Astrocytes Plays a Role in Microglia Macrophage Activation and Subsequent Neurodegeneration in Secondary Progressive Multiple Sclerosis." *Acta Neuropathol*. Vol. 112, No. 2, 2006.
105. M. Ram, Y. Sherer, Y. Shoenfeld. "Matrix Metalloproteinase-9 and Autoimmune Diseases." *Journal of Clinical* Immunology. Vol. 26, No. 4, 2006.
106. P. Lalive, T. Menge, C. Delarasse, B. Gaspera, D. Pham-Dinh, P. Villoslada, H. von Budingen, and C. Genain. "Antibodies to Native Myelin Oligodendrocyte Glycoprotein are Serological Markers of Early Inflammation in Multiple Sclerosis." *PNAS*. Vol. 103, No. 7, 2006.
107. T. Menge, P. Lalive, H. Budingen, B. Cree, S. Hauser, and C. Genain. "Antibody Responses Against Galactocerebroside are Potential Stage-specific Biomarkers in Multiple Sclerosis." *Journal of Allergy and Clinical Immunology.* Vol. 116, No. 2, 2005.
108. E. Kartalov, J. Zhong, A. Scherer, S. Quake, and C. Taylor. "High-throughput multi- antigen microfluidic fluorescence." *BioTechniques*. Vol. 40, No. 1, 2006.
109. Alberts et al. *Molecular Biology of the Cell*. New York: Garland Science, 2002.
110. http://en.wikipedia.org/wiki/PCR.
111. http://en.wikipedia.org/wiki/Real_time_pcr.
112. Bailon et al. *Affinity Chromatography Methods and Protocols*.
113. http://en.wikipedia.org/wiki/Affinity_chromatography
114. Springer, Timothy. "Immunoaffinity Chromatography." *Current Protocols in Molecular Biology* (1996) 10.11.1-9.
115. V. Zhirnov, R. Cavin, J. Hutchby, G. Bourianoff. Proceedings of the IEEE, Vol. 91, No. 11, Nov. 2003.
116. Intel Corporation; http://www.intel.com/technology/silicon/mooreslaw/
117. HP Development Company website: http://www.hpl.hp.com/news/2003/oct_dec/energy_talk.html
118. http://codesign.ece.gatech.edu/publications/jcpark/paper/patmos_2004.pdf
119. A. Shakouri, Y. Zhang. *IEEE Transactions on Components and Packaging Technologies*, Vol. 28, No. 1, March 2005
120. G. Maltezos, A. Scherer, A. Rajagopal. *California Institute of Technology Patent Disclosure*, File Number: CIT-4466-PB
121. Miserendino, Scott, and Yu-Chong Tai. "Modular microfluidic interconnects using photodefinable silicone microgaskets and MEMS O-rings." *Sensors and Actuators A: Physical* 143.1 (2008): 7-13.
122. Shaikh, Kashan A., et al. "A modular microfluidic architecture for integrated biochemical analysis." *Proceedings of the National Academy of Sciences of the United States of America* 102.28 (2005): 9745-9750.
123. Grodzinski, P., et al. "A modular microfluidic system for cell pre-concentration and genetic sample preparation." *Biomedical Microdevices* 5.4 (2003): 303-310.
124. Fredrickson, Carl K., and Z. Hugh Fan. "Macro-to-micro interfaces for microfluidic devices." *Lab on a Chip* 4.6 (2004): 526-533.

125. Vogt, Oliver, et al. "A new two-chip concept for continuous measurements on PMMA-microchips." *Lab on a Chip* 5.2 (2005): 205-211.
126. Leatzow, Dan M., et al. "Attachment of plastic fluidic components to glass sensing surfaces." *Biosensors and Bioelectronics* 17.1 (2002): 105-110.
127. Golden, Joel, et al. "A "do-it-yourself" array biosensor." *Methods* 37.1 (2005): 65-72.
128. Schmitt,E., Panvert,M., Blanquet,S. and Mechulam,Y. (1995) Transition state stabilisation by the 'high' motif of class I aminoacyl-tRNA synthetases: the case of Escherichia coli methionyl-tRNA synthetase. Nucleic Acids Res., 23, 4793-4798.
129. Huynh,T.V., Young,R.A. and Davies,R.W. (1988) Constructing and screening cDNA libraries in lambdagt10 and lambdagt11. In Glover,D.M. (ed.), DNA Cloning - A Practical Approach. IRL Press, Oxford, Vol. I, pp. 49-78.
130. Maniatis,T., Fritsch,E.F. and Sambrook,J. (1982) Molecular Cloning: A Laboratory Manual. Cold Spring Harbor Laboratory Press, Cold Spring Harbor, NY.
131. Burnett,R.C. (1993) EMBL accession no. X52486.
132. Capaldi,S., Getts,R.C. and Jayasena,S.D. (2000) Signal amplification through nucleotide extension and excision on a dendritic DNA platform. Nucleic Acids Res., 28, e21.
133. Qiao,D., Chen,W., Stratagoules,E. and Martinez,J. (March 10, 2000) Bile acid-induced activation of activator protein-1 requires both extracellular signal-regulated kinase and protein kinase C signaling. J. Biol. Chem., 10.1074/jbc.M908890199
134. Qiao,D., Chen,W., Stratagoules,E. and Martinez,J. (2000) Bile acid-induced activation of activator protein-1 requires both extracellular signal-regulated kinase and protein kinase C signaling. J. Biol. Chem., 275, 15090-15098. First published on May 19, 2000, 10.1074/jbc.M908890199
135. Bernhagen,J., Elkine,B., Geiger,G., Tovar,G. and Vitzthum,F. (1999) Patent DE-198198889.2-44;; PCT/WO/EP/99/03047.
136. Kelley, Shana O., and Jacqueline K. Barton. "Electron transfer between bases in double helical DNA." *Science* 283.5400 (1999): 375-381.
137. Hall, Daniel B., R. Erik Holmlin, and Jacqueline K. Barton. "Oxidative DNA damage through long-range electron transfer." (1996): 731-735.
138. Kelley, Shana O., and Jacqueline K. Barton. "Electron transfer between bases in double helical DNA." *Science* 283.5400 (1999): 375-381.
139. Kim, Sang Tae, et al. "Determination of rates and yields of interchromophore (folate. fwdarw. flavin) energy transfer and intermolecular (flavin. fwdarw. DNA) electron transfer in Escherichia coli photolyase by time-resolved fluorescence and absorption spectroscopy." *Biochemistry* 30.47 (1991): 11262-11270.
140. Fukui, Keijiro, and Kazuyoshi Tanaka. "Distance dependence of photoinduced electron transfer in DNA." *Angewandte Chemie International Edition* 37.1-2 (1998): 158-161.
141. Baguley, Bruce C., and Marc Le Bret. "Quenching of DNA-ethidium fluorescence by amsacrine and other antitumor agents: a possible electron-transfer effect." *Biochemistry* 23.5 (1984): 937-943.
142. Priyadarshy, S., S. M. Risser, and D. N. Beratan. "DNA is not a molecular wire: protein-like electron-transfer predicted for an extended π-electron system." *The Journal of Physical Chemistry* 100.44 (1996): 17678-17682.
143. Didenko, Vladimir V. "DNA probes using fluorescence resonance energy transfer (FRET): designs and applications." *Biotechniques* 31.5 (2001): 1106.
144. Patterson, B. K., Till, M., Otto, P., Furtado, M. R., Mcbride, L. J., & Wolinsky,

S. M. (1993). Detection of HIV-1 DNA and Messenger RNA in Individual in Situ Hybridization Cells by PCR-Driven and Flow Cytometry. Science, 260(5110), 976-979.

145. Roth, W. K., Weber, M., & Seifried, E. (1999). Feasibility and efficacy of routine PCR screening of blood donations for hepatitis C virus, hepatitis B virus, and HIV-1 in a blood-bank setting. Lancet, 353(9150), 359-63.

146. Ptak, R. G., Gallay, P. A., Jochmans, D., Halestrap, A. P., Ruegg, U. T., Pallansch, L. A., Bobardt, M. D., et al. (2008). Inhibition of human immunodeficiency virus type 1 replication in human cells by Debio-025, a novel cyclophilin binding agent. Antimicrobial Agents and Chemotherapy, 52(4), 1302-17.

147. Ou, C.-Y., Kwok, S., Mitchell, S. W., Mack, D. H., Sninsky, J. J., Krebs, J. W., Feorino, P., et al. (1988). DNA Amplification for Direct Detection of HIV-1 in DNA of Peripheral Blood Mononuclear Cells. Science, 239(4837), 295-29.

148. Li, Jin, and G. Mike Makrigiorgos. "Anti-primer quenching-based real-time PCR for simplex or multiplex DNA quantification and single-nucleotide polymorphism genotyping." *Nature Protocols* 2.1 (2007): 50-58.

A p p e n d i x A

PCR REACTION PROTOCOLS

All PCR reactions were performed on a Roche 480 LightCycler instrument (Roche Applied Science, Penzberg, Germany). The PCR cycling reaction was run for 45 cycles, with a 60 sec hot-start at 95°C. The cycling conditions were: denaturation for 45 sec at 95°C, annealing for 50 sec at 65°C, and extension for 60 sec at 70°C. Each experiment was run in quintuplicate, with a reaction volume of 15μL. Fluoresence measurements in 483nm-533nm (FAM), 523nm-568nm (Cy3), 558nm-610nm (ROX), and 615nm-670nm (Cy5) were first taken after the hot-start, and again taken at the end of 45 thermal cycles. The change in fluorescence intensity between these two measurements, for each instance of an experiment, determined the fluorescent signal.

Positive control experiments were performed to determine base-line fluorescence levels for each target and set of probes. Only targets with their associated probes were cycled in experiments 1, 3, 5, 7, 9, tabulated in Tables A.9, A.11, A.13, A.15, A.17, A.19. These were positive-control experiments that provided baseline fluorescence intensity for each oligo target. The change in fluorescence intensity, in each color, was used to assemble the expected cumulative signal levels in the chromatograms in Figure 4.1. The combinatorial superposition of fluorescence levels, in each independent wavelength channel, determined the actual bands for each count. Experiments 2, 4, 6, 8, 10, measured the extent of cross-talk.

Experiments 11, 12, 13, 14, tabulated in Tables A.11 – A.14, were multiplex coding experiments. Their changes of fluorescence intensity in each color was presented by the black circles in the chromatograms of Figure 4.1.

Experiments 23 – 27, tabulated in Tables A.23 – A.29, were binary-coded multiplex experiments in the FAM channel. The change in fluorescence intensity at the end of the saturated PCR experiment was presented by the black circles in the chromatograms of Figure 2. In each case, the multiplicity count corresponded to a unique combination of present targets. The baseline concentration for a 1x count was determined by a set of

fluorophore titration experiments. A 200nM 1x concentration of probes in the FAM channel allowed for a sufficiently strong signal that minimized cross-channel bleed through.

In any particular experiment, the uncertainty in the cycling data was determined by the spread of values in the last five cycles of the particular amplification reaction. This uncertainty did not scale with the value of the total signal, which implied that the source of uncertainty was instrumental rather than experimental. A 1x fluorphore (200nM) baseline was determined by statistical analysis of a set of data on 200nM concentration. The expected multiplicative signal levels were determined by multiplying this baseline by the multiplicity.

Sequence Information	HIV-1 Poly protease 198mer synthesized from bases 2253 – 2550
Source	HIV-1 Reference Sequence, Los Alamos National Laboratory
Target sequence (3' to 5')	GGAAGCTCTATTAGATACAGGAGCAGATGATACAGTATTAG AAGAAATGAGTTTGCCAGGAAGATGGAAACCAAAAATGAT AGGGGGAATTGGAGGTTTTATCAAAGTAAGACAGTATGATC AGATACTCATAGAAATCTGTGGACATAAAGCTATAGGTACA GTATTAGTAGGACCTACACCTGTCAACATAATTGG
Forward Primer (3' to 5')	GGAAGCTCTATTAGATACAGGAGCAG
Reverse Primer (3' to 5')	CCAATTATGTTGACAGGTGTAGGTCC
Probe 1 (3' to 5')	/**56-FAM**/TGAGTTTGCCAGGAAGATGGAAACCA/3BHQ_1/

Table A.1 HIV-1 Poly Protease Sequence Information

Sequence Name	HIV-1 P17 199mer synthesized from bases 790 – 1186
Source	HIV-1 Reference Sequence, Los Alamos National Laboratory
Target sequence (3' to 5')	CAGCTACAACCATCCCTTCAGACAGGATCAGAAGAACTTAG ATCATTATATAATACAGTAGCAACCCTCTATTGTGTGCATCA AAGGATAGAGATAAAAGACACCAAGGAAGCTTTAGACAAG ATAGAGGAAGAGCAAAACAAAAGTAAGAAAAAAGCACAGC AAGCAGCAGCTGACACAGGACACAGCAATCAGGTCA
Forward Primer (3' to 5')	CAGCTACAACCATCCCTTCAGACA
Reverse Primer (3' to 5')	TGACCTGATTGCTGTGTCCTGTGT
Probe 1 (3' to 5')	/**56-FAM**/AGCAACCCTCTATTGTGTGCATCAAAGG/3BHQ_1
Probe 2 (3' to 5')	/**5Cy3**/AAAGCACAGCAAGCAGCAGCTGA/3BHQ_2/

Table A.2 HIV-1 P17 Sequence Information

Sequence Name	Malaria ChR7 199mer synthesized from bases 1139138 - 1141223
Source	UCSC Plasmodium falciparum Genome Browser Gateway
Target sequence (3' to 5')	GCCTAACATGGCTATGACGGGTAACGGGGAATTAGAGTTCG ATTCCGGAGAGGGAGCCTGAGAAATAGCTACCACATCTAAG GAAGGCAGCAGGCGCGTAAATTACCCAATTCTAAAGAAGA GAGGTAGTGACAAGAAATAACAATGCAAGGCCAATTTAAA ACCTTCCCAGAGTAACAATTGGAGGGCAAGTCTGGTG
Forward Primer (3' to 5')	GCCTAACATGGCTATGACGGGTAA
Reverse Primer (3' to 5')	CACCAGACTTGCCCTCCAATTGTT
Probe 1 (3' to 5')	/**56-FAM**/ATTCCGGAGAGGGAGCCTGAGAAATA/3BHQ_1/
Probe 2 (3' to 5')	/**56-ROXN**/AAGGAAGGCAGCAGGCGCGTAAATTA/3BHQ_2/

Table A.3 Malaria ChR7 Sequence Information

Sequence Name	HSV-2 193mer synthesized from HSV-2 genome
Source	EMBL Bank AJ303204
Target sequence (3' to 5')	TCAGCCCATCCTCCTTCGGCAGTATGGAGGGTGTCGCGGCG GCGAGCCGCCGTCCCCAAAGACGTGCGGGTCGTACACGTAC ACGTACCAGGGCGGCGGGCCTCCGACCCGGTACGCTCTCGT AAATGCTTCCCTGCTGGTGCCGATCTGGGACCGCGCCGCGG AGACATTCGAGTACCAGATCGAACTCGG
Forward Primer (3' to 5')	TCAGCCCATCCTCCTTCGGCAGTAT
Reverse Primer (3' to 5')	CCGAGTTCGATCTGGTACTCGAATGT
Probe 1 (3' to 5')	/**56-FAM**/AAAGACGTGCGGGTCGTACACGTACA/3BHQ_1/
Probe 2 (3' to 5')	/**5Cy5**/TAAATGCTTCCCTGCTGGTGCCGAT/3IAbRQSp/

Table A.4 Herpes Simplex Virus-2 Sequence Information

Sequence Name	Mycobacterium Tuberculosis rpoB 200mer synthesized from Mycobacterium tuberculosis rpoB genome
Source	EMBL Bank GQ395623
Target sequence (3' to 5')	GAGTGCAAAGACAAGGACATGACGTACGCGGCCCCGCTGTT CGTCACGGCCGAGTTCATCAACAACAACACCGGCGAGATCA AGAGCCAGACGGTGTTCATGGGTGACTTCCCGATGATGACC GAGAAGGGCACCTTCATCATCAACGGCACCGAGCGCGTCGT GGTCAGCCAGCTGGTCCGCTCGCCCGGTGTGTACTT
Forward Primer (3' to 5')	GAGTGCAAAGACAAGGACATGACG
Reverse Primer (3' to 5')	AAGTACACACCGGGCGAGC
Probe 1 (3' to 5')	/**56-FAM**/CGCTGTTCGTCACGGCCGAGTTCAT/3BHQ_1/
Probe 2 (3' to 5')	/**5Cy3**/AGATCAAGAGCCAGACGGTGTTCATG/3BHQ_2/
Probe 3 (3' to 5')	/**5Cy5**/AAGGGCACCTTCATCATCAACGGCA/3IAbRQSp/

Table A.5 Tuberculosis rpoB Sequence Information

Sequence Name	Dengue Virus Type 3 200mer synthesized from Dengue Virus Type 3 genome
Source	GenBank M93130
Target sequence (3' to 5')	ATGCCAACTGTGATTGAGCACTTAGAAAGACTACAAAGGAA ACATGGAGGAATGCTTGTGAGAAATCCACTCTCACGAAACT CCACGCACGAAATGTATTGGATATCCAATGGTACAGGCAAC ATCGTCTCATTCACAATGACACACAGGAGACCCACCATAGA GAAAGATGTGGATTTAGGAGCAGGAACCCGACATGT
Forward Primer (3' to 5')	ATGCCAACTGTGATTGAGCACT
Reverse Primer (3' to 5')	ACATGTCGGGTTCCTGCTCCTAAA
Probe 1 (3' to 5')	/**56-FAM**/ACAAAGGAAACATGGAGGAATGCTTGTGA/3BHQ_1/
Probe 2 (3' to 5')	/**5Cy3**/ACTCTCACGAAACTCCACGCACGAAA/3BHQ_2/
Probe 3 (3' to 5')	/**56-ROXN**/ACAATGACACACAGGAGACCCACCAT/3BHQ_2/
Probe 4 (3' to 5')	/**5Cy5**/GGATATCCAATGGTACAGGCAACATCGT/3IAbRQSp/

Table A.6 Tuberculosis rpoB Sequence Information

Reagents	Concentration	Volume Added
UltraPure Water	-	34µL
Taq 5x Master Mix	-	42µL
Templates	Concentration	Volume Added
Poly Protease Template	17nM	2µL
Primers	Concentration	Volume Added
Poly Protease FWD Primer	1µM	2µL
Poly Protease RVS Primer	1µM	2µL
Probes	Concentration	Volume Added
Poly Protease Probe 1	1µM	2µL

Table A.7 Experiment 1 Cocktail

Reagents	Concentration	Volume Added
UltraPure Water	-	28µL
Taq 5x Master Mix	-	42µL
Templates	Concentration	Volume Added
Malaria Template	15nM	2µL
Herpes Template	17nM	2µL
TB Template	16nM	2µL
Dengue Virus Template	17nM	2µL
Primers	Concentration	Volume Added
Poly Protease FWD Primer	1µM	2µL
Poly Protease RVS Primer	1µM	2µL
Probes	Concentration	Volume Added
Poly Protease Probe 1	1µM	2µL

Table A.8 Experiment 2 Cocktail

Reagents	Concentration	Volume Added
UltraPure Water	-	32µL
Taq 5x Master Mix	-	42µL
Templates	Concentration	Volume Added
Malaria Template	15nM	2µL
Primers	Concentration	Volume Added
Malaria FWD Primer	1µM	2µL
Malaria RVS Primer	1µM	2µL
Probes	Concentration	Volume Added
Malaria Probe 1	1µM	2µL
Malaria Probe 2	1µM	2µL

Table A.9 Experiment 3 Cocktail

Reagents	Concentration	Volume Added
UltraPure Water	-	26µL
Taq 5x Master Mix	-	42µL
Templates	Concentration	Volume Added
Poly Protease Template	17nM	2µL
Herpes Template	17nM	2µL
TB Template	16nM	2µL
Dengue Virus Template	17nM	2µL
Primers	Concentration	Volume Added
Malaria FWD Primer	1µM	2µL
Malaria RVS Primer	1µM	2µL
Probes	Concentration	Volume Added
Malaria Probe 1	1µM	2µL
Malaria Probe 2	1µM	2µL

Table A.10 Experiment 4 Cocktail

Reagents	Concentration	Volume Added
UltraPure Water	-	32µL
Taq 5x Master Mix	-	42µL
Templates	Concentration	Volume Added
Herpes Template	17nM	2µL
Primers	Concentration	Volume Added
Herpes FWD Primer	1µM	2µL
Herpes RVS Primer	1µM	2µL
Probes	Concentration	Volume Added
Herpes Probe 1	1µM	2µL
Herpes Probe 2	1µM	2µL

Table A.11 Experiment 5 Cocktail

Reagents	Concentration	Volume Added
UltraPure Water	-	26µL
Taq 5x Master Mix	-	42µL
Templates	Concentration	Volume Added
Poly Protease Template	17nM	2µL
Malaria Template	15nM	2µL
TB Template	16nM	2µL
Dengue Virus Template	17nM	2µL
Primers	Concentration	Volume Added
Herpes FWD Primer	1µM	2µL
Herpes RVS Primer	1µM	2µL
Probes	Concentration	Volume Added
Herpes Probe 1	1µM	2µL
Herpes Probe 2	1µM	2µL

Table A.12 Experiment 6 Cocktail

Reagents	Concentration	Volume Added
UltraPure Water	-	30µL
Taq 5x Master Mix	-	42µL
Templates	Concentration	Volume Added
TB Template	16nM	2µL
Primers	Concentration	Volume Added
TB FWD Primer	1µM	2µL
TB RVS Primer	1µM	2µL
Probes	Concentration	Volume Added
TB Probe 1	1µM	2µL
TB Probe 2	1µM	2µL
TB Probe 3	1µM	2µL

Table A.13 Experiment 7 Cocktail

Reagents	Concentration	Volume Added
UltraPure Water	-	30µL
Taq 5x Master Mix	-	42µL
Templates	Concentration	Volume Added
Poly Protease Template	17nM	2µL
Malaria Template	15nM	2µL
Herpes Template	17nM	2µL
Dengue Virus Template	17nM	2µL
Primers	Concentration	Volume Added
TB FWD Primer	1µM	2µL
TB RVS Primer	1µM	2µL
Probes	Concentration	Volume Added
TB Probe 1	1µM	2µL
TB Probe 2	1µM	2µL
TB Probe 3	1µM	2µL

Table A.14 Experiment 8 Cocktail

Reagents	Concentration	Volume Added
UltraPure Water	-	28µL
Taq 5x Master Mix	-	42µL
Templates	Concentration	Volume Added
Dengue Virus Template	17nM	2µL
Primers	Concentration	Volume Added
Dengue Virus FWD Primer	1µM	2µL
Dengue Virus RVS Primer	1µM	2µL
Probes	Concentration	Volume Added
Dengue Virus Probe 1	1µM	2µL
Dengue Virus Probe 2	1µM	2µL
Dengue Virus Probe 3	1µM	2µL
Dengue Virus Probe 4	1µM	2µL

Table A.15 Experiment 9 Cocktail

Reagents	Concentration	Volume Added
UltraPure Water	-	22µL
Taq 5x Master Mix	-	42µL
Templates	Concentration	Volume Added
Poly Protease Template	17nM	2µL
Malaria Template	15nM	2µL
Herpes Template	17nM	2µL
TB Template	16nM	2µL
Primers	Concentration	Volume Added
Dengue Virus FWD Primer	1µM	2µL
Dengue Virus RVS Primer	1µM	2µL
Probes	Concentration	Volume Added
Dengue Virus Probe 1	1µM	2µL
Dengue Virus Probe 2	1µM	2µL
Dengue Virus Probe 3	1µM	2µL
Dengue Virus Probe 4	1µM	2µL

Table A.16 Experiment 10 Cocktail

Reagents	Concentration	Volume Added
Taq 5x Master Mix	-	42µL
Templates	**Concentration**	**Volume Added**
Poly Protease Template	17nM	2µL
Malaria Template	15nM	2µL
Herpes Template	17nM	2µL
Dengue Virus Template	17nM	2µL
Primers	**Concentration**	**Volume Added**
Poly Protease FWD Primer	1µM	2µL
Poly Protease RVS Primer	1µM	2µL
Malaria FWD Primer	1µM	2µL
Malaria RVS Primer	1µM	2µL
Herpes FWD Primer	1µM	2µL
Herpes RVS Primer	1µM	2µL
Dengue Virus FWD Primer	1µM	2µL
Dengue Virus RVS Primer	1µM	2µL
Probes	**Concentration**	**Volume Added**
Poly Protease Probe 1	1µM	2µL
Malaria Probe 1	1µM	2µL
Malaria Probe 2	1µM	2µL
Herpes Probe 1	1µM	2µL
Herpes Probe 2	1µM	2µL
Dengue Virus Probe 1	1µM	2µL
Dengue Virus Probe 2	1µM	2µL
Dengue Virus Probe 3	1µM	2µL
Dengue Virus Probe 4	1µM	2µL

Table A.17 Experiment 11 Cocktail

Reagents	Concentration	Volume Added
UltraPure Water	-	2µL
Taq 5x Master Mix	-	42µL
Templates	Concentration	Volume Added
Poly Protease Template	17nM	2µL
Malaria Template	15nM	2µL
Herpes Template	17nM	2µL
TB Template	16nM	2µL
Primers	Concentration	Volume Added
Poly Protease FWD Primer	1µM	2µL
Poly Protease RVS Primer	1µM	2µL
Malaria FWD Primer	1µM	2µL
Malaria RVS Primer	1µM	2µL
Herpes FWD Primer	1µM	2µL
Herpes RVS Primer	1µM	2µL
TB FWD Primer	1µM	2µL
TB RVS Primer	1µM	2µL
Probes	Concentration	Volume Added
Poly Protease Probe 1	1µM	2µL
Malaria Probe 1	1µM	2µL
Malaria Probe 2	1µM	2µL
Herpes Probe 1	1µM	2µL
Herpes Probe 2	1µM	2µL
TB Probe 1	1µM	2µL
TB Probe 2	1µM	2µL
TB Probe 3	1µM	2µL

Table A.18 Experiment 12 Cocktail

Reagents	Concentration	Volume Added
UltraPure Water	-	12µL
Taq 5x Master Mix	-	42µL
Templates	Concentration	Volume Added
Poly Protease Template	17nM	2µL
Herpes Template	17nM	2µL
TB Template	16nM	2µL
Primers	Concentration	Volume Added
Poly Protease FWD Primer	1µM	2µL
Poly Protease RVS Primer	1µM	2µL
Herpes FWD Primer	1µM	2µL
Herpes RVS Primer	1µM	2µL
TB FWD Primer	1µM	2µL
TB RVS Primer	1µM	2µL
Probes	Concentration	Volume Added
Poly Protease Probe 1	1µM	2µL
Herpes Probe 1	1µM	2µL
Herpes Probe 2	1µM	2µL
TB Probe 1	1µM	2µL
TB Probe 2	1µM	2µL
TB Probe 3	1µM	2µL

Table A.19 Experiment 13 Cocktail

Reagents	Concentration	Volume Added
UltraPure Water	-	10µL
Taq 5x Master Mix	-	42µL
Templates	Concentration	Volume Added
Poly Protease Template	17nM	2µL
Malaria Template	15nM	2µL
Dengue Virus Template	17nM	2µL
Primers	Concentration	Volume Added
Poly Protease FWD Primer	1µM	2µL
Poly Protease RVS Primer	1µM	2µL
Malaria FWD Primer	1µM	2µL
Malaria RVS Primer	1µM	2µL
Dengue Virus FWD Primer	1µM	2µL
Dengue Virus RVS Primer	1µM	2µL
Probes	Concentration	Volume Added
Poly Protease Probe 1	1µM	2µL
Malaria Probe 1	1µM	2µL
Malaria Probe 2	1µM	2µL
Dengue Virus Probe 1	1µM	2µL
Dengue Virus Probe 2	1µM	2µL
Dengue Virus Probe 3	1µM	2µL
Dengue Virus Probe 4	1µM	2µL

Table A.20 Experiment 14 Cocktail

Reagents	Concentration	Volume Added
UltraPure Water	-	50µL
Taq 5x Master Mix	-	25µL
Templates	Concentration	Volume Added
Poly Protease Template	17nM	4µL
P17 Template	15nM	4µL
Dengue Virus Template	17nM	4µL
Primers	Concentration	Volume Added
Poly Protease FWD Primer	1µM	4µL
Poly Protease RVS Primer	1µM	4µL
P17 FWD Primer	1µM	4µL
P17 RVS Primer	1µM	4µL
Dengue Virus FWD Primer	1µM	4µL
Dengue Virus RVS Primer	1µM	4µL
Probes	Concentration	Volume Added
Poly Protease Probe 1	800nM	4µL
P17 Probe 1	400nM	4µL
Dengue Virus Probe 1	200nM	4µL

Table A.21 Binary FAM Experiment 1 Cocktail

Reagents	Concentration	Volume Added
UltraPure Water	-	54µL
Taq 5x Master Mix	-	25µL
Templates	Concentration	Volume Added
Poly Protease Template	17nM	-
P17 Template	15nM	4µL
Dengue Virus Template	17nM	4µL
Primers	Concentration	Volume Added
Poly Protease FWD Primer	1µM	4µL
Poly Protease RVS Primer	1µM	4µL
P17 FWD Primer	1µM	4µL
P17 RVS Primer	1µM	4µL
Dengue Virus FWD Primer	1µM	4µL
Dengue Virus RVS Primer	1µM	4µL
Probes	Concentration	Volume Added
Poly Protease Probe 1	800nM	4µL
P17 Probe 1	400nM	4µL
Dengue Virus Probe 1	200nM	4µL

Table A.22 Binary FAM Experiment 2 Cocktail

Reagents	Concentration	Volume Added
UltraPure Water	-	54µL
Taq 5x Master Mix	-	25µL
Templates	Concentration	Volume Added
Poly Protease Template	17nM	4µL
P17 Template	15nM	-
Dengue Virus Template	17nM	4µL
Primers	Concentration	Volume Added
Poly Protease FWD Primer	1µM	4µL
Poly Protease RVS Primer	1µM	4µL
P17 FWD Primer	1µM	4µL
P17 RVS Primer	1µM	4µL
Dengue Virus FWD Primer	1µM	4µL
Dengue Virus RVS Primer	1µM	4µL
Probes	Concentration	Volume Added
Poly Protease Probe 1	800nM	4µL
P17 Probe 1	400nM	4µL
Dengue Virus Probe 1	200nM	4µL

Table A.23 Binary FAM Experiment 3 Cocktail

Reagents	Concentration	Volume Added
UltraPure Water	-	54µL
Taq 5x Master Mix	-	25µL
Templates	Concentration	Volume Added
Poly Protease Template	17nM	4µL
P17 Template	15nM	4µL
Dengue Virus Template	17nM	-
Primers	Concentration	Volume Added
Poly Protease FWD Primer	1µM	4µL
Poly Protease RVS Primer	1µM	4µL
P17 FWD Primer	1µM	4µL
P17 RVS Primer	1µM	4µL
Dengue Virus FWD Primer	1µM	4µL
Dengue Virus RVS Primer	1µM	4µL
Probes	Concentration	Volume Added
Poly Protease Probe 1	800nM	4µL
P17 Probe 1	400nM	4µL
Dengue Virus Probe 1	200nM	4µL

Table A.24 Binary FAM Experiment 4 Cocktail

Reagents	Concentration	Volume Added
UltraPure Water	-	58µL
Taq 5x Master Mix	-	25µL
Templates	Concentration	Volume Added
Poly Protease Template	17nM	-
P17 Template	15nM	-
Dengue Virus Template	17nM	4µL
Primers	Concentration	Volume Added
Poly Protease FWD Primer	1µM	4µL
Poly Protease RVS Primer	1µM	4µL
P17 FWD Primer	1µM	4µL
P17 RVS Primer	1µM	4µL
Dengue Virus FWD Primer	1µM	4µL
Dengue Virus RVS Primer	1µM	4µL
Probes	Concentration	Volume Added
Poly Protease Probe 1	800nM	4µL
P17 Probe 1	400nM	4µL
Dengue Virus Probe 1	200nM	4µL

Table A.25 Binary FAM Experiment 5 Cocktail

Reagents	Concentration	Volume Added
UltraPure Water	-	58µL
Taq 5x Master Mix	-	25µL
Templates	Concentration	Volume Added
Poly Protease Template	17nM	-
P17 Template	15nM	4µL
Dengue Virus Template	17nM	-
Primers	Concentration	Volume Added
Poly Protease FWD Primer	1µM	4µL
Poly Protease RVS Primer	1µM	4µL
P17 FWD Primer	1µM	4µL
P17 RVS Primer	1µM	4µL
Dengue Virus FWD Primer	1µM	4µL
Dengue Virus RVS Primer	1µM	4µL
Probes	Concentration	Volume Added
Poly Protease Probe 1	800nM	4µL
P17 Probe 1	400nM	4µL
Dengue Virus Probe 1	200nM	4µL

Table A.26 Binary FAM Experiment 6 Cocktail

Reagents	Concentration	Volume Added
UltraPure Water	-	58µL
Taq 5x Master Mix	-	25µL
Templates	Concentration	Volume Added
Poly Protease Template	17nM	4µL
P17 Template	15nM	-
Dengue Virus Template	17nM	-
Primers	Concentration	Volume Added
Poly Protease FWD Primer	1µM	4µL
Poly Protease RVS Primer	1µM	4µL
P17 FWD Primer	1µM	4µL
P17 RVS Primer	1µM	4µL
Dengue Virus FWD Primer	1µM	4µL
Dengue Virus RVS Primer	1µM	4µL
Probes	Concentration	Volume Added
Poly Protease Probe 1	800nM	4µL
P17 Probe 1	400nM	4µL
Dengue Virus Probe 1	200nM	4µL

Table A.27 Binary FAM Experiment 7 Cocktail

.

A p p e n d i x B

SEQUENCE INFORMATION

Sequence Information	HIV-1 40mer, 60mer, and 80mer
Source	HIV-1 Reference Sequence, Los Alamos National Laboratory
40Mer Template	5'- GGA AGC TCT ATT AGA TAC AGA CAC CTG TCA ACA TAA TTG G -3'
60Mer Template	5'- GGA AGC TCT ATT AGA TAC AGA TGA TAC AGT ATT AGA AGA AAC ACC TGT CAA CAT AAT TGG -3'
80Mer Template	5'- GGA AGC TCT ATT AGA TAC AGA TGA TAC AGT ATT AGA AGA AAT GAG TTT GCC AGG AAG ATG ACA CCT GTC AAC ATA ATT GG -3'
FWD Primer	5'- /5Cy3/GG AAG CTC TAT TAG ATA CAG -3'
RWD Primer	5'- /5IABkFQ/CC AAT TAT GTT GAC AGG TGT -3'

Table 8.1 HIV-1 Poly Protease Sequence Information

Sequence Information	Influenza A
Source	GenBank Accession #M23976.1 Influenza A
85Mer Template	5' GTA GGG ATA GAC CCT TTC AAA CTG CTT CAA AAC AGC CAA GTA TAC AGC CTA ATC AGA CCG AAT GAG AAT CCA GCA CAC AAG AGT C 3'
FWD Primer	5' GTA GGG ATA GAC CCT TTC AAA CTG 3'
RWD Primer	5' GAC TCT TGT GTG CTG GAT TCT C 3'
TaqMan Probe	5' /56 FAM/AG CCA AGT ATA CAG CCT AAT CAG ACC GA/3BHQ_1/ 3'
FWD qPrimer	5' /5Cy3/GT AGG GAT AGA CCC TTT CAA ACT G 3'
RWD qPrimer	5' /5IABkFQ/GA CTC TTG TGT GCT GGA TTC TC 3'
FWD Mistake qPrimer	5' /5Cy3/GT AGG GA**G** AGA CCC TTT CAA ACT G 3'

Table 8.2 Influenza A sequence information

Sequence Information	Influenza B
Source	GenBank Accession # AB036876 Influenza B
81Mer Template	5' GTG CTT CCC ATA AGC ATT TAC GCC AAA ATA CCT CAA CTA GGG TTC AAC GTT GAA GAG TAC TCT ATG GTT GGG TAT GAA GCC 3'
FWD Primer	5' GTG CTT CCC ATA AGC ATT TAC G 3'
RWD Primer	5' GGC TTC ATA CCC AAC CAT AGA G 3'
TaqMan Probe	5' /56 FAM/CC TCA ACT AGG GTT CAA CGT TGA AGA GT/3BHQ_1/ 3'
FWD qPrimer	5' /5Cy3/GT GCT TCC CAT AAG CAT TTA CG 3'
RWD qPrimer	5' /5IABkFQ/GG CTT CAT ACC CAA CCA TAG AG 3'

Table 8.3 Influenza type B sequence information

Sequence Information	Respiratory syncytial virus type A
Source	GenBank Accession # |JX627336.1|:5726-7450 Human respiratory syncytial virus strain RSVA/GN435/11, complete genome
85Mer Template	5' GTT GGA AAC TAC ACA CAT CTC CTC TAT GTA CAA CCA ACA CAA AGG AAG GAT CCA ACA TCT GCT TAA CAA GAA CCG ACA GAG GAT G 3'
FWD Primer	5' GTT GGA AAC TAC ACA CAT CTC CTC 3'
RWD Primer	5' CAT CCT CTG TCG GTT CTT GTT AAG 3'
TaqMan Probe	5' /56 FAM/CC AAC ACA AAG GAA GGA TCC AAC ATC TG/3BHQ_1/ 3'
FWD qPrimer	5' /5Cy3/GT TGG AAA CTA CAC ACA TCT CCT C 3'
RWD qPrimer	5' /5IABkFQ/CA TCC TCT GTC GGT TCT TGT TAA G 3'

Table 8.4 Respiratory syncytial virus type A sequence information

Sequence Information	Respiratory syncytial virus type B
Source	GenBank Accession # JX682822.1
81Mer Template	5' CCT CAC CTC AAG TCA GAA CAT AAC TGA GGA GTT TTA CCA ATC GAC ATG TAG TGC AGT TAG CAG AGG TTA CTT GAG TGC TTT 3'
FWD Primer	5' CCT CAC CTC AAG TCA GAA CAT AAC 3'
RWD Primer	5' AAA GCA CTC AAG TAA CCT CTG C 3'
TaqMan Probe	5' /56 FAM/AC CAA TCG ACA TGT AGT GCA GT/3BHQ_1/ 3'
FWD qPrimer	5' /5Cy3/CC TCA CCT CAA GTC AGA ACA TAA C 3'
RWD qPrimer	5' /5IABkFQ/AA AGC ACT CAA GTA ACC TCT GC 3'

Table 8.5 Respiratory syncytial virus type B sequence information

Sequence Information	Human rhinovirus
Source	GenBank Accession # AF108174.1
81Mer Template	5' ACA ATG GAC AAG GTG TGA AGA GCC CCG TGT GCT CGC TTT GAG TCC TCC GGC CCC TGA ATG TGG CTA ACC TTA ACC CTG CAG CTA G 3'
FWD Primer	5' ACA ATG GAC AAG GTG TGA AGA G 3'
RWD Primer	5' CTA GCT GCA GGG TTA AGG TTA G 3'
TaqMan Probe	5' /56 FAM/TG TGC TCG CTT TGA GTC CTC CG/3BHQ_1/ 3'
FWD qPrimer	5' /5Cy3/AC AAT GGA CAA GGT GTG AAG AG 3'
RWD qPrimer	5' /5IABkFQ/CT AGC TGC AGG GTT AAG GTT AG 3'

Table 8.6 Human rhinovirus sequence information

Sequence Information	Human metapneumovirus
Source	GenBank Accession # |AF371337.2|:3052-4671 Human metapneumovirus isolate 00-1, complete genome)
88Mer Template	5' GAG AGC ATT GAG AAC AGT CAG GCC TTG GTG GAT CAA TCA AAC AGA ATC CTA AGC AGT GCA GAG AAA GGA AAC ACT GGC TTC ATC ATT G 3'
FWD Primer	5' GAG AGC ATT GAG AAC AGT CAG G 3'
RWD Primer	5' CAA TGA TGA AGC CAG TGT TTC C 3'
TaqMan Probe	5' /56 FAM/AC AGA ATC CTA AGC AGT GCA GAG A/3BHQ_1/ 3'
FWD qPrimer	5' /5Cy3/GA GAG CAT TGA GAA CAG TCA GG 3'
RWD qPrimer	5' /5IABkFQ/CA ATG ATG AAG CCA GTG TTT CC 3'

Table 8.7 Human metapneumovirus sequence information